

University of Crete  
PHYSICS DEPARTMENT

# PHD THESIS

to obtain the title of

**PhD of Science**

of the University of Crete  
**Specialty : PHYSICS**

Defended by

Stefania PAPADOPOULOU  
on 10 December, 2019

## Bunch characteristics evolution for lepton and hadron rings under the influence of the Intra-beam scattering effect

under the Supervision of:  
Prof. Theodore TOMARAS  
Dr. Ioannis PAPAPHILIPPOU

**Committee :**

Prof. Theodore TOMARAS	-	UoC
Dr. Ioannis PAPAPHILIPPOU	-	CERN
Prof. Giorgos TSIRONIS	-	UoC
Prof. Ioannis KOMINIS	-	UoC
Prof. Konstantinos MAKRIS	-	UoC
Prof. Vasiliki PAVLIDOU	-	UoC
Prof. Nicolaos TSAMIS	-	UoC





# Abstract

The physical parameter quantifying particle events' production and thereby the performance of a collider is the luminosity. High luminosities are reached by increasing the beam brightness, i.e. the intensity on a specific phase space volume (emittance). In this respect, the luminosity of hadron and lepton rings is limited by a combination of collective effects causing particle losses and emittance growth. In particular, Intra-beam scattering (IBS) impacts beam quality, through emittance growth. Several IBS theoretical models and their approximations exist, all assuming Gaussian beams. This thesis elaborates the optimization of the lattice design for a lepton ring and the study of the bunch characteristics evolution for a hadron ring, under the influence of IBS. Taking into account IBS, based on analytical results and numerical simulations, the optics design optimization is presented for the damping rings (DRs) of the Compact Linear Collider (CLIC). Specifically, aiming to reduce the betatron emittance of the DRs, dipoles whose magnetic field varies longitudinally are used together with high-field SC wigglers. Based on measurements and Monte-Carlo simulations, the interplay between IBS and radiation effects is also studied for the Large Hadron Collider (LHC), in view of understanding the bunch parameters evolution that determine the delivered luminosity. For the LHC bunch profiles which are observed to be non-Gaussian along the LHC energy cycle, appropriate fitting functions are used in order to describe accurately the distributions. In addition, the impact of the non-Gaussian distributions on the estimation of the beam size and thus, of the luminosity is studied. The importance to develop analytical formulas and simulation tools that calculate IBS for any distribution is underlined.

# Περίληψη

Η φυσική παράμετρος που ποσοτικοποιεί την παραγωγή των γεγονότων σωματιδίων και συνεπώς την απόδοση ενός επιταχυντή είναι η φωτεινότητα. Υψηλές φωτεινότητες επιτυγχάνονται αυξάνοντας τον πληθυσμό σωματιδίων σε συγκεκριμένο όγκο του φασικού χώρου (εκπεμπτικότητα - emittance) της δέσμης. Η φωτεινότητα των επιταχυντικών δακτυλίων λεπτονίων και αδρονίων περιορίζεται από ένα συνδυασμό φαινομένων που προκαλούν απώλειες σωματιδίων και αύξηση της emittance. Συγκεκριμένα, η ενδο-δεσμική σκέδαση (intra-beam scattering - IBS) επηρεάζει την ποιότητα της δέσμης, μέσω της αύξησης της emittance. Τα υπάρχοντα θεωρητικά μοντέλα της IBS και οι προσεγγίσεις τους, θεωρούν πως οι δέσμες είναι και παραμένουν Γκαουσιανές. Η παρούσα διατριβή παρουσιάζει το σχεδιασμό και τη βελτιστοποίηση της οπτικής του μαγνητικού πλέγματος για ένα δακτύλιο λεπτονίων και τη μελέτη της εξέλιξης των χαρακτηριστικών της δέσμης για ένα δακτύλιο αδρονίων, υπό την επίδραση της IBS. Λαμβάνοντας υπόψη την IBS, βάσει αναλυτικών αποτελεσμάτων και αριθμητικών προσομοιώσεων, μελετήθηκε η βελτιστοποίηση του σχεδιασμού της οπτικής για τους δακτυλίους απόσβεσης (Damping Ring - DR) του Γραμμικού Συμπαγή Συγκρουστήρα (Compact Linear Collider - CLIC). Συγκεκριμένα, με στόχο τη μείωση της emittance των DRs, χρησιμοποιούνται δίπολα των οποίων το μαγνητικό πεδίο μεταβάλλεται διαμήκως, σε συνδυασμό με υπεραγωγίμους συστρεφόμενους μαγνήτες απόσβεσης υψηλού πεδίου. Επίσης, βάσει μετρήσεων και προσομοιώσεων Monte-Carlo, μελετάται η αλληλεπίδραση μεταξύ της IBS και φαινομένων ακτινοβολίας για τον Μεγάλο Επιταχυντή Αδρονίων (Large Hadron Collider - LHC), ώστε να κατανοηθεί η εξέλιξη των παραμέτρων της δέσμης που καθορίζουν την παραγόμενη φωτεινότητα. Για τις κατανομές των δεσμών σωματιδίων του LHC, οι οποίες παρατηρούνται να είναι μη Γκαουσιανές κατά τον κύκλο ενέργειας του LHC, χρησιμοποιούνται κατάλληλες συναρτήσεις κατανομών για την ακριβή περιγραφή τους. Επιπλέον, ερευνώνται οι επιπτώσεις των μη Γκαουσιανών κατανομών στην εκτίμηση του μεγέθους της δέσμης και συνεπώς της φωτεινότητας. Τέλος, υπογραμμίζεται η σημασία της ανάπτυξης αναλυτικών τύπων και εργαλείων προσομοίωσης που υπολογίζουν την IBS για οποιαδήποτε κατανομή.

# Contents

<b>1</b>	<b>Introduction</b>	<b>1</b>
1.1	Physics potential of circular and linear colliders . . . . .	1
1.2	LHC overview . . . . .	3
1.3	CLIC overview . . . . .	7
1.4	Scope of the thesis . . . . .	9
<b>2</b>	<b>Introduction to beam dynamics</b>	<b>12</b>
2.1	Linear single particle beam dynamics . . . . .	12
2.2	Transverse motion . . . . .	13
2.3	Longitudinal motion . . . . .	19
2.4	Synchrotron radiation and damping . . . . .	22
2.5	Equilibrium beam properties . . . . .	25
2.6	Low emittance lattices . . . . .	27
2.7	Insertion devices . . . . .	28
2.8	Collective effects . . . . .	29
<b>3</b>	<b>Intrabeam Scattering</b>	<b>30</b>
3.1	Theories of Intrabeam Scattering . . . . .	30
3.2	Equilibrium emittances due to IBS . . . . .	32
3.3	IBS in MAD-X . . . . .	33
3.4	The multi-particle tracking codes . . . . .	33
<b>4</b>	<b>Reduction of the TME cell emittance using longitudinally variable bends</b>	<b>38</b>
4.1	Analytical solutions for minimizing the emittance of a TME cell . . . . .	38
4.2	Dipole profiles . . . . .	44
<b>5</b>	<b>Alternative CLIC DR design using longitudinally variable bends and high field wigglers</b>	<b>49</b>
5.1	Longitudinally variable field dipole design for the CLIC Damping Rings . . . . .	49
5.2	Numerical application for a variable bend TME cell . . . . .	51
5.3	Alternative CLIC DR design . . . . .	55
5.4	CLIC DR design parameters for the original and the improved design . . . . .	58
<b>6</b>	<b>IBS Simulations for the CLIC DRs</b>	<b>60</b>
6.1	The IBS growth rates along the CLIC DR . . . . .	60
6.2	Benchmarking of the B-M IBS theoretical model with SIRE . . . . .	61
<b>7</b>	<b>Bunch profile measurements at the LHC</b>	<b>64</b>
7.1	Transverse bunch profile instruments . . . . .	64
7.2	Longitudinal bunch profile instruments . . . . .	66
7.3	Probability distribution functions for the LHC bunch profiles . . . . .	67

---

7.4	Example of transverse bunch profiles at the LHC FT energy . . . . .	69
<b>8</b>	<b>Luminosity observations and estimations</b>	<b>71</b>
8.1	Emittance observations in the LHC . . . . .	71
8.2	Observations and modeling of the LHC Luminosity . . . . .	73
8.3	Luminosity estimations . . . . .	75
<b>9</b>	<b>IBS Simulations for the LHC</b>	<b>81</b>
9.1	Benchmarking of the B-M IBS theoretical model with SIRE . . . . .	84
9.2	Comparison with experimental data from Run 2 . . . . .	90
<b>10</b>	<b>Conclusions</b>	<b>95</b>
	<b>Appendices</b>	<b>99</b>
<b>A</b>	<b>The Bjorken-Mtingwa formalism auxiliary matrices</b>	<b>100</b>
<b>B</b>	<b>The integrals to calculate the emittance of a variable bend</b>	<b>101</b>
<b>C</b>	<b>The emittance reduction factor as a function of <math>\rho</math> and <math>\lambda</math> for the step and the trapezium profile</b>	<b>102</b>
<b>D</b>	<b>CLIC DRs design parameters for the case of <math>N_b = 5.7 \times 10^9</math></b>	<b>103</b>
<b>E</b>	<b>Luminosity calculation for q-Gaussian density distribution functions</b>	<b>104</b>
	<b>Bibliography</b>	<b>106</b>

# Introduction

---

## 1.1 Physics potential of circular and linear colliders

The Standard Model provides a unified picture of the fundamental Universe constituents and their interactions. Numerous experimental results have corroborated its predictions. A scalar, spin-0, with a mass of  $\sim 125$  GeV particle, which is the consequence of the Higgs mechanism after the spontaneous symmetry breaking, was discovered by the ATLAS [1] and CMS [2] experiments of the LHC in 2012. In addition, the first observations of the very rare decay of the  $B_s$  meson into two muons ( $B_s^0 \rightarrow \mu^+ \mu^-$ ) which is a major test of super-symmetry, was recorded by the LHC. Some other worth-mentioning achievements are the creation of a quark-gluon plasma and the discovery of the  $\xi_b(3P)$  bottomonium state and the massive 125 GeV boson which has been confirmed to be the long-sought Higgs boson [1, 2].

Several upgrade options that aim to extend the LHC discovery potential are currently being studied. For the High-Luminosity LHC (HL-LHC) [3], that is the major LHC upgrade to start around 2020, the luminosity is increased by at least a factor of 10 compared to the nominal LHC design value (from 300 to 3000 fb<sup>-1</sup>). In order to achieve that, the bunch intensity needs to be increased and the transverse beam size at the collision points has to be lowered. The extreme beam parameters enhance strong intensity effects that can be mitigated by considering alternative design options. In view of reaching the beam parameters for the HL-LHC, the LHC Injectors Upgrade (LIU) [4] is also one of the projects being implemented.

While the Long-Shutdown 2 (LS2) is ongoing, the debate on what will be the next machine at the energy frontier has started. The proposals for the alternatives are being discussed and the related studies are progressing. The main protagonists of this debate are a new generation of circular colliders much larger than the LHC and long linear colliders accelerating leptons.

The Future Circular Collider (FCC) study develops options for potential high-energy frontier circular colliders at CERN for the post-LHC era. The main FCC design scenario is a hadron collider with a centre-of-mass energy of the order of 100 TeV in a new 80-100 km circumference tunnel. The corresponding hadron injector chain takes into account the existing CERN accelerator infrastructure and the long-term accelerator operation plans. The conceptual design study also includes a lepton collider with a centre-of-mass energy of the order of 90 to 365 GeV and its detectors, as a potential intermediate step towards realization of the hadron facility.

After the discovery of a Higgs-like boson, the particle physics community expressed a consensus that the results of the LHC will need to be complemented by experiments at a lepton collider at the TeV energy range. In a lepton collider the center-of-mass energy and initial-state polarizations are precisely known and can be adjusted, and backgrounds are many orders of magnitude lower than the QCD backgrounds that challenge hadron collider environments. Collisions between  $e^+/e^-$  beams at the TeV scale are conceivable only by means of Linear Colliders (LC),

which do not bend the beam and so, the massive energy losses and beam degradation caused by synchrotron radiation are avoided. The limitations emerging from crossing beams, like the beam-beam effect, are more relaxed compared to a circular accelerator. Even if each pair of bunches collides only once, the small beam sizes provided in a LC result in high luminosities [5] (see Fig. 1.1). The exact requirements of such experiments are expected to be defined from the LHC results of Run 2 (2015-2018), when substantial integrated luminosity will have been accumulated at full LHC energy [6].

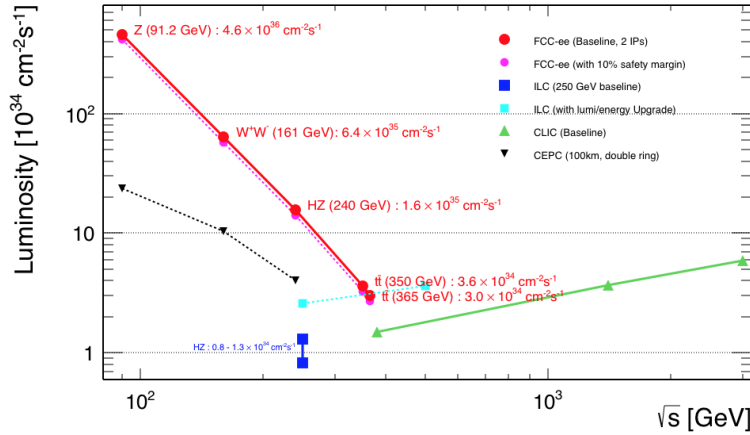


Figure 1.1: Target luminosities as a function of center-of-mass energy for future circular (FCC-ee, CEPC) and linear (ILC, CLIC)  $e^+e^-$  colliders [5].

The two options for a future  $e^+e^-$  LC developed are the International Linear Collider (ILC) that uses superconducting Radio-Frequency (RF) cavities and the Compact Linear Collider (CLIC) that uses a separate drive beam to provide the accelerating power to normal conducting (or copper) RF cavities. The ILC technology provides an option for a Higgs and top factory to be constructed on a relatively short timescale. It aims at colliding beam energy of 500 GeV, upgradeable to 1 TeV [7]. CLIC aims to extend the energy range of linear colliders into the multi-TeV region by introducing for the first time a technology of Two-Beam Acceleration (TBA), providing colliding beams up to 3 TeV. At different energy stages of CLIC, precision measurements of various observables of the Standard Model Higgs boson can be carried out.

## Luminosity

The performance of a collider is determined by the luminosity [8] which is given by:

$$\mathcal{L} = \frac{n_b f_{rev} N_1(t) N_2(t)}{2\pi \sigma_x(t) \sigma_y(t)} H(\sigma_s(t), \beta^*) F_{geom}(\sigma_s(t), \beta^*) , \quad (1.1)$$

where  $n_b$  is the number of colliding bunches,  $f_{rev}$  is the revolution period,  $N_{1,2}$  is the number of particles per bunch for each beam,  $\sigma_{x,y}$  are the horizontal and vertical rms beam sizes,  $\sigma_s$  is the rms bunch length and  $\beta^*$  is the beta function at the collision point when assuming round optics. Due to the crossing angle at collision  $\phi$  and the fact that the beta function varies rapidly around

the interaction point (IP), a geometric factor  $F_{geom}(\sigma_s(t), \beta^*)$ , and the hourglass effect reduction factor  $H(\sigma_s(t), \beta^*)$  are considered. The luminosity of two colliding Gaussian bunches is given for the convoluted transverse beam sizes being:

$$\sigma_x(t) = \sqrt{\sigma_{x_1}(t)^2 + \sigma_{x_2}(t)^2} \quad \text{and} \quad \sigma_y(t) = \sqrt{\sigma_{y_1}(t)^2 + \sigma_{y_2}(t)^2}, \quad (1.2)$$

where the subscripts 1 and 2 correspond to the two colliding bunches. In order to achieve the high luminosity, very small transverse beam sizes or emittances and a large number of high intensity bunches are required.

## 1.2 LHC overview

The European Organization for Nuclear Research (CERN) is an international laboratory that operates a series of accelerators for nuclear and particle physics research, including the Large Hadron Collider (LHC), as well as a range of lower energy particle accelerators. A highlight of the experiment's results using data acquired during the LHC Run 1 is the discovery of a new boson compatible with the Higgs mechanism [1, 2].

### LHC layout and performance

In the Large Hadron Collider (LHC), proton beams are accelerated to a high energy and are then brought in collision to probe into the heart of matter. The top energy is gradually built up in a chain of accelerators of equal importance. Each machine boosts the energy of the particles beam, before injecting it into the next machine in a sequence. A full scheme of the CERN accelerator chain is shown in Fig. 1.2.

The proton source consists of hydrogen gas that is injected in a plasma chamber, where the atoms are ionized by strong electromagnetic fields and are then extracted at 100 KeV towards LINAC 2. The LINAC 2 is a linear accelerator in which protons are captured in bunches, accelerated to the energy of 50 MeV and sent to the first circular accelerator in the chain. The Proton Synchrotron Booster (PSB) accelerates the protons from 50 MeV/c to 1.4 GeV/c for injection into the Proton Synchrotron (PS), where the protons are accelerated up to a momentum of 26 GeV/c. Then, the beam is extracted towards the Super Proton Synchrotron (SPS) that accelerates the proton beams up to 450 GeV/c (the injection energy of the LHC). The injectors, apart from accelerating the LHC beam, provide beams for fixed target experiments that operate at different energies.

The heavy ions that are produced from a different source, are first accelerated in the Linear Accelerator 3 (LINAC 3) to an energy of 4.2 MeV/u. Then, the ions are transferred to the Low-Energy Ion Ring (LEIR), where the energy gain goes up to 72 MeV/u for injection into the PS. After the PS, the ions follow the same path as the protons.

Finally, the injected beams of 450 GeV/c are brought up by design report to 7 TeV/c in the LHC, making it the worlds highest energy particle accelerator. The LHC with a circumference of 27 km long, lays at about 100 m underground. Two counter rotating beams circulate in two separated rings designed to be filled with protons (p) or ions (Pb). The beams collide in four Interaction Points (IP 1, 2, 5, 8), distributed around the ring, where the detectors of ATLAS,



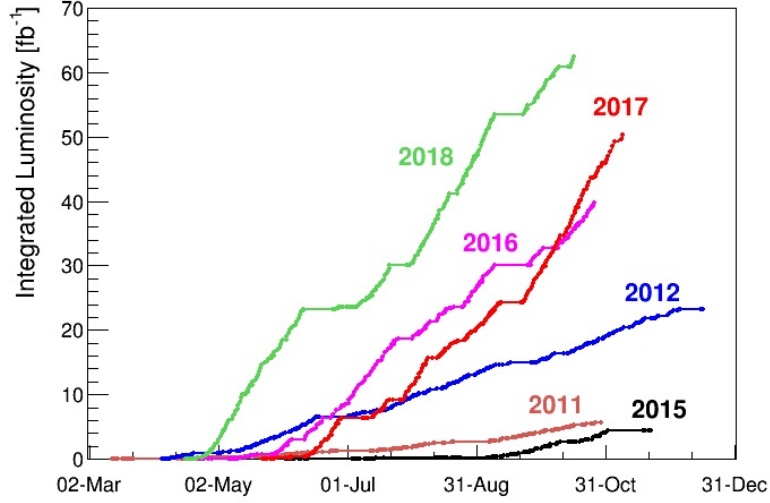


Figure 1.3: The integrated luminosity delivered to the ATLAS and CMS experiments during different LHC runs.

blow-up in the LHC during the ramp, it is observed that the BCMS beam gives an increase in peak luminosity of around 20%. The BCMS parameters for the HL-LHC are only considered for injection and as a backup parameter set in case one encounters larger than expected emittance growth in the HL-LHC during injection, ramp and squeeze.

## LHC cycle

The intrabeam scattering (IBS) effect is one of the main mechanisms that determine the emittance evolution of the beams during injection energy (i.e. 450 GeV), during the energy ramp and the first part of the collision energy (i.e. 6.5 TeV) of the LHC. During collisions, apart from the IBS and Synchrotron Radiation (SR) which are the dominant effects for the emittance evolution, a combination of other diffusion mechanisms, like the beam-beam effect, electron-cloud, noise (due to the power converters, the transverse damper, the crab cavities in the case of the HL-LHC, etc.), non-linearities, etc., cause emittance blow up and/or particle losses [12].

The main mechanism of the bunch intensity reduction during collisions is the luminosity burn-off that describes the bunch current decay due to the collisions themselves. The burn-off decay time is given by:

$$\tau_{nuc} = \frac{N_{b0}}{kL_0\sigma_{tot}} \quad (1.3)$$

where  $N_{b0}$  is the initial bunch intensity,  $L_0$  the initial luminosity,  $k$  the number of interaction points and  $\sigma_{tot}$  the proton-proton total cross section that is energy depended. Due to the very small beta functions at the interaction points, only the inelastic part of the proton-proton collisions is expected to contribute to the burn-off losses, while the elastic part is causing transverse

Table 1.1: Nominal and HL-LHC main parameters (2017).

Description [units]	Nom. LHC (design report)	Nom. BCMS	HL-LHC	HL-LHC BCMS
Beam energy in collision [TeV]	7	7	7	7
Particles per bunch, $N_b$ [ $10^{11}$ ]	1.15	2.2	2.2	2.2
Number of collisions in IP1 and IP5	2808	2592	2736	2592
$N_{tot}$ [ $10^{14}$ ]	3.2	5.73	6.00	5.70
Beam current [A]	0.58	1.04	1.09	1.03
Crossing angle in IP1 and IP5 [ $\mu$ rad]	512	512	590	590
Min. normalized LR BB* separation [ $\sigma$ ]	9.4	12.5	12.5	12.5
Min. $\beta^*$ [m]	0.55	0.20	0.15	0.15
$\varepsilon_n$ [ $\mu$ m]	3.75	2.5	2.5	2.5
$\varepsilon_l$ [eVs]	2.5	2.5	2.5	2.5
r.m.s. energy spread [ $10^{-4}$ ]	1.13	1.20	1.13	1.13
r.m.s. bunch length [cm]	7.55	7.55	7.55	7.55
IBS horizontal [h]	105	18.8	18.5	18.5
IBS longitudinal [h]	63	25.0	20.4	20.4
Peak lumi. without CC** [ $10^{34}\text{cm}^{-2}\text{s}^{-1}$ ]	1.00	6.32	7.18	6.80
Virtual lumi. with CC [ $10^{34}\text{cm}^{-2}\text{s}^{-1}$ ]	1.18	1.29	19.54	18.52
$N_b$ at injection [ $10^{11}$ ]	1.2	2.3	2.3	2.3
$\varepsilon_n$ at SPS extraction [ $\mu$ m]	3.4	1.7	2.0	< 2.0

\* LR BB= Longe-Range Beam-Beam

\*\* CC= Crab Cavities

emittance blow up [6]. The bunch current evolution is then given by:

$$N_b = \frac{N_{b0}}{1 + t/\tau_{nuc}} . \quad (1.4)$$

Figure 1.4 presents the evolution of the bunch current, for all the colliding and non-colliding

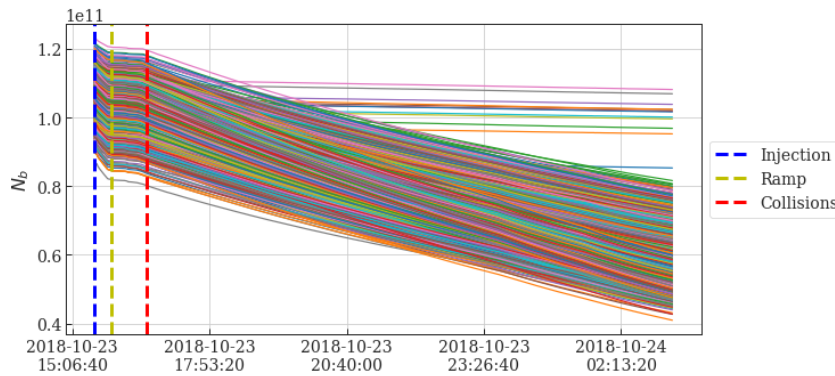


Figure 1.4: Bunch current evolution, for colliding and non-colliding bunches, during injection energy (i.e. 450 GeV) and during collision energy (i.e. 6.5 TeV) of the LHC.

bunches, during a typical LHC energy cycle. The time stamps that correspond to the injection of the bunches, the start of the energy ramp and the start of the collisions process are noted.

### 1.3 CLIC overview

Following preliminary physics studies based on an electron-positron collider in the multi-TeV energy range [13], the CLIC study is focused on the design of a linear collider with a center-of-mass collision energy of  $E = 3$  TeV. Superconducting technology cannot achieve the very high acceleration gradient of 100 MV/m, thus would require a much longer linear accelerator. Since the goal of the CLIC collider is a high luminosity at a high energy at the lowest possible construction cost and power, the two beam acceleration scheme was proposed. Following the 2012 CLIC Conceptual Design Report [6], the main beam and linac parameters for a luminosity of  $\mathcal{L} = 2 \times 10^{34} \text{ cm}^{-2}\text{s}^{-1}$  at  $E=3$  TeV, are summarized in Table 1.2.

Table 1.2: CLIC main parameters for 500 GeV and 3 TeV.

Description [units]	500 GeV	3 TeV
Total (peak 1%) luminosity	2.3 (1.4) $\times 10^{34}$	5.9 (2.0) $\times 10^{34}$
Total site length [km]	13.0	48.4
Loaded accel. gradient [MV/m]	80	100
Main Linac RF frequency [GHz]		12
Beam power/beam [MW]	4.9	14
Bunch charge [ $10^9 e^+/e^-$ ]	6.8	3.72
Bunch separation [ns]		0.5
Bunch length [ $\mu\text{m}$ ]	72	44
Beam pulse duration [ns]	177	156
Repetition rate [Hz]		50
Hor./vert. norm. emitt. [ $10^{-6}/10^{-9}$ m]	2.4/25	0.66/20
Hor./vert. IP beam size [nm]	202/2.3	40/1
Beamstrahlung photons/electron	1.3	2.2
Hadronic events/crossing at IP	0.3	3.2
Coherent pairs at IP	200	$6.8 \times 10^8$

Figure 1.5 illustrates the layout of the CLIC accelerator complex at 3 TeV [6]. The main components of the complex are the particle sources, the damping rings which are used for producing small beam sizes, the main linacs which accelerate the beams to full energy, the beam delivery system including the final focus, the post-collision diagnostic lines and the dumps. The Main Beam is generated and pre-accelerated in the injector linacs. Then, it enters the Damping Rings complex for reducing the beam emittances down to 500 nm and 5 nm, normalized to the beam energy, in the horizontal and vertical plane respectively. After being accelerated in a booster linac, the beams are transported through the main tunnel to the turnarounds and later, they are accelerated with a gradient of 100 MV/m. The Drive Beam pulses are generated in the two Main Linacs and are compressed in the Delay Loops and Combiner Rings (CR1 and CR2). Afterwards, they are transported through the Main Linac tunnel to 24 individual turnarounds. For the final RF power generation, each Drive Beam segment is directed by pulsed Power Extraction and Transfer Structures (PETS) into the accelerating structures of the Main Beams. The beams collide after a long Beam Delivery Section (BDS), including collimation and final focus, at the

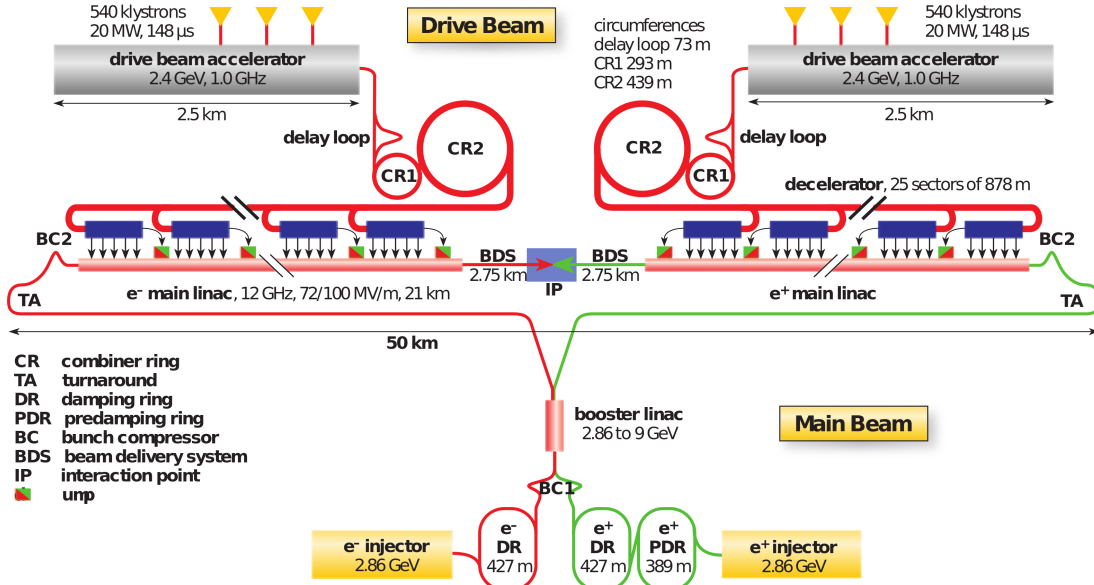


Figure 1.5: The CLIC layout at 3 TeV [6].

interaction point (IP).

For an optimal exploitation of its physics potential, CLIC is foreseen to be operated in a staged approach with three centre-of-mass energy stages (ranging from a few hundred GeV up to 3 TeV). The first stage will focus on precision Standard Model physics, in particular Higgs and top-quark measurements. The goals of subsequent stages are the measurements of rare Higgs processes, precision measurements (i. e. states previously discovered at the LHC or at the CLIC itself) and exploration of new states for new physics processes. The studies for the proposed lower energy stages and the updated baseline staging scenario for CLIC is presented in [14].

## CLIC Damping Rings

The CLIC Damping Rings (DRs) baseline design aims to reach ultra-low emittance with high bunch charge necessary for the luminosity requirements of the collider, providing the final stage of damping. The DRs requirements are driven by the main parameters of the collider, which are summarized in Table 1.3 [15]. The DRs have to accommodate a 2.86 GeV beam and should damp it down to normalized horizontal and vertical emittances of 500 nm-rad and 5 nm-rad respectively. The longitudinal normalized emittance should be kept below 6 keV·m. The requirements for ultra-low emittances in all three planes give rise to a series of collective effects, with intrabeam scattering (IBS) being the dominant one. That makes the lattice design of the main DRs very challenging in terms of beam dynamics and technology.

The current CLIC DR layout is presented in Fig. 1.6 has a racetrack with two arcs and two long straight sections (LSS). The arcs are composed by theoretical minimum emittance (TME) cells and the LSS by FODO cells filled with damping wigglers. Space is also reserved for RF cavities, injection and extraction equipment [16]. The lattice functions between the arcs and the

straight sections are matched from the dispersion suppressors and beta matching sections.

Table 1.3: The required injection and extraction parameters of the DR complex.

Parameters	Injected		Extracted
	$e^-$	$e^+$	$e^-/e^+$
Bunch Population [ $10^9$ ]	4.4	4.6	4.1
Bunch spacing [ns]	0.5/1	0.5/1	0.5
Bunches/train	312/156	312/156	312
Number of trains	2	2	1
Repetition rate [Hz]	50	50	50
Norm. horiz. emittance [nm·rad]	$100 \times 10^3$	$7 \times 10^6$	500
Norm. vert. emittance [nm·rad]	$100 \times 10^3$	$7 \times 10^6$	5
Norm. long. emittance [keV·m]	2.86	2288	6

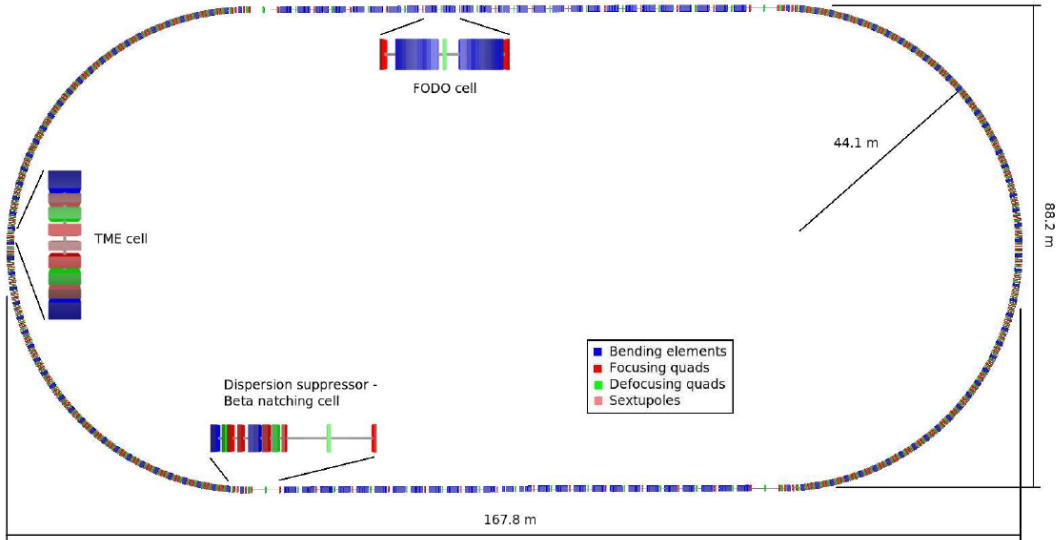


Figure 1.6: The CLIC Damping Ring layout [6].

## 1.4 Scope of the thesis

One of the statistical processes causing a spreading of particles in phase space or a continuous increase of beam emittance, with a direct impact on the luminosity, is the small angle multiple Coulomb scattering, called Intrabeam scattering (IBS). The IBS plays an important role in high intensity hadron [17] and ion [18] circular machines and, in  $e^+/e^-$  damping rings, high intensity/low energy light sources [19]. The luminosity performance of hadron machines is limited by the IBS effect causing emittance growth. For lepton machines such as future linear collider Damping Rings, new generation light sources, the IBS effect can also be predominant.

Several analytical models that describe the IBS effect exist, all assuming Gaussian beam distributions. In the case of non-Gaussian beam distributions, on the other hand, no analytical models exist. Taking into account IBS and radiation effects but also other diffusive mechanisms, there is no evidence that the distribution remains Gaussian. The way IBS and radiation effects act depends on the shape of the distributions. In view of quantifying the impact of the distribution's shape on the beam parameters and consequently on the luminosity, it is important to study the interplay between these effects for any distribution.

This PhD thesis elaborates the bunch characteristics evolution for lepton and hadron machines under the influence of the intrabeam scattering (IBS) effect. The first part of this thesis concerns the design of the optics and optimization of the performance of the CLIC main damping rings (DRs). The DR lattice design is driven by the emittance requirements, imposed by the luminosity goal of the linear collider, which for ultra-low values give rise to collective effects, with IBS being the dominant one. An alternative design is proposed, which aims to mitigate the IBS effect for a compact ring, using longitudinally variable bends and high field insertion devices which are formed by a sequence of short dipole fields of alternating polarity, called wigglers. The second part of this thesis is dedicated to the studies of LHC bunch profiles and their impact on the evolution of the bunch characteristics and the luminosity. The performance of a high-energy hadron collider such as the LHC is heavily based on the preservation of the injected emittances, under the influence of several degrading mechanisms, such as the effect of IBS. In order to understand the evolution of the bunch characteristics that determine the delivered luminosity, it is important to study the interplay between IBS and radiation effects during the full LHC energy cycle.

Chapter 2 is devoted to the theoretical principles of beam dynamics in accelerators, focusing on the linear single particle motion under the influence of electromagnetic forces. The basic equations describing the transverse and longitudinal motion in an accelerator are defined. The synchrotron radiation (SR) theory and its damping mechanism which, together with the quantum excitation (QE), leads to the equilibrium beam properties, is explained. Concerning the lepton rings, the lattices giving low emittances and the insertion devices that determine the beam damping are discussed. Finally, a brief description of the main collective effects is given.

In Chapter 3, the theories of intrabeam scattering (IBS), that is one of the main effects leading to an increase of beam emittances in ultra low emittance lepton machines and high intensity hadron machines, are described. The expressions of the final state emittances, taking into account IBS, SR damping and QE are given. The IBS theoretical model of Bjorken-Mitingwa, which is implemented in the Methodical Accelerator Design code MAD-X [20] is described. In addition, the Monte-Carlo multiparticle code (called SIRE) used for tracking particle distributions under the effects of IBS, SR and QE, is presented.

A low emittance lattice design capable of providing the lowest possible emittance in a compact cell, is the theoretical minimum emittance (TME) cell. The detailed study for reducing further the emittance of a TME cell by using longitudinally variable bends is presented in Chapter 4. The emittance reductions achieved using the variable bend profiles instead of a uniform dipole (of the same bending angle) are presented.

The magnetic design according to the characteristics of a dipole with the optimal longitudinal field variation in terms of emittance reduction, is shown in Chapter 5. The numerical results

obtained when implementing the designed magnet in the CLIC DR lattice are used for the optimization of the arc TME cells. The optimization of the CLIC DR FODO cell using high field wigglers, is also discussed. Finally, the new performance parameters for the alternative CLIC DR design are presented. Chapter 6 presents the benchmarking of the Bjorken-Mtingwa (B-M) IBS theoretical model with the IBS Monte-Carlo tracking code called SIRE (Software for IBS and Radiation Effects) for the CLIC DRs.

For the LHC luminosity studies, a model including the effects of intrabeam scattering (IBS), synchrotron radiation, elastic scattering and luminosity burn-off is used [21]. A comparison of the bunch characteristics evolution as predicted by this model with the measured ones revealed an extra (on top of the model) transverse emittance blow up in the measured data. One of the attempts to explain this blow up concerns the bunch profiles that appear to have non-Gaussian shapes. The aim of the studies presented in Chapter 7 and in Chapter 8, is to quantify the impact of the distribution's shape on the emittance and luminosity estimations.

In Chapter 9, the simulations performed using SIRE for the LHC are discussed. The benchmarking of the code with the analytical IBS formulas gave encouraging results with respect to the idea of employing a novel distribution function to study the IBS for various machine parameters, including the HL-LHC upgrade. In the end, the comparison of experimental data with simulations and theoretical models, is presented.

Finally, the last chapter is devoted to the conclusions of this thesis.

# Introduction to beam dynamics

## 2.1 Linear single particle beam dynamics

The interaction of charged particles with electromagnetic fields determines their motion in accelerators. Detailed knowledge of this interaction in the six-dimensional phase space is necessary for predicting the beam behavior and understanding how to meet the design goals of an accelerator. The interplay between particles and fields is called beam dynamics. This section is meant to give an overview of the basic equations governing the motion of the particles in an accelerator.

In an accelerator the charged particles are guided and accelerated by means of electromagnetic fields, based on the relativistic form of the Lorentz equation:

$$\vec{F} = \gamma q(\vec{E} + c\vec{\beta} \times \vec{B}), \quad (2.1)$$

where  $\vec{F}$  is the force acting on a particle of electric charge  $q$  moving at a relativistic velocity of  $\vec{u} = c\vec{\beta}$ , due to the electromagnetic fields and  $\vec{E}$  and  $\vec{B}$ . The Lorentz factor is defined as  $\gamma = 1/\sqrt{1 - u^2/c^2}$ , with  $c$  being the speed of light. The electric field is supplied using the Radio Frequency (RF) cavities, that provide the energy for the particles acceleration and compensate for the energy loss. The magnetic fields are responsible of the bending and the focusing of the particles around the design trajectory for the nominal momentum particles.

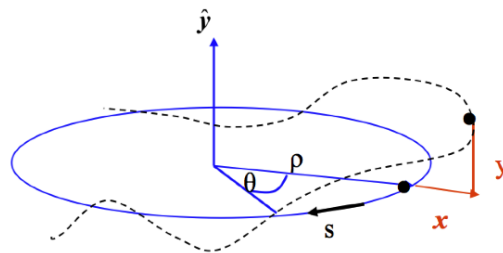


Figure 2.1: The trajectory coordinates are given with respect to the Frenet-Serret frame, which rotates with the ideal particle around the accelerator [22].

The Frenet-Serret coordinate system is used to determine the kinematic properties of a particle moving along a continuous, differentiable curve in the three-dimensional Euclidean space. This system is used to describe the motion of the particles in the vicinity of the ideal orbit. The designed orbit is the blue colored circle in Fig.2.1, while a particle's trajectory around this orbit is drawn with a dashed black line. The longitudinal direction along the circumference of the ring

is denoted by  $s$ . The horizontal and the vertical planes denoted by  $x$  and  $y$  respectively, compose the transverse plane. The  $\theta$  and  $\rho$  correspond to the bending angle and radius respectively.

In general, only transverse field components are considered. This means that the magnetic field vector  $\vec{B}$  is perpendicular to the velocity vector. The transverse components of the particles velocities for relativistic beams are small compared to the particle velocity  $u_z$  ( $u_x \ll u_z$ ,  $u_y \ll u_z$ ,  $u_s \approx u_z$ ). Under these assumptions, from the equilibrium of the centrifugal force and the Lorentz force, the bending radius of a charged particle passing through the vertical homogeneous field  $B$  generated by a dipole magnet, is given by [23]:

$$\frac{1}{\rho_x} [\text{m}^{-1}] = 0.2998 \frac{|B[\text{T}]|}{\beta E[\text{GeV}]} . \quad (2.2)$$

The magnetic rigidity of the beam, that depends only on the beam energy, is defined as:

$$(B\rho_x) = \frac{\beta E[\text{GeV}]}{0.2998} , \quad (2.3)$$

The deflection angle in a magnetic field is:

$$\theta = \int \frac{ds}{\rho_x} , \quad (2.4)$$

The Lorentz forces are applied not only to guide particles along a specific path but also to focus the beam within a narrow vicinity of the ideal path. In order to that, the focusing forces are applied at exact points so that to achieve specific beam properties along the accelerator. The focusing is provided by the quadrupole magnets, whose field is zero on the  $s$  axis and increases linearly with distance as:

$$B_y = gx, \quad B_x = gy, \quad \text{where} \quad g = \frac{\partial B_x}{\partial y} = \frac{\partial B_y}{\partial x} . \quad (2.5)$$

The focusing strength is given by:

$$k[\text{m}^{-1}] = 0.2998 \frac{g[\text{T/m}]}{\beta E[\text{GeV}]} . \quad (2.6)$$

For a positively charged particle, the quadrupole with  $\partial B_y/\partial x$  will provide horizontal focusing and vertical defocusing that correspond to  $k > 0$  and  $k < 0$  respectively. This will be reversed, if the current direction or the particle charge is reversed. The sign and the value of the deflection that a particle undergoes in the quadrupoles varies with its momentum and its transverse offset with respect to the magnet's center. Hence, particles in a bunch see different focusing strengths, leading to chromatic effects. In order to correct them, sextupole and octupole magnets are used.

## 2.2 Transverse motion

In particle beam dynamics, the equation of motion in periodic lattices is described by Hill's equations [23, 24] that are basically the ones of a harmonic oscillator with periodic coefficients.

These equations for the linear motion of particles in a circular machine (i.e. considering only dipole and quadrupole magnets) are given by:

$$\frac{d^2x}{ds^2} - K_1(s)x = \frac{1}{\rho_x(s)} \frac{\delta p}{p_0}, \quad (2.7)$$

$$\frac{d^2y}{ds^2} - K_1(s)y = 0. \quad (2.8)$$

The coefficient  $K_1$  is the general focusing strength, which can be expressed, including the weak focusing from the dipole and the strong focusing from quadrupole magnets, in the general form:

$$K_1(s) = \frac{1}{\rho_{x,y}^2(s)} - \frac{1}{B\rho_x} \frac{\partial B_y(s)}{\partial x}, \quad (2.9)$$

where  $\rho_x(s)$  is the bending radius of the element at position  $s$ .  $K_1(s)$  and  $\rho_x(s)$  are periodic functions of  $s$ , with a period at least equal to the circumference of the closed orbit of the machine.  $\delta p/p_0$  is the relative momentum deviation of an off-momentum particle with momentum  $p_0 \pm \delta p$  from the design (reference) momentum  $p_0$ .

According to Floquet's theorem [24], the solutions to the homogeneous Hill's equations can be written in the form:

$$z(s) = Aw(s) \cos(\phi_z(s) + \phi_0), \quad (2.10)$$

where  $w(s) = w(s + C)$  and  $\phi_z(s) = \phi_z(s + C)$  are periodic functions with the same period  $C$ , and  $z = x$  or  $y$ . The phase  $\phi_0$  is determined by the initial conditions. Substituting Eq. (2.10) to Eq. (2.7) and (2.8), the betatron phase advance  $\phi_z(s)$  and the betatron or twiss (Courant-Snyder parameters) functions  $\alpha_z(s)$ ,  $\beta_z(s)$  and  $\gamma_z(s)$  can be defined, describing the motion of the particle with the maximum amplitude in the beam. The twiss functions are also periodic functions, with a period equal to the circumference of the machine  $C$ , and are related to each other and the betatron phase advance  $\phi_z(s)$  by:

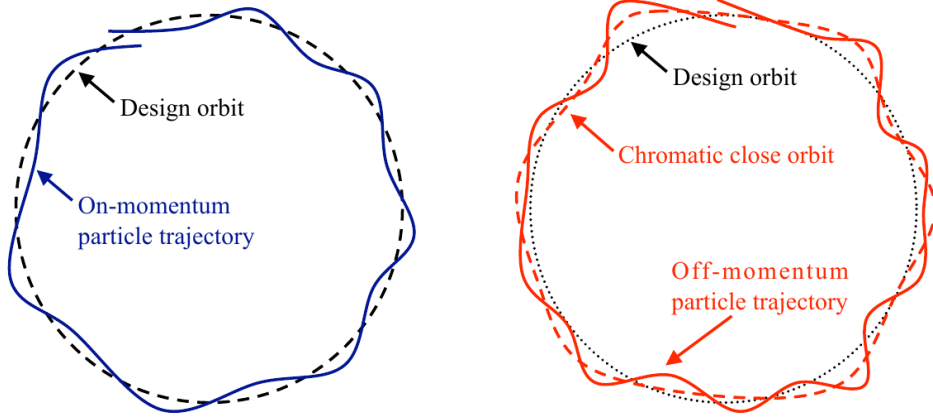
$$\begin{aligned} \alpha_{x,y}(s) &\equiv -\frac{1}{2}\beta'_{x,y}(s), \\ \gamma_{x,y}(s) &\equiv \frac{1 + \alpha_{x,y}^2(s)}{\beta_{x,y}(s)}, \\ \phi_{x,y}(s) &\equiv \int \frac{ds}{\beta_{x,y}(s)}. \end{aligned} \quad (2.11)$$

The horizontal and vertical tunes of a machine of circumference  $C$ , that practically give the number of betatron oscillations executed by particles traveling once around the ring, are then defined by:

$$Q_{x,y} = \frac{1}{2\pi} \int_0^C \frac{ds}{\beta_{x,y}(s)}. \quad (2.12)$$

### Matrix formulation for linear elements

Since the solution of Eqs. (2.7), (2.8) is not trivial if the whole accelerator is considered, it is rather easy if  $K_1$  is considered to be a piece-wise constant. The homogeneous equations (for

Figure 2.2: Emittance ellipses change due to different  $\delta p/p_0$  [22].

$\delta p/p_0 = 0$ ) can then be expressed in matrix formulation (only for linear elements as drifts, dipoles and quadrupoles) as:

$$\begin{pmatrix} z(s) \\ z'(s) \end{pmatrix} = M(s|s_0) \begin{pmatrix} z(s_0) \\ z'(s_0) \end{pmatrix}, \quad (2.13)$$

where  $z$  refers to the horizontal  $x$  or vertical  $y$  plane.

The transfer matrices for a constant focusing function  $K$  are:

$$M(s|s_0) = \begin{cases} \begin{pmatrix} \cos(\sqrt{K}l_q) & \frac{1}{\sqrt{K}} \sin(\sqrt{K}l_q) \\ -\sqrt{K} \sin(\sqrt{K}l_q) & \cos(\sqrt{K}l_q) \end{pmatrix} & K > 0: \text{focusing quad,} \\ \begin{pmatrix} 1 & s \\ 0 & 1 \end{pmatrix} & K = 0: \text{drift space,} \\ \begin{pmatrix} \cosh(\sqrt{|K|}l_q) & \frac{1}{\sqrt{|K|}} \sinh(\sqrt{|K|}l_q) \\ \sqrt{|K|} \sinh(\sqrt{|K|}l_q) & \cosh(\sqrt{|K|}l_q) \end{pmatrix} & K < 0: \text{defocusing quad.} \end{cases} \quad (2.14)$$

In thin-lens approximation, where the quadrupole length  $l_q \rightarrow 0$ , the transfer matrix for a quadrupole reduces to:

$$M_{\text{quad}} = \begin{pmatrix} 1 & 0 \\ -1/f & 1 \end{pmatrix}, \quad (2.15)$$

where the focal length is given by  $f = \lim_{l_q \rightarrow 0} \frac{1}{Kl_q}$ .

In a similar way, the transfer matrix of a sector dipole, for which the particle trajectories enter and exit with perpendicular entrance and exit angles to the edge of the dipole field, is given by:

$$M_{\text{dip}} = \begin{pmatrix} \cos \theta & \rho_x \sin \theta \\ -\frac{1}{\rho_x} \sin \theta & \cos \theta \end{pmatrix} \xrightarrow{\text{small-angle approximation}} M_{\text{dip}} = \begin{pmatrix} 1 & l_d \\ 0 & 1 \end{pmatrix}, \quad (2.16)$$

where  $\theta = l_d/\rho_x$  is the bending angle of the dipole,  $l_d$  is the dipole length and  $\rho_x$  is the bending radius.

One of the most important perturbations originates from the fact that the particle beams have a finite spread of energies about the nominal energy. The deflection of a particle with an

energy different than the nominal one in any magnetic or electric field will deviate from that for a particle with the nominal energy and will start oscillating around a chromatic closed orbit, as shown in Figure 2.2. For an off-momentum particle, the solution of the in-homogeneous Eq. (2.7) can be expressed as a linear superposition of the particular solution and the solution of the homogeneous equation (for  $\delta p/p_0 = 0$ ):

$$x = x_\beta(s) + D(s) (\delta p/p_0) , \quad (2.17)$$

where  $D(s) (\delta p/p_0)$  is the off-momentum closed orbit and  $D(s)$  is the dispersion function that determines the offset of the reference trajectory from the ideal path for particles with a relative energy deviation from the ideal momentum. The solution can then be expressed as:

$$\begin{pmatrix} D(s) \\ D'(s) \end{pmatrix} = M(s|s_0) \begin{pmatrix} D(s_0) \\ D'(s_0) \end{pmatrix} + \begin{pmatrix} d \\ d' \end{pmatrix} , \quad (2.18)$$

where  $d$  and  $d'$  is the dispersive part of the matrices.

The dispersive part of the matrices can be written in the form:

$$\begin{pmatrix} d \\ d' \end{pmatrix} = \begin{cases} \begin{pmatrix} \frac{1}{\rho_x K} (1 - \cos(\sqrt{K}l_q)) \\ \frac{1}{\rho_x \sqrt{K}} \sin(\sqrt{K}l_q) \end{pmatrix} & K > 0: \text{ focusing quad,} \\ \begin{pmatrix} \frac{1}{\rho_x |K|} (-1 + \cosh(\sqrt{|K|}l_q)) \\ \frac{1}{\rho_x \sqrt{|K|}} \sinh(\sqrt{|K|}l_q) \end{pmatrix} & K < 0: \text{ defocusing quad,} \\ \begin{pmatrix} \rho_x (1 - \cos \theta) \\ \sin \theta \end{pmatrix} & \text{sector dipole.} \end{cases} \quad (2.19)$$

In the small angle approximation the general transfer matrix with dispersion for a sector dipole is:

$$M = \begin{pmatrix} 1 & l_d & \frac{l_d \theta}{2} \\ 0 & 1 & \theta \\ 0 & 0 & 1 \end{pmatrix}. \quad (2.20)$$

The transfer matrix for any intervals, made up of sub-intervals, is the product of the transfer matrices of the sub-intervals:

$$M(s_2|s_0) = M(s_2|s_1)M(s_1|s_0) . \quad (2.21)$$

Using these matrices, the linear motion of particles can be tracked through the elements of the accelerator.

## Emittance and rms beam size

The motion of the particles in phase space follow the Liouville theorem [24], which states that under the influence of conservative forces the particle density in phase space stays constant. The

motion of an on-momentum particle at any point of the lattice is described by the solution of Eq. (2.7), which by using the Floquet solutions of Eq. (2.10), can be written in the form [23]:

$$\begin{aligned} x(s) &= \sqrt{\varepsilon_x} \sqrt{\beta_x(s)} \cos(\phi_x(s) + \phi_0), \\ x'(s) &= -\frac{\sqrt{\varepsilon_x}}{\sqrt{\beta_x(s)}} [\sin(\phi_x(s) + \phi_0) + a_x(s) \cos(\phi_x(s) + \phi_0)] . \end{aligned} \quad (2.22)$$

The position  $x(s), x'(s)$  satisfy the equation of an ellipse that depends on the optics parameters, as:

$$A_x = \gamma_x x^2 + 2\alpha_x x x' + \beta_x x'^2 . \quad (2.23)$$

This expression is the Courant-Snyder invariant, describing an ellipse with area  $\pi\varepsilon_x$ , with  $\varepsilon_x$  being the geometrical emittance. Practically, the beam emittance describes the region in phase space, that is always constant for a specific energy, occupied by the beam particles. In the case of acceleration, the quantity that is kept constant is called the normalized emittance and it is defined as  $\beta\gamma\varepsilon_x$ . Since the emittance depends on the twiss parameters around the ring, its shape changes at different positions. The geometrical meaning of the emittance is shown in Figure 2.3 (left). According to the particle distribution (e.g. homogeneous, Gaussian, etc.), the beam or

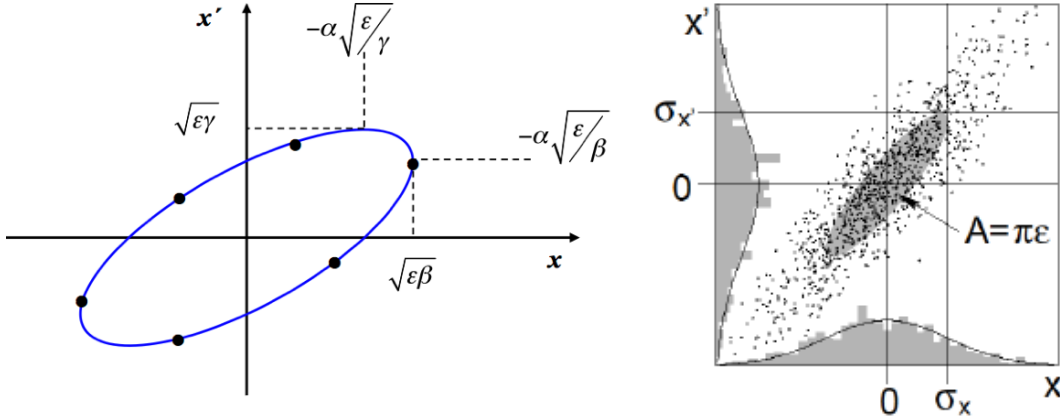


Figure 2.3: Left: The single particle emittance defined by the twiss parameters at a certain position in the lattice [25]. Right: Statistical beam emittance depending on the beam distribution [26].

statistical emittance is defined by a contour confining some fraction of particles, as:  $\varepsilon_x = \langle A_x \rangle$ . It is shown in the right part of Figure 2.3.

In the non-zero momentum deviation case, with  $\eta_x$  and  $\eta'_x$  being the dispersion function and its derivative, there is another invariant of the lattice, called the dispersion invariant that is defined as:

$$\mathcal{H}_x = \gamma_x \eta_x^2 + 2\alpha_x \eta_x \eta'_x + \beta_x \eta_x'^2 , \quad (2.24)$$

The beam size is determined by the beam emittance  $\varepsilon_x$ , the values of the betatron and the dispersion functions ( $\beta_x, \eta_x$ ) and the energy spread  $\sigma_{p0}$  at a specific point along the accelerator. So, it is a quantity that varies along the lattice [24]. The beam size is given by the standard

deviation of the distribution of the beam particles. In the case of a Gaussian beam distribution, the beam size is defined as:

$$\sigma_x(s) = \sqrt{\varepsilon_x \beta_x(s) + \eta_x^2(s) \sigma_{p0}^2} . \quad (2.25)$$

Similar expressions as the ones described above, are valid for the vertical plane too. If the three planes are fully uncoupled, three independent two-dimensional beam emittances (and sizes) can be defined.

## Dynamic aperture

The dynamic aperture (DA) is the stability region of phase space in an accelerator. Practically, the DA gives the maximum phase-space amplitude within which particles do not get lost as a consequence of single-particle effects [27]. The DA has to be at least equal or larger than the minimum beam transverse acceptance  $R_{\min}$ , that is defined in terms of a maximum emittance  $\varepsilon_{\max}$  (given by particles with the maximum betatron action in the beam) and of a maximum relative momentum deviation  $(\delta p/p_0)_{\max}$  [28] as:

$$R_{\min} = \sqrt{2\beta\varepsilon_{\max} + \eta(\delta p/p_0)_{\max}} . \quad (2.26)$$

The basic method for computing DA involves the use of a tracking code. A model of the ring is built within the code that includes an integration routine for each magnetic element. The particle is tracked many turns and stability is determined.

## Chromaticity

When passing through a quadrupole, particles in a beam having different momenta experience different focusing. Since the focusing strength depends on the energy of the particles, higher energy particles are focused less and lower energy particles are focused more than the ideal energy particles. The effect of different betatron oscillations or tunes due to different momentum deviations is called chromaticity and is defined as:

$$\xi_{x,y} = \frac{\partial Q_{x,y}}{\partial \delta} . \quad (2.27)$$

The chromaticity caused only by the linear elements of the lattice, is called the natural chromaticity and is defined as [23]:

$$\begin{aligned} \xi_x &= \frac{\partial Q_x}{\partial \delta} = -\frac{1}{4\pi} \int_{s_0}^{s_0+C} \beta_x(s) K_1(s) ds , \\ \xi_y &= \frac{\partial Q_y}{\partial \delta} = \frac{1}{4\pi} \int_{s_0}^{s_0+C} \beta_y(s) K_1(s) ds . \end{aligned} \quad (2.28)$$

Correction of the chromaticities can be accomplished by installing sextupole magnets <sup>1</sup> into the storage ring at locations where the dispersion is not zero. The dispersion makes higher energy particles gather more outside of the ideal orbit and lower energy particles more on the inside. If the natural chromaticity is large, the sextupole strengths needed for the chromaticity correction are strong, introducing strong non-linearities and reducing the dynamic aperture.

<sup>1</sup>Sextupoles can be considered as quadrupoles with varying focal strength across the horizontal aperture.

### Momentum compaction factor

Off-momentum particles on the dispersion orbit, travel in a different path length than on-momentum particles. The change of the path length with respect to the momentum spread is called momentum compaction factor [23]:

$$\alpha_p = \frac{\Delta C/C}{\delta p/p_0} . \quad (2.29)$$

The change in circumference for a particle with momentum  $p_0 + \delta p$  is:

$$\Delta C = \oint D \frac{\delta p}{p_0} d\theta = \oint D \frac{\delta p}{p_0} \frac{ds}{\rho_x} , \quad (2.30)$$

and thus, the momentum compaction factor can be written as:

$$\alpha_p = \frac{1}{C} \oint \frac{D(s)}{\rho_x(s)} ds = \left\langle \frac{D(s)}{\rho_x(s)} \right\rangle . \quad (2.31)$$

Practically, the momentum compaction factor increases only in curved sections where  $\rho_x \neq 0$ . Depending on the dispersion function being positive or negative, the path length is longer or shorter for higher energy particles ( $\delta p > 0$ ) respectively.

The revolution frequency of a reference particle, is defined as:

$$f = \frac{u}{2\pi\rho_x} = \frac{\beta c}{C} . \quad (2.32)$$

So, the change in the frequency for an off-momentum particle can then be written as:

$$\frac{\delta f}{f} = \left( \frac{1}{\gamma^2} - \alpha_p \right) \frac{\delta p}{p_0} , \quad (2.33)$$

where the factor  $(1/\gamma^2 - \alpha_p) \equiv \eta$  is called the slippage factor. There is an energy for which the velocity variation is compensated by the trajectory variation and corresponds to  $\eta = 0$ , i.e. the momentum compaction vanishes, that is:

$$\gamma_t = \frac{1}{\sqrt{\alpha_p}} , \quad (2.34)$$

is called the transition energy and plays an important role in phase focusing. At  $\gamma = \gamma_t$  the revolution period is independent of the particle's momentum and all particles around the accelerator will travel with equal revolution frequencies. Below the transition energy ( $\eta < 0$ ), a higher momentum particle will have shorter revolution period than the reference one, and will arrive at a fixed location earlier than the reference particle. Above transition energy ( $\eta > 0$ ) the opposite is true.

## 2.3 Longitudinal motion

As discussed in the beginning of this chapter, the position of a particle is described using a Cartesian coordinate system that moves with a reference particle. This particle has the design energy and

passes through the center of all the magnets, following the closed trajectory, with an angular revolution frequency of  $\omega_0 = 2\pi/T_0$ , for  $T_0$  being revolution period. The focusing and the acceleration in the longitudinal plane are obtained by the longitudinal component of the electric field in the RF cavities that is:

$$E_z = E_{z0} \sin(\omega_{\text{RF}}t + \phi_s), \quad (2.35)$$

where  $E_{z0}$  is the amplitude of the field,  $\phi_s$  is the phase of the synchronous particle and  $\omega_{\text{RF}}$  is the angular frequency of the RF system. The reference particle should be synchronized with the RF voltage (that is why it is often called the synchronous particle). So, the RF phase angle  $\phi = \omega_{\text{RF}}t$  should be the same every time the reference particle crosses an RF cavity. In order to achieve this synchronization, the RF frequency must be an integer multiple of the revolution frequency:  $\omega_{\text{RF}} = h\omega_0$ , where  $h$  is an integer called the harmonic number.

In the RF cavity, under the influence of an electric field having a RF voltage with amplitude  $V_0$ , a synchronous particle gains in each turn an amount of energy that is:

$$\Delta E_s = eV_0 \sin(\phi_s), \quad (2.36)$$

The phase of the RF voltage determines the particle's relative longitudinal position. The phase of an arbitrary non-synchronous particle is the deviation from the phase of the synchronous particle:  $\phi = \phi_s \pm \delta\phi$ . Similarly, the energy gain of a particle with a phase  $\phi$  is  $\Delta E_p = eV_0 \sin(\phi)$ . The energy gain per turn with respect to the energy gain of the synchronous particle is:

$$(\Delta E)_{\text{turn}} = \Delta E_p - \Delta E_s = eV_0(\sin \phi - \sin \phi_s). \quad (2.37)$$

Taking into account the slow change of energy with respect to the revolution frequency, the equation of motion for the energy difference is:

$$\frac{d}{dt} \left( \frac{\Delta E}{\omega_0} \right) = \frac{1}{2\pi} eV_0 (\sin \phi - \sin \phi_s), \quad (2.38)$$

or by using the fractional off-momentum deviation:

$$\frac{\delta p}{p_0} = \frac{\omega_0}{\beta^2 E_0} \frac{\Delta E}{\omega_0}, \quad (2.39)$$

Eq. (2.38) can be written as:

$$\frac{d}{dt} \left( \frac{\delta p}{p_0} \right) = \frac{\omega_0}{2\pi\beta^2 E_0} eV_0 (\sin \phi - \sin \phi_s). \quad (2.40)$$

where  $E_0$  is the energy of the synchronous particle and  $\beta$  the relativistic normalized velocity. The time evolution of the phase angle variable is:

$$\frac{d\phi}{dt} = -h(\omega - \omega_0) = -h\Delta\omega. \quad (2.41)$$

Replacing the slippage factor from Eq. (2.33) and then using Eq. (2.39), the phase equation becomes:

$$\frac{d\phi}{dt} = h\omega_0\eta \frac{\delta p}{p_0} = \frac{h\omega_0^2\eta}{\beta^2 E_0} \left( \frac{\Delta E}{\omega_0} \right). \quad (2.42)$$

Combining the energy and phase equations (2.38) and (2.42), the time evolution of the phase coordinate can be written as a second order differential equation:

$$\frac{d^2}{dt^2}(\phi - \phi_s) = \frac{h\omega_0^2 e V_0 \eta_0 \cos \phi_s}{2\pi\beta^2 E_0}(\phi - \phi_s). \quad (2.43)$$

This equation for the small angle oscillations corresponds to the equation of the harmonic oscillator, having an angular frequency:

$$\omega_s = \omega_0 \sqrt{\frac{heV_0 |\eta_0 \cos \phi_s|}{2\pi\beta^2 E_0}}, \quad (2.44)$$

while the synchrotron tune that is defined as the number of synchrotron oscillations per revolution, is:

$$Q_s = \frac{\omega_s}{\omega_0} = \sqrt{\frac{heV_0 |\eta_0 \cos \phi_s|}{2\pi\beta^2 E_0}}. \quad (2.45)$$

In order for the oscillating system to be stable, the expression under the square root in Eq. (2.44) must be positive. Except for  $\eta_0 \cos \phi_s$  all the parameters are positive, so, the stability condition of the synchrotron motion is given by:

$$\eta_0 \cos \phi_s < 0. \quad (2.46)$$

The stability criterion makes it clear that below transition energy ( $\eta_0 < 0$ ) the synchronous phase angle should be  $0 < \phi_s < \pi/2$  and above transition ( $\eta_0 > 0$ ) it should be  $\pi/2 < \phi_s < \pi$ .

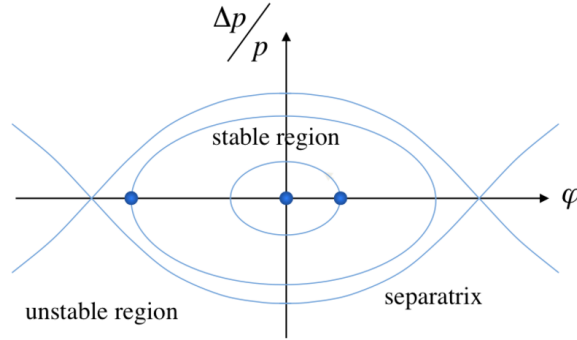


Figure 2.4: Trajectories of particles in the longitudinal phase space. The separatrix defines the limit of stable motion.

In the longitudinal phase space, the particle trajectory has two different types of fixed points, when the derivative of the coordinates with respect to time is zero ( $d\phi/dt = 0$  and  $dE/dt = 0$ ). Its motion is described by distorted circles in the vicinity of  $\phi_s$  that is a stable fixed point. For phases beyond  $\pi - \phi_s$ , which is an unstable fixed point, the motion is unbounded as shown in Figure 2.4 (unstable region). The region of stable motion that describes closed trajectories around a stable fixed point is also illustrated. Acceleration of bunched beams is only possible for particles inside this region, which is called an RF bucket. The limit of this region is determined

by a curve passing through  $\pi - \phi_s$ , known as the separatrix. The height of the separatrix is called momentum acceptance and is defined by:

$$\left(\frac{\delta p}{p_0}\right)_{\max} = \mp \sqrt{\frac{eV_0}{\pi h \alpha_p E_0} (2 \cos \phi_s + (2\phi_s - \pi) \sin \phi_s)}, \quad (2.47)$$

where  $\alpha_p$  is the momentum compaction factor.

In order to avoid particle losses, the particles of a bunch are often not distributed over the full RF bucket but are restricted to a certain fraction of the phase space. The phase-space area filled by a bunch is called the longitudinal beam emittance and is defined as:

$$\varepsilon_l = \oint \frac{\Delta E}{h\omega_0} d\phi, \quad (2.48)$$

## 2.4 Synchrotron radiation and damping

The electromagnetic radiation emitted when charged particles are accelerated radially is called synchrotron radiation (SR). Practically, it is the consequence of the finite value of the speed of light. Electric fields extend infinitely into space from charged particles in uniform motion. When these particles are accelerated and their velocity approaches the velocity of light, parts of these fields cannot catch up with the particle anymore, giving rise to SR. The angular distribution of

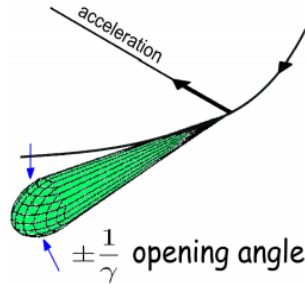


Figure 2.5: The angular distribution of synchrotron radiation (lab frame) [29].

SR is sharply peaked in the direction of the electron velocity vector within an angular width of  $1/\gamma$ , as can be seen in Fig. 2.5.

The radiation power of an accelerated particle having a momentum  $p = m_0 u$ , is given by Larmor's formula [30]:

$$P_s = \frac{e^2}{6\pi\epsilon_0 m_0^2 c^3} \left(\frac{dp}{dt}\right)^2, \quad (2.49)$$

with  $e$  and  $m_0$  being the particle charge and rest mass respectively,  $c$  the speed of light and  $\epsilon_0$  the permittivity of free space. It is clear from this formula that the electromagnetic energy is emitted only when  $dp/dt \neq 0$ , i.e. the momentum of the particle changes and that is a result of an applied force. The closer is a particle's velocity to the speed of light the stronger is the effect of radiation, the opposite happens for non-relativistic particles. The radiation power for

relativistic particles is given by:

$$P_s = \frac{e^2 c}{6\pi\epsilon_0(m_0 c^2)^2} \left[ \left( \frac{dp}{d\tau} \right)^2 - \frac{1}{c^2} \left( \frac{dE}{d\tau} \right)^2 \right]. \quad (2.50)$$

In the case of linear acceleration this reduces to:

$$P_s = \frac{e^2 c}{6\pi\epsilon_0(m_0 c^2)^2} \left( \frac{dp}{\gamma d\tau} \right)^2 = \frac{e^2 c}{6\pi\epsilon_0(m_0 c^2)^2} \left( \frac{dp}{dt} \right)^2. \quad (2.51)$$

Then the power radiated from linearly accelerated particles, using  $dp/dt = dE/dx$ , becomes:

$$P_s = \frac{e^2 c}{6\pi\epsilon_0(m_0 c^2)^2} \left( \frac{dE}{dx} \right)^2. \quad (2.52)$$

For particles traveling in a circular path, the general radiation formula is given by:

$$P_s = \frac{e^2 c}{6\pi\epsilon_0(m_0 c^2)^2} \left( \frac{dp}{d\tau} \right)^2 = \frac{e^2 c \gamma^2}{6\pi\epsilon_0(m_0 c^2)^2} \left( \frac{dp}{dt} \right)^2. \quad (2.53)$$

Comparing Eq. (2.53) with Eq. (2.52) shows that the radiation from circular motion is at least a factor of  $\gamma^2$  larger than that from longitudinal acceleration. The change of momentum in a circular path through an angle  $d\theta$  is  $dp = p d\theta$ . If  $\rho$  is the bending radius, it is  $\frac{dp}{dt} = p\omega = p \frac{u}{\rho}$ . Considering the fact that  $E = pc$  for extremely relativistic particles, that are the ones that radiate more, results in what is called synchrotron radiation and is given by Liénard's formula:

$$P_s = \frac{e^2 c}{6\pi\epsilon_0} \frac{1}{(m_0 c^2)^4} \frac{E^4}{\rho^2}, \quad (2.54)$$

So, the SR power is proportional to the fourth power of the energy  $E$  and inversely proportional to the fourth power of  $m_0$ . In order to understand the dependence of the SR power on the rest mass, the radiated power from an electron is compared to that from a proton of the same energy, as:

$$\frac{P_{s,e}}{P_{s,p}} \simeq 10^{13}. \quad (2.55)$$

Clearly, SR plays a dominant role in the case of electrons and positrons, however for protons it becomes important only for energies higher than 1 TeV [30].

In circular accelerators, the energy loss per revolution period from a particle with energy  $E$  is given by:

$$U_0 = \oint P dt = \frac{C_\gamma}{2\pi} E^4 \oint \frac{1}{\rho^2} ds, \quad (2.56)$$

where  $C_\gamma = \frac{4\pi}{3} \frac{r_0}{(m c^2)^3}$ ; that is  $8.846 \times 10^{-5}$  m/GeV<sup>3</sup> for electrons and  $7.783 \times 10^{-18}$  m/GeV<sup>3</sup> for protons. Due to the fact that the radiation power is proportional to  $E^4/\rho^2$ , the higher the particle energy is the more energy the particle loses.

### SR damping mechanism

The reduction of the particles momenta due to SR happens in all planes. A RF field is used to compensate the energy loss but this is done only in the longitudinal plane. This leads to steady reduction of the transverse betatron oscillation or to what is called synchrotron damping. A schematic representation of the effect is shown in Figure 2.6. The initial momentum  $p_0$  is reduced down to  $p_1$  because of the SR emission and afterwards, due to the energy kick from the RF cavity, the new momentum is  $p_2$ .

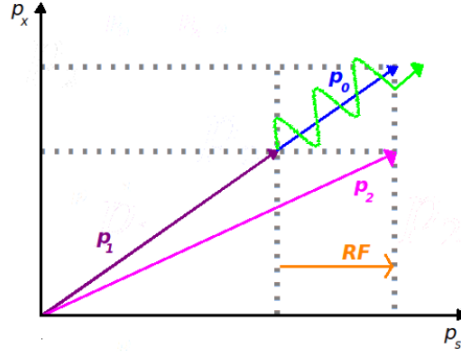


Figure 2.6: The damping mechanism due to synchrotron radiation [26].

The oscillation amplitudes in the transverse and longitudinal plane are damped like:  $A_i = A_{i0}e^{-\alpha_i t}$ , where  $i = x, y, s$  and  $\alpha_i$  are the damping increments which are equivalent to the damping term of the harmonic oscillation with a frictional force. Taking into account the different, dispersive, orbit of off-momentum particles, the damping increments can be written in the form:

$$\alpha_{s,y,x} = \frac{U_0}{2ET_0} \mathcal{J}_{s,y,x}, \quad (2.57)$$

with  $\mathcal{J}_x, \mathcal{J}_y, \mathcal{J}_s$  being the damping constants:  $\mathcal{J}_s = 2 + \mathcal{D}$ ,  $\mathcal{J}_y = 1$ ,  $\mathcal{J}_x = 1 - \mathcal{D}$ , and

$$\mathcal{D} = \frac{\oint \left[ \frac{\eta}{\rho_x} \left( 2k + \frac{1}{\rho_x^2} \right) \right]}{\oint \frac{ds}{\rho_x^2}},$$

where  $\eta$  is the dispersion function,  $\rho_x$  the radius of curvature and  $k$  the quadrupole focusing strength. The corresponding damping times defined as  $1/\alpha_i$ , for  $T_0$  being the revolution period, are given by:

$$\tau_{x,y,s} = \frac{2E_0 T_0}{\mathcal{J}_{x,y,s} U_0}. \quad (2.58)$$

According to the Robinson Theorem, the sum of the three damping constants is invariant [23]:  $\mathcal{J}_x + \mathcal{J}_y + \mathcal{J}_s = 4$ . The beam parameters in a circular accelerator are modified due to synchrotron radiation, and they can be expressed through the radiation integrals which are [27]:

$$I_1 = \oint \frac{\eta_x}{\rho_x} ds, \quad I_2 = \oint \frac{1}{\rho_x^2} ds, \quad I_3 = \oint \frac{1}{|\rho_x^3|} ds,$$

$$I_4 = \oint \frac{\eta_x}{\rho_x} \left( \frac{1}{\rho_x^2} - 2K_1 \right) ds = \oint \frac{(1-2n)\eta_x}{\rho_x^3} ds, \quad I_5 = \oint \frac{\mathcal{H}_x}{|\rho_x^3|} ds. \quad (2.59)$$

The damping partition numbers are defined through the radiation integrals as:

$$\mathcal{J}_x = 1 - \frac{I_4}{I_2}, \quad \mathcal{J}_y = 1, \quad \mathcal{J}_s = 2 + \frac{I_4}{I_2}. \quad (2.60)$$

Due to the quantum nature of synchrotron radiation, the emission of photons is discrete and random, and the quantum process causes diffusion and excitation. The beam eventually reaches an equilibrium distribution that is determined by a balance between radiation damping and quantum excitation [27].

## 2.5 Equilibrium beam properties

For Gaussian equilibrium distributions with parameters defined by the damping times and the respective diffusion coefficients [24], the emittance evolution with time is given by:

$$\varepsilon_x(t) = \varepsilon_{x,\text{inj}} e^{-2t/\tau_x}, \quad \varepsilon_y(t) = \varepsilon_{y,\text{inj}} e^{-2t/\tau_y}, \quad \sigma_p^2(t) = \sigma_{p,\text{inj}} e^{-2t/\tau_p}, \quad (2.61)$$

where the index ‘‘inj’’ refers to the injected beam emittances and energy spread and  $\tau_x$ ,  $\tau_y$ ,  $\tau_p$  are the horizontal, vertical and longitudinal damping times respectively.

### Horizontal and vertical emittance

The relativistic particles that pass through bending magnets emit synchrotron radiation, a process that leads to quantum excitation and damping. The quantum excitation of the oscillation amplitude is compensated by damping and an equilibrium is reached when these effects are of equal strength. The equilibrium horizontal beam emittance is defined as [23]:

$$\varepsilon_{x0} = C_q \gamma^2 \frac{\langle \mathcal{H}_x / |\rho_x^3| \rangle}{\mathcal{J}_x \langle 1/\rho_x^2 \rangle} = C_q \gamma^2 \frac{I_5}{I_2 - I_4}. \quad (2.62)$$

It scales as the square of the beam energy  $\gamma$  and it depends on the bending radius  $\rho_x$  and the dispersion invariant  $\mathcal{H}_x$ , defined in Eq. (2.24). It can be adjusted by appropriate choice of the optics functions along the bending magnets. For electrons it is  $C_q = \frac{55}{32\sqrt{3}} \frac{hc}{mc^2} = 3.8319 \times 10^{-13}$  m and for protons it is  $C_q = 0.0021 \times 10^{-13}$  m.

Similarly to the horizontal emittance, the contribution of vertical dispersion to vertical emittance is [23]:

$$\varepsilon_{y0} = C_q \gamma^2 \frac{\langle \mathcal{H}_y / |\rho_y^3| \rangle}{\mathcal{J}_y \langle 1/\rho_y^2 \rangle}. \quad (2.63)$$

In order to minimize this effect, correction of the equilibrium orbit and the perturbation to the dispersion function is needed.

In the absence of vertical dispersion or coupling,  $\mathcal{H}_y = 0$  and the vertical emittance is defined only by the opening angle of synchrotron radiation. The synchrotron radiation photons are emitted with an rms angle of  $1/\gamma$ , relative to the particle trajectory, affecting both the longitudinal

and transverse momenta of the particle, defining a lower (the so-called quantum) limit of vertical emittance:

$$\varepsilon_{y0,\min} = \frac{13 C_q}{55 \mathcal{J}_y} \frac{\oint \frac{\beta_y}{|\rho_y|^3} ds}{\oint \frac{1}{\rho_y^2} ds} . \quad (2.64)$$

However, this is negligible and the vertical emittance is mainly defined by vertical dispersion, due to alignment errors and by betatron coupling, if we do not take into account any current depended or collective effects. The contribution of vertical dispersion to vertical emittance is:

$$\varepsilon_{y0,d} \approx \mathcal{J}_s \langle \mathcal{H}_y \rangle \sigma_{p0}^2 , \quad (2.65)$$

while the contribution of weak coupling to vertical emittance is:

$$\varepsilon_{y0,k} = k \varepsilon_{x0} , \quad (2.66)$$

where  $\sigma_{p0}$  is the rms relative momentum deviation and  $k$  the coupling factor.

In the presence of both vertical dispersion and betatron coupling, the vertical emittance is the sum of the above expressions:

$$\varepsilon_{y0} = \varepsilon_{y0,\min} + \varepsilon_{y0,d} + \varepsilon_{y0,k} . \quad (2.67)$$

The index 0 in all the equilibrium properties expressions, refers to the absence of any current depended effects, thus to the case of nearly zero current.

### Energy spread, bunch length and longitudinal emittance

The statistical emission of photons causes a change of particle energy, leading to an energy spread within the beam. The interplay between the quantized emission of photons and the SR damping which reduces the synchrotron oscillation amplitude, determine the beam energy spread. As the emission of photons is a statistical process and the RF cavity recovers only the average energy loss, there is a subsequent rms equilibrium energy spread in the beam [23]:

$$\sigma_{p0}^2 = \left( \frac{\delta E}{E} \right)^2 = C_q \gamma^2 \frac{\langle |1/\rho_x^3| \rangle}{\mathcal{J}_s \langle 1/\rho_x^2 \rangle} = C_q \gamma^2 \frac{I_3}{2I_2 + I_4} , \quad (2.68)$$

For separated function magnets, it depends only on the particle energy and the bending radius, where for combined function magnets the partition number  $\mathcal{J}_s$  can be modified accordingly to vary the energy spread.

A spread of particle energy can also be translated as a spread in the longitudinal phase. For circular electron accelerators the bunches are small compared to the bucket area and the small amplitude approximation is valid. In these terms, the rms relative energy spread  $\sigma_p$  and rms bunch length  $\sigma_s$  [m] are related through:

$$\sigma_{s0} = \sigma_{p0} C \sqrt{\frac{\alpha_p E}{2\pi h (eV_0^2 - U_0^2)^{1/2}}} , \quad (2.69)$$

where  $\alpha_p$  is the momentum compaction factor,  $C$  the ring circumference,  $V_0$  the amplitude of the RF voltage,  $h$  the harmonic number and  $U_0$  the energy loss per turn.

The zero current equilibrium longitudinal emittance is defined as the product of the equilibrium energy spread and bunch length:

$$\varepsilon_l = \sigma_{p0} \sigma_{s0} . \quad (2.70)$$

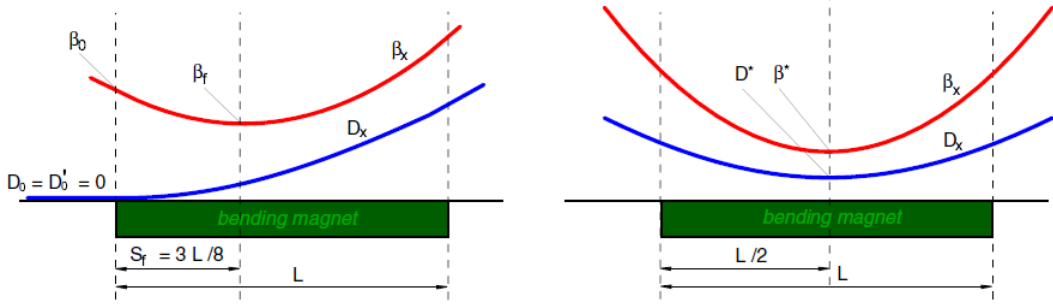


Figure 2.7: The two basic layouts for low emittance lattices. Left: the achromat condition. Right: the symmetry condition [31].

## 2.6 Low emittance lattices

The lattice design of modern  $e^+/e^-$  rings, such as light sources or damping rings is focused on the minimization of the emittance. As mentioned earlier (see paragraph 2.5), the equilibrium beam emittance depends on the mean value of the dispersion invariant  $\mathcal{H}_x(s)$  in the dipoles. In order to minimize the emittance, the minimization of  $\langle \mathcal{H}_x \rangle$  is necessary. Knowing the twiss parameters at the entrance of the dipole, the  $\mathcal{H}_x$  function can be determined at any point within a bending magnet, using Eq. (2.24). Assuming a lattice where the optics functions are the same in all dipoles, the average value in the ring is:

$$\langle \mathcal{H}_x \rangle = \frac{1}{L_d} \int_0^{L_d} \mathcal{H}_x(s) ds, \quad (2.71)$$

where  $L_d$  the length of the dipole magnet with constant bending radius  $\rho_x$ .

The two basic layouts used to minimize the  $\langle \mathcal{H}_x \rangle$  are shown in Fig. 2.7. The one (left) imposes an achromat condition of vanishing dispersion, i.e.  $\eta_x = \eta'_x = 0$  in the entrance (or exit) of the bending magnet and the other one (right) imposes a symmetry condition, i.e. both beta ( $\beta_x$ ) and dispersion ( $\eta_x$ ) functions have a minimum at the center of the bending magnets ( $\alpha_x = \eta'_x = 0$ ). The first layout is mainly used in light sources, where many dispersion free regions are required for the insertion of the synchrotron radiation beam lines. The second layout provides emittance minimization in a more compact ring and that is why it is used in DR. For  $\mathcal{F}_{\text{lattice}}$  being the scaling factor that depends on the lattice design, the equilibrium emittance can be written in the form:

$$\varepsilon_{x0} = \mathcal{F}_{\text{lattice}} C_q \gamma^2 \theta^3. \quad (2.72)$$

An example of a low emittance lattice that is the most common one in high brilliance light sources is the Double Bend Achromat (DBA) or basic Chasman-Green cell which consists of two dipoles and either a focusing quad (basic scheme) or a triplet (extended scheme) between them. Applying the achromat condition, with  $\beta_{x0} = \sqrt{12/5}L$  and  $\alpha_{x0} = \sqrt{15}$  at the entrance of the dipole, the minimum emittance for the DBA cell is given for a scaling factor that is:

$$\mathcal{F}_{DBA} = \frac{1}{4\sqrt{15}\mathcal{J}_x}. \quad (2.73)$$

### The Theoretical Minimum Emittance cell

The emittance can be further minimized, if the achromat condition is not necessary for the lattice design. The optimal configuration to achieve the absolute theoretical minimum emittance (TME) is the TME cell [32]. It consists of one dipole and of two quadrupole families, resulting in a structure that is more compact than the DBA one. The theoretical minimum emittance can be achieved if the symmetry condition, shown in Fig. 2.7 (right), is satisfied. The scaling factor for the theoretical minimum emittance is equal to:

$$\mathcal{F}_{TME} = \frac{1}{12\sqrt{15}\mathcal{J}_x}, \quad (2.74)$$

with  $\eta_{xc} = \frac{\theta L}{24}$  and  $\beta_{xc} = \frac{L}{2\sqrt{15}}$  at the center of the dipole. The minimum emittance in this case is a factor of 3 smaller than in the DBA lattice.

Due to the compactness and the very small emittance the TME cells reach, they are preferred for the Damping Rings lattice design. The performance of these cells was precedently studied for the case of uniform dipoles [33]. In this thesis, a further minimization of the TME cell emittance when using longitudinally variable bends instead of uniform dipoles is discussed in detail. In order to have a global understanding of all cell properties, analytical solutions for a TME cell with a variable bend are described in Chapter 4.

In general, tuning the low emittance lattices to the minimum emittance is difficult. That is because of the high chromaticities due to the strong quadrupole strengths needed for the low dispersion and beta functions, which can lead to a strongly nonlinear motion and a limited dynamic aperture (DA). Therefore, the main challenges of the design is to build a compact lattice, attaining a sufficiently low emittance and an adequately large DA.

## 2.7 Insertion devices

In addition to the SR that is unavoidably emitted in the bending magnets of a synchrotron, dedicated insertion devices are used to generate brighter SR beams for light sources or fast damping for cases as linear collider damping rings. These devices are formed by a sequence of short dipole fields of alternating polarity and they are installed along the particles beam path. The undulators and wigglers are two types of insertion devices that have different bending field strengths, i.e. they produce different radiation characteristics. The weaker beam bending of an undulator, generates constructive coherent radiation with very high intensity that is useful for the light sources experiments. A strong field wiggler, that gives a spectrum similar to that of a bending magnet, results in fast damping times that are important for the damping ring performance.

After passing through an insertion device, the beam should return to its nominal orbit, otherwise, a closed orbit distortion occurs around the machine. As the insertion devices do not contribute to the bending of the beam, long straight sections must be provided within the accelerator to accommodate them. The presence of insertion devices may induce perturbations due to the magnetic field of the device, which results in linear optics distortion, tune shifts, resonance excitation and reduction of dynamic aperture. In addition, the radiation emitted by the beam in the insertion device changes the emittance and energy spread of the beam [34].

## Wigglers

The insertion of damping wigglers along the particle beam path gives rise to fast damping and quantum excitation, resulting in different equilibrium states and damping times. For short wiggler poles, the magnetic field can be expressed as:

$$B_y(x, y = 0, z) = B_0 \sin \frac{2\pi z}{\lambda_p}, \quad (2.75)$$

where  $B_0$  the wiggler peak field and  $\lambda_p$  the wiggler period. With  $(B\rho_x)$  being the magnetic rigidity and  $B_w$  the wiggler field, the wiggler radius is defined by:

$$\rho_w = \frac{(B\rho_x)}{B_w} \quad \text{or} \quad \rho_w[m] = \frac{0.0017\gamma}{B_w[T]}. \quad (2.76)$$

The damping wigglers need to be placed in a dispersion free region, as the existence of dispersion in a wiggler region can lead to emittance blow up. For the CLIC DRs case, it is possible to place the wiggler magnets at the dispersion free long straight sections (LSS) which have a FODO structure. The FODO cells have been used as the building blocks of high energy colliders and storage rings due to their simplicity.

## 2.8 Collective effects

Due to their charges, beam particles interact with each other within the beam they belong to, with particles of the beam they collide with and with their environment. In a very general sense, the collective effects can be summarized in three categories: beam-self, beam-beam, and beam-environment. One of the most studied beam-self collective effects is generated by the space charge force, which refers to the force acting on one particle by the self field produced by the particle distribution. The other main beam-self processes called intrabeam scattering (discussed in Chapter 3) and Touschek effect, are a result of the compression of a large number of charged particles into a small volume which increases the probability for collisions of particles within the same beam. The main beam-beam effect in circular colliders is caused because the particles in one beam feel the electric and magnet forces of the particles in the other beam when passing through each other at certain interaction points. Another beam-beam effect is the electron-proton instability that is generated when the protons beam interacts with ambient electrons in the vacuum chamber, if electrons live until the beam returns on the next pass, the electron cloud grows until it causes an instability in the proton beam or drive a slow process of emittance growth. Since particles travel in the accelerator environment with beam pipes, magnets, etc, they induce fields (called wakefields) in the accelerator structures which can act back on a trailing particle <sup>2</sup>. Such effects belong to the beam-environment category of the collective effects. A successful accelerator design necessitates the full understanding of all collective effects and instabilities, since they have a significant contribution to beam dynamics.

---

<sup>2</sup>In practice, it can be very difficult to calculate the wakefield for real accelerator beams and vacuum chamber geometries. It is often easier to work with the Fourier transform of the wakefield, namely the impedance.

# Intrabeam Scattering

---

One of the statistical processes causing a spreading of particles in phase space or a continuous increase of beam emittance is the small angle multiple Coulomb scattering effect between charged particles within accelerator beams, called Intrabeam scattering (IBS). In cases where this diffusion is due to the particle density, the emittance growth may decrease significantly because the scattering occurrence drops to lower and lower values as the particle density decreases. IBS plays an important role in  $e^+/e^-$  damping rings, high intensity/low energy light sources [19] and high intensity hadron [17] and ion [18] circular machines. The scattering results are different when operating below or above transition. Below transition, the small-angle scattering is analogous to collisions of particles in a gas that lead to an equilibrium beam distribution. Above transition, this is no longer valid and both the transverse emittances and energy spread can all grow indefinitely. In this section, the standard IBS theories are summarized.

Closely related to IBS is the Touschek effect [35] that describes the elastic Coulomb collisions of particles in high intensity bunches, which results in particles being ejected from the beam. The probability for elastic collisions between particles is further enhanced considering that particles perform transverse betatron as well as longitudinal synchrotron oscillations. The colliding particles exchange momentum, leading to a change in their oscillation amplitudes. In each degree of freedom there are specific acceptance limits, if the particles amplitudes exceeds them they can get lost, leading to a reduction of the beam lifetime. In many high brightness synchrotron radiation light sources the beam current is limited by the Touschek lifetime.

## 3.1 Theories of Intrabeam Scattering

The IBS theory for accelerators was firstly introduced by Piwinski [36] and extended by Martini [37], establishing a formulation called the standard Piwinski (P) method. Later, Bjorken and Mtingwa (BM) [38] used a different approach to describe the effect, taking into account the strong focusing effect. The Modified Piwinski (MP) method [39] that includes the strong focusing effect, was developed by Bane. Some approximations of these theories are the high energy one by Bane (Bane) [39] and the completely integrated modified Piwinski (CIMP) [40]. These approximations are valid under certain conditions. A different approach that was developed for hadron beams and that is based on a Boltzmann type integro-differential equation, includes betatron coupling [41].

The horizontal ( $x$ ), vertical ( $y$ ) and longitudinal ( $p$ ) growth rates for the aforementioned theories are defined as:

$$\frac{1}{T_p} = \frac{1}{\sigma_p} \frac{d\sigma_p}{dt}, \quad \frac{1}{T_x} = \frac{1}{\varepsilon_x^{1/2}} \frac{d\varepsilon_x^{1/2}}{dt}, \quad \frac{1}{T_y} = \frac{1}{\varepsilon_y^{1/2}} \frac{d\varepsilon_y^{1/2}}{dt}, \quad (3.1)$$

with

$$\frac{1}{T_i} = \langle f_i \rangle, \quad (3.2)$$

where the functions  $f_i$  are integrals that have a complicated dependence on the beam properties, due to the coupling of the three planes through dispersion<sup>1</sup>. Some of these properties are the bunch charge and energy, the beam optics and the equilibrium rms horizontal, vertical emittances and the energy spread. The growth rates are determined by the average of the  $f_i$  functions along the ring and have a  $1/\gamma^4$  dependence. This means that IBS effects diminish with increasing beam energy.

In all IBS theories, the growth rates depend on the 6-dimensional invariant phase space volume of a bunched beam that is given by:

$$A = \frac{cNr_0^2}{64\pi^2\beta^3\gamma^4\varepsilon_x\varepsilon_y\sigma_s\sigma_p}, \quad (3.3)$$

where  $r_0$  is the classical particle radius, with  $r_0 = 2.82 \times 10^{-15}$  m for electrons or positrons and  $1.53 \times 10^{-18}$  m for protons.  $c$  is the speed of light,  $N$  the number of particles per bunch,  $\beta$  the particle velocity divided by  $c$ ,  $\gamma$  the Lorentz energy factor and  $\sigma_s$  the rms bunch length. The dependence of the density factor  $A$  on  $N$  and on  $1/\gamma^4$  makes it clear that IBS is stronger for high particle densities and that it is greatly reduced for high beam energies.

### The Coulomb log factor

For scattering calculations like IBS, a logarithmic Coulomb factor is used to include the contribution of events having a very large and very small impact parameter. The typical way of computing a log factor overemphasizes the importance of the very small impact parameter events for which the tails of the steady-state bunch distributions are non-Gaussian. In the high energy approximation by Bane [19], in order to describe the size of the core of the bunch, the Coulomb log factor is calculated as was first proposed by Raubenheimer [42], i.e. based on a boundary between the contribution to the core and the tails.

In B-M, Bane and CIMP methods, the Coulomb factor is defined as the ratio of the maximum  $r_{\max}$  to the minimum  $r_{\min}$  impact parameter in the collision of two particles in the bunch, that is  $(\log) \equiv \ln(r_{\max}/r_{\min})$ . For typical flat beams, the  $r_{\max}$  is taken to be equal to the vertical beam size  $\sigma_y$ , while  $r_{\min}$  is taken to be  $r_{\min} = r_0\beta_x/(\gamma^2\varepsilon_x)$ . Then, the Coulomb factor can be written as:

$$(\log) = \ln \left( \frac{\gamma^2\varepsilon_x\sqrt{\beta_y\varepsilon_y}}{r_0\beta_x} \right). \quad (3.4)$$

Piwinski always seems to underestimate the IBS effect with respect to the other theoretical models. What diversifies Piwinski's method, is the different definition of the Coulomb factor. In the Piwinski formalism, the maximum impact parameter which is typically taken as the vertical beam size appears. In the high energy limit, with  $d$  being the maximum impact parameter, the

---

<sup>1</sup>The dispersion couples the betatron and synchrotron oscillations, i.e. the particle's momentum change in a non zero dispersion region leads to a change in the betatron oscillations

Coulomb (*log*) for Piwinski can be written as [43]:

$$(\log) = \ln \left( \frac{d\sigma_H^2}{4r_0\alpha^2} \right), \quad (3.5)$$

where  $a = \frac{\sigma_H}{\gamma} \sqrt{\frac{\beta_x}{\varepsilon_x}}$ . Comparing the (*log*) factors of Eq. (3.4) and (3.5), then  $d = 4\sigma_y$ . If the parameter  $d$  is chosen such that we have an effective Coulomb log factor which is the same as the one of Eq. (3.4), then Piwinski agrees with the other models.

## 3.2 Equilibrium emittances due to IBS

In the presence of IBS, the performance of the beam can be described via an invariant that depends on the sum of the emittance mean values in all planes. Piwinski showed that this emittance dependent invariant [36] is:

$$\varepsilon_l \left( \frac{1}{\gamma^2} - \left\langle \frac{\eta_x^2}{\beta_x^2} \right\rangle - \left\langle \frac{\eta_y^2}{\beta_y^2} \right\rangle \right) + \left\langle \frac{\varepsilon_x}{\beta_x} \right\rangle + \left\langle \frac{\varepsilon_y}{\beta_y} \right\rangle = \text{const}, \quad (3.6)$$

where  $\varepsilon_l$  is the longitudinal emittance. Equation (3.6) shows that, below transition ( $\gamma^2 < \gamma_{tr}^2 = 1/\alpha_p \approx 1/\langle \eta_x^2 \beta_x^2 \rangle$ ) the sum of the three (positive) invariants is limited, and an equilibrium can exist. Above transition,  $\varepsilon_s$ ,  $\varepsilon_x$  and  $\varepsilon_y$  can grow simultaneously and an equilibrium does not exist. Although electron rings run normally above transition, where IBS leads to continuous emittance growth and equilibrium does not exist, synchrotron radiation damping counteracts the IBS growth, leading to new steady-state emittances.

The emittance growths for electron accelerators are in most cases negligible compared to radiation damping. However, they become significant in proton and ion storage rings where high particle densities and long storage times are required. The steady state properties, for which  $\frac{d\varepsilon_x}{dt} = \frac{d\varepsilon_y}{dt} = \frac{d\sigma_p^2}{dt} = 0$ , are expressed using the growth rates as:

$$\varepsilon_{x,y} = \frac{\varepsilon_{x0,y0}}{1 - \tau_{x,y}/T_{x,y}} \quad \text{and} \quad \sigma_p^2 = \frac{\sigma_{p0}^2}{1 - \tau_p/T_P}, \quad (3.7)$$

where  $\varepsilon_{x0}$ ,  $\varepsilon_{y0}$ ,  $\sigma_{p0}$  are the zero-current (without the effect of IBS) equilibrium horizontal and vertical emittances and rms energy spread.  $\tau_x$ ,  $\tau_y$  and  $\tau_p$  are the synchrotron radiation damping times. Equations 3.7 can be written in a differential form, describing the evolution of the horizontal, vertical emittance and energy spread with time:

$$\begin{aligned} \frac{d\varepsilon_{x,y}}{dt} &= -\frac{2}{\tau_{x,y}}(\varepsilon_{x,y} - \varepsilon_{x0,y0}) + \frac{2\varepsilon_{x,y}}{T_{x,y}(\varepsilon_x, \varepsilon_y, \sigma_p)}, \\ \frac{d\sigma_p}{dt} &= -\frac{1}{\tau_p}(\sigma_p - \sigma_{p0}) + \frac{\sigma_p}{T_p(\varepsilon_x, \varepsilon_y, \sigma_p)}. \end{aligned} \quad (3.8)$$

### 3.3 IBS in MAD-X

The general formalism of Bjorken-Mtingwa (B-M) following the approach of Conte and Martini [37], but including the effect of vertical dispersion was implemented in the Methodical Accelerator Design code MAD-X since 2006 [44]. This implementation included several bug fixes, the modified routine was crosschecked with the Mathematica implementation of the B-M formalism for the CLIC DR and the SLS lattices [45] and the correct implementation was then available in MAD-X [20]. The B-M formalism takes into account the variation of the lattice parameters (beta and dispersion functions) around the machine and consequently, the knowledge of the optical functions along the machine is required. IBS calculates the values at the center of each element by performing a linear interpolation between the last values of the previous element and the last values of the current element.

#### The Bjorken-Mtingwa formalism

Bjorken and Mtingwa [38] describe the IBS effect based on the relativistic "Golden Rule" for the transition rate due to a 2-body scattering process. For  $i = p, x, y$  being the index that respectively corresponds to the longitudinal and transverse planes, the growth times for the relative energy spread and the transverse emittances are:

$$\frac{1}{T_i} = 4\pi A(\log) \left\langle \int_0^\infty d\lambda \frac{\lambda^{1/2}}{[\det(L + \lambda I)]^{1/2}} \left\{ Tr L^{(i)} Tr \left( \frac{1}{L + \lambda I} \right) - 3 Tr L^{(i)} \left( \frac{1}{L + \lambda I} \right) \right\} \right\rangle, \quad (3.9)$$

with  $A$  being the density factor given in Eq. 3.3 and  $(\log)$  being the Coulomb factor given in Eq. 3.4. The auxiliary matrices are given in Appendix A.

### 3.4 The multi-particle tracking codes

The existing analytical formulas for modelling the IBS effect are based on Gaussian beam distributions. In the case of non-Gaussian beam distributions no theoretical models exist. The stationary solution of the Fokker-Planck equation is a particle distribution that is Gaussian in the phase space. However, taking into account the effects of IBS, radiation damping and quantum excitation [46], there is no evidence that the distribution remains Gaussian. Therefore, it is important to develop analytical formulas and simulation tools that calculate the interplay between these effects for any distribution. To this end, two multi-particle Monte Carlo codes capable of such calculations have been developed; the Software for IBS and Radiation Effects (SIRE) [47], and the IBStrack [48] implemented also in the collective effects simulation tool CMAD [49, 50]. Both algorithms are inspired by MOCAC (MONte CARlo Code), a Monte-Carlo code developed by Zenkevich et al [51, 52], which calculates the IBS effect for arbitrary distributions. SIRE and IBStrack include also Radiation Damping (RD) and Quantum Excitation (QE). SIRE uses only the optics functions around the ring, calculating only the pure IBS effect without taking into account coupling or non-linear effects. However, IBStrack uses the element-by-element composed one turn map, taking into account the phase advance between the elements and so, non-linear effects and coupling can also be included in the calculations.

The performance of hadron machines is limited by the IBS effect causing emittance blow up. For lepton machines such as future linear collider Damping Rings, new generation light sources and B-factories, the IBS effect can also be predominant. It is thus important to study the IBS theories in the presence of synchrotron radiation and quantum excitation and benchmark the existing theoretical models and tracking codes with experimental data. In this way, the codes limitations can be identified so that to apply the necessary improvements in order to get better predictions for the operation of a machine..

For the Relativistic Heavy Ion Collider (RHIC), the IBS growth rates were calculated and benchmarked with experimental data using the distribution function evolution (based on the Fokker-Planck equations), extending the usual approach of employing a conventional Gaussian-like distribution [53]. Furthermore, the intrabeam scattering growth rates were calculated for a bi-gaussian distribution, which was interesting for studying the possibility of using electron cooling in RHIC [54]. Later, a model that is suitable for IBS calculations for arbitrary distribution functions and its comparison to experimental data was presented in [55]. The IBS effect was also studied for high-brightness electron linac beams which appear to be non-Gaussian, especially in the longitudinal plane [56].

The IBS theoretical models have been studied in detail and benchmarked with experimental data [17,18] for hadron beams over the years. A benchmarking of the IBS theoretical models with Monte-Carlo codes is presented in [57] for lepton rings and in [58] for the LHC. A comparison of the LHC data with simulations performed with SIRE is discussed in [59].

## SIRE

The SIRE [47,60] code uses the classical Rutherford cross section which is closer to the Piwinski formalism, for the IBS calculations. It needs as an input the Twiss functions at different locations of the lattice in order to determine the trajectories of the particles in phase space. This is done in terms of the two Courant-Snyder and longitudinal invariants, and the 3 phases (betatron and synchrotron), instead of using the 6 coordinates for position and momentum. The 3 invariants are conserved between points around the lattice and can only be changed by the effects of IBS, SR and QE, while the phases are chosen randomly at each given point of the lattice. The time steps for which the IBS and radiation effects are called should be specified such that they are larger than the revolution time and smaller than the damping/growth times. Dividing the total time by the time steps shows how frequently the IBS, SR and QE routines are called. Currently, the output file giving the evolution of the emittance in all planes presents the values computed for the specified time steps.

The algorithm SIRE uses to calculate IBS is similar to the one implemented in MOCAC, where the beam is represented by a large number of macro-particles occupying points in the 6-dimensional phase space. The default distribution defined in SIRE by using a random number generator, is the Gaussian and is given in action angle variables. So, in order to get a Gaussian distribution in terms of beam size, the histogram of the macroparticles action angle variables should form an exponential (based on 2.25), as given in Fig. 3.1. In order to apply a different distribution, someone should either make SIRE generate the proper random deviates or provide as an input file the action angle variables of all macroparticles for the desired distribution. After specifying the total beam population and the number of macro-particles, the initial distribution

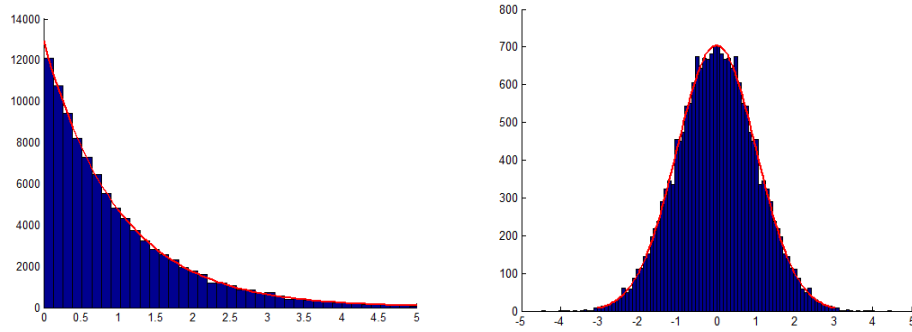


Figure 3.1: The default distribution defined in SIRE by using a random number generator is the Gaussian and is given in action angle variables. In this case, the histogram of the macroparticles action angle variables is described by the exponential function (left), the corresponding distribution in terms of beam size is a Gaussian (right).

of the macro-particles can be tracked. The particle distribution in all planes can be saved as often as requested during the simulation time.

The steps followed for the IBS effect simulation can be summarized as:

- For each lattice point defined in the Twiss file, the 3 phases of each macro-particle are randomly chosen and position and momentum of the macro-particles are calculated.
- The beam is geometrically divided into a number of cells that is specified for each plane. The macro-particles are assigned to each cell according to their geometrical position (Fig. 3.2).
- Based on the classical Rutherford cross section, intra-beam collisions between pairs of macro-particles are calculated in each cell. The momentum of particles is changed because of scattering. According to the available computational time, the number of macro-particles and cells, i.e. the number of collisions each macro-particle experiences, is chosen. The scattering angles for each collision are determined [61].
- The beam distribution is then updated based on the new invariants of the macro-particles.
- The simulation proceeds to the next lattice point and continues until the end time is reached.

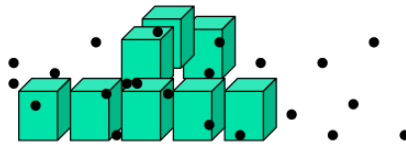


Figure 3.2: The beam is geometrically divided into a number of cells that is specified for each plane. The macro-particles (black dots) are assigned to the constructed cells (green cubes) according to their geometrical position.

Depending on the elapsed time, the synchrotron radiation damping (RD) acts on the invariants of the macro-particles as an exponential decrement. The routine introduced for this reason is called after the calculation of the IBS effect for each iteration. Using small iteration time steps  $dt$  (which are much smaller than the damping times and for which the emittances change

adiabatically), the evolution of the transverse emittance and energy spread due to the effects of IBS and SR can be obtained by solving the coupled differential equations:

$$\begin{aligned}\frac{d\varepsilon_{x,y}}{dt} &= \frac{-2(\varepsilon_{x,y} - \varepsilon_{x,y0})}{\tau_{x,y}} + \frac{2\varepsilon_{x,y}}{T_{x,y}}, \\ \frac{d\sigma_p}{dt} &= \frac{-(\sigma_p - \sigma_{p0})}{\tau_p} + \frac{\sigma_p}{T_p},\end{aligned}\tag{3.10}$$

with  $\varepsilon_{x,y0}$  and  $\sigma_{p0}$  being the zero current (without the effect of IBS) equilibrium transverse emittances and energy spread, respectively. The  $\tau_{x,y}$ ,  $\tau_p$  are the synchrotron radiation damping times and the  $T_{x,y}$ ,  $T_p$  the IBS growth times. The QE is then implemented, by adding to the 6 coordinates of each macro-particle a random Gaussian contribution.

A lattice compression technique named ‘‘lattice recurrences’’, has been implemented to speed up the calculations [47]. Since the increase of the invariants due to IBS is linear to the first order in the traveling time along an element, elements of the full lattice with optics functions differing less than a specified precision value are considered equal. For such a group of elements, the IBS effect is evaluated only for one of these elements, resulting in a smaller computational time.

### Convergence studies

For a specified set of input beam parameters, various scans should be performed for different combinations of number of macro-particles and cells in order to find the optimal values which provide a fast tracking and at the same time, guarantee that the scattering process leads to accurate results. In these terms, in order to avoid having a very small number of macro-particles per cell, the total number of cells is calculated based on the optimal minimum number of macro-particles per cell. For  $n_x$ ,  $n_y$ ,  $n_z$  being the number of cells in the horizontal, vertical and longitudinal plane, respectively, it is assumed that in the transverse plane there is a correlation between the number of cells ratio and the beam sizes ratio, meaning that  $n_x/n_y = \sigma_x/\sigma_y$ . Therefore, for  $n_{mp}$  being the total number of macro-particles, the number of macro-particles per cell is:

$$n_{mp}/cell = \frac{n_{mp}}{n_x n_y n_z} = \frac{n_{mp}}{n_x^2 \left(\frac{\sigma_y}{\sigma_x}\right) n_z}.\tag{3.11}$$

A scanning of the total number of cells is performed for an example set of beam parameters to be used as an input for tracking. Based on Eq. (3.11), by keeping the total number of macro-particles constant, the different combinations of cell numbers determines the number of macro-particles per cell. Figure 3.3 (left) shows the dependence of the emittance variation (ratio of final versus initial value) in the horizontal (blue) and longitudinal (green) plane on the number of macro-particles per cell, for a specified time duration. The value of the number of macro-particles per cell after which the variation of the emittances in both planes remains constant is chosen as the optimal minimum value. After specifying this value, a scanning is performed for a fixed number of macro-particles, in order to choose the number of cells to be used, firstly in the longitudinal plane.

Then, the number of cells in the horizontal plane can be calculated using Eq. (3.11), when knowing the ratio of the beam sizes in the transverse plane <sup>2</sup>. In Fig. 3.3, the dependence of

<sup>2</sup>Here it is assumed that the ratio of the transverse beam sizes is initially  $\sigma_x/\sigma_y = 1$ .

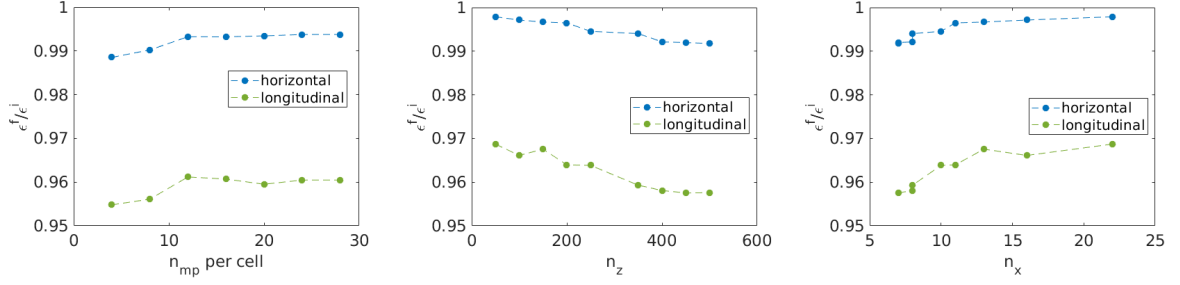


Figure 3.3: The dependence of the horizontal (blue) and longitudinal (green) emittance variation on the number of macro-particles per cell (left), on the number of cells in the longitudinal plane (center) and in the horizontal plane (right), for a specific time period.

the emittances variation is plotted versus the number of cells in the longitudinal (center) and horizontal (right) plane, for a specific time duration. It can be noticed that the variation of the emittances remains constant after a certain number of cells in the longitudinal and horizontal plane that is, for the example set of beam parameters, 350 and 13 cells, respectively. Finally, the number of cells in the vertical plane can be calculated by  $n_y = n_x/(\sigma_x/\sigma_y)$ .

# Reduction of the TME cell emittance using longitudinally variable bends

---

One of the main challenges of linear collider DRs and light sources is the generation of ultra-low emittance in all planes in order to achieve high brightness beams. The main design task is to build a compact ring, attaining a sufficiently low emittance and an adequately large dynamic aperture (DA). The DR lattice design is driven by the emittance requirements which for ultra-low values give rise to collective effects, with intra-beam scattering (IBS) being the dominant one. Aiming to mitigate the IBS effect for a compact ring, the design of the lattice should be revised. The TME cells can provide very small emittances, as well as high compactness. The emittance of a TME cell can be further reduced if instead of uniform dipoles, longitudinally variable bends are used. In this chapter, the studies for minimizing the emittance of a TME cell using variable bends, are presented. The optimal magnetic field evolution of these bends, in order to have a low equilibrium betatron emittance, is found for each dipole profile studied. The resulted emittance is compared to the one of a uniform dipole having the same bending angle and length.

## 4.1 Analytical solutions for minimizing the emittance of a TME cell

The optimal magnetic structure to achieve the absolute theoretical minimum emittance (TME) is the TME cell [62, 63]. Due to their compactness and the very small emittance these cells reach, they are preferred for some ring designs. The performance of these cells was previously studied analytically for the case of uniform dipoles [33]. In what follows, a further minimization of the TME cell emittance when using longitudinally variable bends instead of uniform dipoles is described in detail. In order to have a global understanding of all cell properties, analytical solutions for a TME cell with a variable bend are developed.

The equilibrium horizontal emittance in a storage ring is given by:

$$\varepsilon_x = \frac{C_q \gamma^2}{J_x} \frac{\langle \frac{\mathcal{H}}{|\rho|^3} \rangle}{\langle \frac{1}{\rho^2} \rangle} = \frac{C_q \gamma^2}{J_x} \frac{\frac{1}{C} \int_0^C \frac{\mathcal{H}}{|\rho|^3} ds}{\frac{1}{C} \int_0^C \frac{1}{\rho^2} ds}, \quad (4.1)$$

where  $C$  is the circumference of the ring,  $\gamma$  is the Lorentz factor,  $J_x$  is the damping partition number and  $C_q = 3.84 \times 10^{-13}$  m (for electrons). The lattice function  $\mathcal{H}$  known as the dispersion

invariant, depends on the optics parameters, the dispersion function and its derivative:

$$\mathcal{H}(s) = \gamma(s)\eta(s)^2 + 2\alpha(s)\eta(s)\eta'(s) + \beta(s)\eta'(s)^2 . \quad (4.2)$$

In the case of uniform dipoles, having a constant bending radius  $\rho$ , the minimum emittance value is obtained through the minimization of the  $\langle \mathcal{H} \rangle$ . However, in the case of longitudinally variable bends, for a varying  $\rho$  along the length of the magnet, the aim is to minimize  $\langle \mathcal{H}/\rho^3 \rangle / \langle 1/\rho^2 \rangle$ .

### The TME cell

A schematic layout of the TME cell is displayed in Fig. 4.1. It consists of one dipole D of length  $L$  and of two quadrupole families Q1, Q2 with focal lengths  $f_1$  and  $f_2$  respectively. The focal lengths of the quadrupoles are denoted by  $f_1[m] = 1/(k_1 l_{q_1})$  and  $f_2[m] = 1/(k_2 l_{q_2})$ , where  $k_1, k_2$  are the quadrupole strengths and  $l_{q_1}, l_{q_2}$  their lengths. The drifts between the elements are denoted by  $s_1, s_2$  and  $s_3$ .

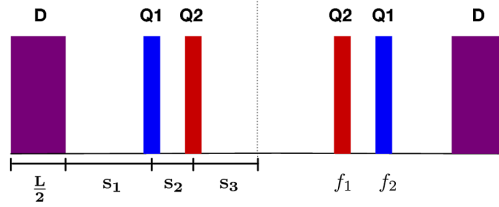


Figure 4.1: Schematic layout of a TME cell

For simplicity, the center of consecutive dipoles is considered as the entrance and exit of the TME cell, the index “ $cd$ ” (center of dipole) represents the initial point. Then, the optics parameters, the dispersion function and its derivative from the center to the edge can be written as:

$$\begin{aligned} \beta(s) &= \beta_{cd} - 2\alpha_{cd}s + \gamma_{cd}s^2, \quad \alpha(s) = \alpha_{cd} - \gamma_{cd}s, \quad \gamma(s) = \gamma_{cd}, \\ \eta(s) &= \eta_{cd} + \eta'_{cd}s + \tilde{\theta}(s), \quad \eta'(s) = \eta'_{cd} + \theta(s) . \end{aligned} \quad (4.3)$$

The expressions in Eq. (4.3) are used to calculate the dispersion invariant  $\mathcal{H}(s)$  (Eq. (4.2)). It should be mentioned that the focusing of the dipole is negligible for dipoles having a small bending angle.

The theoretical minimum emittance can be achieved if the symmetry condition, for which both beta ( $\beta_x$ ) and dispersion ( $\eta_x$ ) functions have a minimum at the center of the bending magnets ( $\alpha_{cd} = \eta'_{cd} = 0$ ), is satisfied (Fig. 4.2) [62, 63]. For isomagnetic TME cells the dispersion and beta functions at the center of the dipole are respectively equal to  $\eta_{cd} = \frac{\theta L}{24}$  and  $\beta_{cd} = \frac{L}{2\sqrt{15}}$ , where  $\theta$  is the bending angle and  $L$  the length of the dipole. These functions are different for a non-uniform dipole since its bending angle and bending radius vary along the electron beam path in the magnet. The bending angle and its integral are given by:

$$\theta = \int_0^s \frac{1}{\rho(s)} ds, \quad \tilde{\theta} = \int_0^s \left( \int_0^s \frac{1}{\rho(s)} ds \right) ds . \quad (4.4)$$

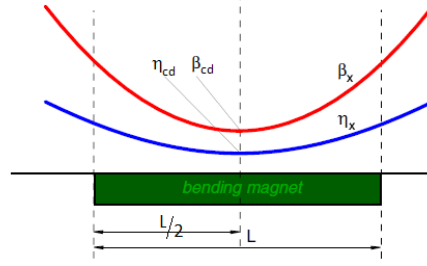


Figure 4.2: Symmetry condition for the TME.

The beta and dispersion functions at the dipole center ( $\beta_{cd}$  and  $\eta_{cd}$ ) impose two independent optics constraints, therefore, at least two quadrupole families are needed for the constraints to be met. Using the thin-lens approximation and for given  $\beta_{cd}$  and  $\eta_{cd}$  at the center of the dipole, the analytical expressions for the quadrupole focal lengths can be derived:

$$f_1 = \frac{s_2 g_1}{g_1 - \eta_{ss} + s_2 \theta} \quad (4.5)$$

$$f_2 = \frac{s_2 \eta_{ss}}{g_1 - \eta_{ss}} \quad (4.6)$$

where:

$$g_1 = \eta_{cd} + s_1 \theta + \tilde{\theta} \quad (4.7)$$

The dispersion  $\eta_{ss}$  at the center of the cell, between two mirror symmetric quadrupoles, depends on the drift lengths, the optics functions at the dipole center and the bending characteristics and it is given by:

$$\eta_{ss} = \frac{-2g_1 s_3}{s_2} \frac{1}{1 \pm \sqrt{1 + \frac{4g_1 s_3}{s_2^2} \frac{\beta_{cd}^2 \theta - (L/2 + s_1) g_2}{\beta_{cd}^2 \theta^2 + g_2^2}}} \quad (4.8)$$

where:

$$g_2 = \eta_{cd} - \frac{L}{2} \theta + \tilde{\theta} \quad (4.9)$$

In the limit of  $s_2 \rightarrow 0$ , meaning that Q1 and Q2 are merged into one quadrupole, both  $f_1$  and  $f_2$  vanish, giving infinite focusing strengths. When  $s_3 \rightarrow 0$ , the two quadrupoles that belong to the Q2 family of the TME cell are merged into one and  $f_2$  vanishes. Drift space lengths that result in very low focal length values and, therefore, in extremely strong quadrupoles must be avoided. In this respect, two consecutive quadrupoles cannot be merged into one. The fact that in the limit of  $s_1 \rightarrow 0$  both  $f_1$  and  $f_2$  have fixed non-zero values, implies that it is possible to place the quadrupole with focal length  $f_1$  exactly next to the dipole, with no drift space between them. Based on Eq. (4.5) and Eq. (4.6), the full expressions of the quadrupole focal lengths,  $f_1$  and  $f_2$ , at the limits where the drifts  $s_1$ ,  $s_2$  and  $s_3$  are zeroed are:

- $\lim_{s_1 \rightarrow 0} f_1 = \frac{s_2(\eta_{cd} + \tilde{\theta})}{\eta_{cd} + \tilde{\theta} - \eta_{ss1} + s_2 \theta}$  and  $\lim_{s_1 \rightarrow 0} f_2 = \frac{s_2 \eta_{ss1}}{\eta_{cd} + \tilde{\theta} - \eta_{ss1}}$

#### 4.1. ANALYTICAL SOLUTIONS FOR MINIMIZING THE EMITTANCE OF A TME CELL 41

- $\lim_{s_2 \rightarrow 0} f_1 = 0$  and  $\lim_{s_2 \rightarrow 0} f_2 = 0$
- $\lim_{s_3 \rightarrow 0} f_1 = \frac{s_2 g_1}{g_1 + s_2 \theta}$  and  $\lim_{s_3 \rightarrow 0} f_2 = 0$

where:

$$\eta_{ss1} = \frac{-2(\eta_{cd} + \tilde{\theta})s_3}{\frac{s_2}{1 \pm \sqrt{1 + \frac{4(\eta_{cd} + \tilde{\theta})s_3}{s_2^2} \frac{\beta_{cd}^2 \theta - g_2 L/2}{\beta_{cd}^2 \theta^2 + g_2^2}}}}$$

and for  $g_1$  and  $g_2$  given by Eq. (4.7) and Eq. (4.9), respectively

### Analytical parametrization of a non-uniform dipole profile

Longitudinally variable dipoles, whose magnetic field varies along their length, can provide lower horizontal emittances than a uniform dipole of the same bending angle [64, 65]. In the case of a TME cell for which the symmetry condition is applied, the evolution of  $\mathcal{H}(s)$  along a uniform dipole is shown in Fig. 4.3. This evolution guides the bending radius choice for achieving an emittance reduction by using a variable bend. In fact, the variable bend should be designed such that the minimum bending radius is at the dipole's center and then it should decrease towards the edge of the dipole [66–72].

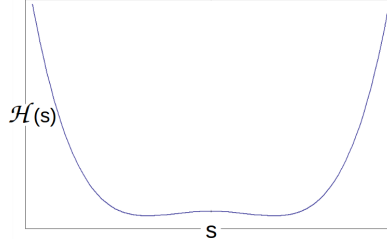


Figure 4.3: The evolution of the dispersion invariant along the uniform dipole.

For the present work, two different bending radii functions are used to describe the field evolution. It is assumed that these functions can be either constants or linearly dependent on the distance  $s$ . For simplicity, half of the dipole (from 0 to  $L/2$ ) is considered since the rest is symmetric. In this respect, the first part of the half dipole starts at the dipole center ( $s = 0$ ) having a length  $L_1$  and the second one with a length  $L_2$  follows until the end of the dipole, with bending radii functions  $\rho_1(s)$  and  $\rho_2(s)$  respectively.

The maximum magnetic field is at the center of the dipole, where the bending radius is minimum. The minimum magnetic field and maximum bending radius is at the edges of the magnet. The field evolution along the magnet can be well described by using only two parameters; the lengths and the bending radii ratio [69, 70, 72], that are defined as:

$$\lambda = \frac{L_1}{L_2} \quad \text{and} \quad \tilde{\rho} = \frac{\rho_1}{\rho_2} . \quad (4.10)$$

The lower  $\lambda$  is, the shorter is the high field region compared to the low field one. The lower  $\tilde{\rho}$  is, the higher is the field at the dipole center compared to the one at the edges. Generally,  $\tilde{\rho} < 1$  because  $\rho_2$  needs to be larger than  $\rho_1$  and  $\lambda > 0$ .

Splitting the half dipole in two parts with different bending radii requires the study of the dispersion invariants for each part separately. In this respect, the dispersion invariant given in Eq. (4.2) should be calculated for both parts; that is  $\mathcal{H}_1(s)$  and  $\mathcal{H}_2(s)$  with:

$$\mathcal{H}_{1,2}(s) = \gamma_{1,2}\eta_{1,2}^2 + 2\alpha_{1,2}\eta_{1,2}\eta'_{1,2} + \beta_{1,2}\eta'_{1,2}{}^2 . \quad (4.11)$$

After implementing the symmetry condition in Eq. (4.3), the optics functions for the first and the second part of the half dipole are given by Eq. (4.12) and Eq. (4.13) respectively, for  $\beta_{L_1}$ ,  $\alpha_{L_1}$ ,  $\gamma_{L_1}$ ,  $\eta_{L_1}$  and  $\eta'_{L_1}$  corresponding to the optics functions at the point where  $s = L_1$ .

$$\beta_1 = \beta_{cd} + \gamma_{cd}s^2, \quad \alpha_1 = -\gamma_{cd}s, \quad \gamma_1 = \gamma_{cd}, \quad \eta_1 = \eta_{cd} + \tilde{\theta}_1, \quad \eta'_1 = \theta_1 \quad (\alpha_{cd} = 0, \eta'_{cd} = 0) \quad (4.12)$$

$$\begin{aligned} \beta_2 &= \beta_{L_1} - 2(s - L_1)\alpha_{L_1} + (s - L_1)^2\gamma_{L_1}, \quad \alpha_2 = \alpha_{L_1} - (s - L_1)\gamma_{L_1}, \quad \gamma_2 = \gamma_{L_1}, \\ \eta_2 &= \eta_{L_1} + \tilde{\theta}_2 + (s - L_1)\eta'_{L_1}, \quad \eta'_2 = \theta_2 + \eta'_{L_1} , \end{aligned} \quad (4.13)$$

where the bending angles and their integrals, using Eq. (4.4), are expressed as:

$$\theta_1 = \int_0^s \frac{1}{\rho_1(s)} ds, \quad \theta_2 = \int_{L_1}^s \frac{1}{\rho_2(s)} ds, \quad \tilde{\theta}_1 = \int_0^s \theta_1 ds, \quad \tilde{\theta}_2 = \int_{L_1}^s \theta_2 ds , \quad (4.14)$$

The bending angle of the half dipole is then given by:

$$\theta = \theta_{1(s=L_1)} + \theta_{2(s=L_1+L_2)} = \int_0^{L_1} \frac{1}{\rho_1(s)} ds + \int_{L_1}^{L_1+L_2} \frac{1}{\rho_2(s)} ds . \quad (4.15)$$

Inserting the partial dispersion invariants into Eq. (4.1), the emittance is found to be:

$$\varepsilon_x = G \left( \frac{1}{L_1} \int_0^{L_1} \frac{\mathcal{H}_1}{|\rho_1(s)|^3} ds + \frac{1}{L_2} \int_{L_1}^{L_1+L_2} \frac{\mathcal{H}_2}{|\rho_2(s)|^3} ds \right) , \quad (4.16)$$

where:

$$G = \frac{C_q \gamma^2}{J_x} \left( \frac{1}{L_1} \int_0^{L_1} \frac{1}{\rho_1(s)^2} ds + \frac{1}{L_2} \int_{L_1}^{L_1+L_2} \frac{1}{\rho_2(s)^2} ds \right)^{-1}$$

The final form of Eq. (4.16) can be expressed as:

$$\varepsilon_x = G \frac{I_7 + I_8 \lambda + (I_1 + I_2 \lambda) \beta_{cd}^2 + \eta_{cd} (I_5 + I_6 \lambda + (I_3 + I_4 \lambda) \eta_{cd})}{L_1 \beta_{cd}} , \quad (4.17)$$

with the integrals  $I_1 - I_8$  given in Appendix B.

#### 4.1. ANALYTICAL SOLUTIONS FOR MINIMIZING THE EMITTANCE OF A TME CELL 43

In order to find the absolute minimum emittance, the partial derivatives of the emittance with respect to the beta and dispersion functions should be zeroed. As a result, the  $\beta_{TME}$  and  $\eta_{TME}$  values that achieve the TME at the center of the dipole are found to be:

$$\beta_{TME} = \frac{\sqrt{-(I_5 + I_6\lambda)^2 + 4(I_7 + I_8\lambda)(I_3 + I_4\lambda)}}{2\sqrt{(I_1 + I_2\lambda)(I_3 + I_4\lambda)}} \quad \text{and} \quad \eta_{TME} = -\frac{I_5 + I_6\lambda}{2(I_3 + I_4\lambda)}. \quad (4.18)$$

By inserting Eq. (4.18) into Eq. (4.17) the expression for the TME is given by:

$$\varepsilon_{TME} = G \frac{\sqrt{I_1 + I_2\lambda} \sqrt{-(I_5 + I_6\lambda)^2 + 4(I_7 + I_8\lambda)(I_3 + I_4\lambda)}}{L_1 \sqrt{I_3 + I_4\lambda}}. \quad (4.19)$$

The emittance detuning factor  $\varepsilon_r$  that describes the deviation of the emittance  $\varepsilon_x$  from its theoretical minimum  $\varepsilon_{TME}$  can be calculated using Eq. (4.20).

$$\varepsilon_r = \frac{\varepsilon_x}{\varepsilon_{TME}} = \frac{\sqrt{I_3 + I_4\lambda} (I_7 + I_8\lambda + (I_1 + I_2\lambda)\beta_{cd}^2 + (I_3 + I_4\lambda)\eta_{cd}^2 - (I_5 + I_6\lambda)\eta_{cd})}{\beta_{cd}\sqrt{I_1 + I_2\lambda}\sqrt{-(I_5 + I_6\lambda)^2 + 4(I_7 + I_8\lambda)(I_3 + I_4\lambda)}} \quad (4.20)$$

Solving Eq. (4.20) with respect to  $\beta_{cd}$ , the solutions, that are functions of  $\varepsilon_r$  and  $\eta_{cd}$ , are:

$$\beta_{cd1,2} = \frac{\varepsilon_r \sqrt{4(I_7 + I_8\lambda) - \frac{(I_5 + I_6\lambda)^2}{I_3 + I_4\lambda}}}{2\sqrt{I_1 + I_2\lambda}} \pm \frac{\sqrt{4((I_7 + I_8\lambda)(\varepsilon_r^2 - 1) + (I_3 + I_4\lambda)\eta_{cd}^2 - (I_5 + I_6\lambda)\eta_{cd}) - \frac{(I_5 + I_6\lambda)^2}{I_3 + I_4\lambda}\varepsilon_r^2}}{2\sqrt{I_1 + I_2\lambda}}, \quad (4.21)$$

with the integrals  $I_1 - I_8$  given in Appendix B. Applying the requirement of  $\beta_{cd}$  to be a real-positive number, the quadratic dependence of the argument in the square root on the dispersion at the center of the dipole must have an upper and a lower limit, i.e.  $\eta_{min} < \eta_{cd} < \eta_{max}$ , given by:

$$\eta_{cdmin,max} = -\frac{(I_5 + I_6\lambda) \pm \sqrt{((I_5 + I_6\lambda)^2 - 4(I_3 + I_4\lambda)(I_7 + I_8\lambda))(1 - \varepsilon_r^2)}}{2(I_3 + I_4\lambda)}. \quad (4.22)$$

The  $\beta_{cd}$  has two solutions for a fixed  $\eta_{cd}$ . The solutions of  $\beta_{cd}$  and  $\eta_{cd}$ , that depend on the detuning factor  $\varepsilon_r$ , determine the limits of  $\varepsilon_x$ .

The horizontal and vertical phase advances of the cell can be found using the trace of the cell transfer matrix. The horizontal phase advance, using Eq. (4.9), is given by:

$$\cos \mu_x = \frac{g_2^2 - \beta_{cd}^2 \theta^2}{g_2^2 + \beta_{cd}^2 \theta^2}. \quad (4.23)$$

For a uniform dipole, the horizontal phase advance in order to reach the absolute minimum emittance is independent of any cell or dipole characteristics and has the unique value  $\mu_x = 284.5^\circ$  [31]. However, in the case of the non-uniform dipoles, the horizontal phase advance for reaching the TME condition is based on  $\theta$  and  $\tilde{\theta}$  and thus, it depends on  $\tilde{\rho}$  and  $\lambda$ .

The vertical phase advance can be expressed as:

$$\begin{aligned} \cos \mu_y = & 1 + (L + 2(s_{13} + s_{12}))\left(\frac{1}{f_1} + \frac{1}{f_2}\right) + \frac{(L + 2s_1)s_{23}}{f_1^2} + \frac{(L + 2(s_1 + s_{12}))s_3}{f_2^2} + \frac{(L + 2s_1)s_2^2 s_3}{f_1^2 f_2^2} \\ & + 2\frac{(L + s_1 + s_{12})s_{23} + s_{12}s_3}{f_1 f_2} + \frac{(L + 2s_1)(s_2^2 + 2s_2 s_3)}{f_1^2 f_2} + 2\frac{(L + 2s_1 + s_{12})s_2 s_3}{f_1 f_2^2}, \end{aligned} \quad (4.24)$$

where  $s_{12} = s_1 + s_2$ ,  $s_{13} = s_1 + s_3$  and  $s_{23} = s_2 + s_3$ . If the cell is tuned to the absolute minimum emittance conditions, for  $s_1 \rightarrow 0$  or  $s_2 \rightarrow 0$  or  $s_3 \rightarrow 0$  and based on the results presented earlier, the  $\cos \mu_y$  goes to infinity and so, the vertical motion is unstable. Unlike the horizontal phase advance, the vertical one depends both on the optics functions at the dipole center and on the cell geometry.

## 4.2 Dipole profiles

Based on studies of preceding works for the longitudinally variable bends [64–69], two dipole profiles are presented where the bending radius forms a step and a trapezium shape. The step profile shown in Fig. 4.4 (left) consists of two different constant field segments, having the minimum bending radius at the dipole center. The evolution of  $\rho$  for the step profile is given by:

$$\rho(s) = \begin{cases} \rho_1, & 0 < s < L_1 \\ \rho_2, & L_1 < s < L_1 + L_2 = L/2 \end{cases}$$

The trapezium profile is shown in Figure 4.4 (right), where again the strongest constant field segment is localized at the center of the dipole. The evolution of the bending radius from the dipole center until its edge is expressed as:

$$\rho(s) = \begin{cases} \rho_1, & 0 < s < L_1 \\ \rho_1 + (L_1 - s)(\rho_1 - \rho_2)/L_2, & L_1 < s < L_1 + L_2 = L/2 \end{cases}$$

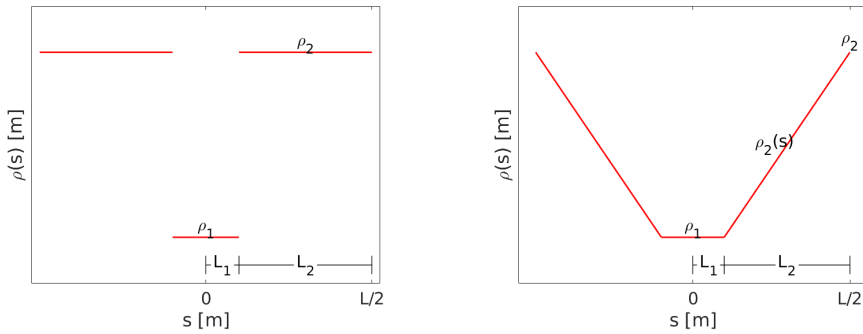


Figure 4.4: The evolution of the bending radius along the step (left) and the trapezium (right) dipole profile.

The theoretical minimum emittance, as calculated using Eq. (4.19) for each dipole profile, depends on  $\tilde{\rho}$ ,  $\lambda$  and  $\theta$ . The emittance reduction factor that describes the reduction of the minimum emittance for a non-uniform dipole with respect to a uniform one with the same

bending angle, is defined as:

$$F_{TME} = \frac{\varepsilon_{TME_{uni}}}{\varepsilon_{TME_{var}}} , \quad (4.25)$$

where  $\varepsilon_{TME_{uni}}$  and  $\varepsilon_{TME_{var}}$  are the TMEs for a uniform dipole and a variable bend respectively. The  $F_{TME}$  depends only on  $\tilde{\rho}$  and  $\lambda$ . For both dipole cases, the full expression of the  $F_{TME}$  is given in Appendix C.

### The relation between the reduction and the detuning factor

In practice, the TME cells are detuned to reach larger emittances so that the cell characteristics are more relaxed. Moving away from the TME, the resulted emittances are  $\varepsilon_{var}$  and  $\varepsilon_{uni}$  for the non-uniform and for the iso-magnetic dipoles, respectively. In order to compare the emittances of a uniform and of a non-uniform bending magnet, their ratio (using Eqs. (4.20) and (4.25)) is defined as:

$$\frac{\varepsilon_{var}}{\varepsilon_{uni}} = \frac{\varepsilon_{r_{var}} \varepsilon_{TME_{var}}}{\varepsilon_{r_{uni}} \varepsilon_{TME_{uni}}} = \frac{\varepsilon_{r_{var}}}{\varepsilon_{r_{uni}}} \frac{1}{F_{TME}} , \quad (4.26)$$

where  $\varepsilon_{r_{var}}$  and  $\varepsilon_{r_{uni}}$  are the detuning factors for the non-uniform and for the uniform dipole respectively. In order to get an emittance reduction, it should always be  $\frac{\varepsilon_{var}}{\varepsilon_{uni}} < 1$ . Thus, using Eq. (4.26), the restriction of:

$$\frac{\varepsilon_{r_{var}}}{\varepsilon_{r_{uni}}} < F_{TME} \quad (4.27)$$

is established. The smaller is the ratio of the detuning factors compared to the  $F_{TME}$  (that is fixed in accordance to the chosen dipole characteristics), the lower is the final emittance the variable bend gives. Practically this means that even if the detuning of a TME cell with a variable bend is larger than in the case of using a uniform dipole, emittance reductions are possible if Eq. (4.27) is satisfied.

### Parameterization of the emittance reduction factor $F_{TME}$ with $\rho$ and $\lambda$

The characteristics of a realistic dipole profile are driven by the constraint of how sharply and quickly the transition from the high to the low field can be established. Regarding the fact that the fringe field of the first dipole part should not significantly affect the field of the second one and that a sharp field drop off is technologically questionable, the minimum difference between the highest and the lowest field and the corresponding lengths difference is assumed to be 4%. So, the range of the following plots is regulated by the restriction of  $\lambda, \tilde{\rho} > 0.04$ . Based on the optimal variable bend characteristics, the design of a magnet that can give the final specifications of the dipole to be fabricated is under study [73, 74].

In Figure 4.5, the reduction factor  $F_{TME}$  is parametrized with  $\tilde{\rho}$  and  $\lambda$ , for the step (left) and the trapezium (right) profile. The areas where  $F_{TME}$  is high are blue-colored, while red-colored are the areas where the reduction is smaller. The black contour lines show different values of the horizontal phase advance. For a uniform dipole, there is a unique horizontal phase advance independent of any cell or dipole characteristics in order to reach the absolute minimum emittance case, which is given by  $\mu_x = 284.5^\circ$  [31]. However, in the case of the non-uniform dipoles, the horizontal phase advance for reaching the TME condition depends on  $\tilde{\rho}$  and  $\lambda$ . The highest reductions correspond to high phase advances  $\mu_x > 310^\circ$ . Still, remarkable emittance

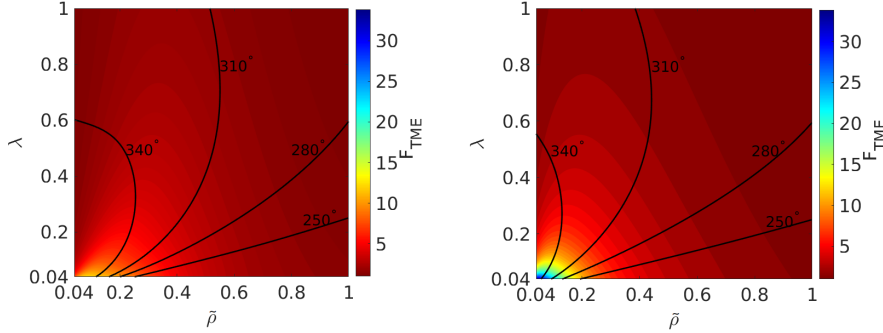


Figure 4.5: The parametrization of the reduction factor  $F_{TME}$  with the bending radii ratio  $\tilde{\rho}$  and the lengths ratio  $\lambda$  for the step (left) and the trapezium (right) profile, for the TME case. The black contour lines correspond to different values of horizontal phase advances.

reductions are reached even for lower phase advances which correspond to smaller chromaticities, that is one of the main goals for the optimization of low emittance cells.

For both profiles, in the limits where  $\tilde{\rho}, \lambda \rightarrow 1$  (i.e.  $\rho_2 = \rho_1$  and  $\lambda_2 = \lambda_1$ ) there is no emittance reduction. Actually this was expected because  $\tilde{\rho} \rightarrow 1$  means that the bending radius is constant and so, the variable bend becomes practically a uniform dipole. In the limits where  $\lambda \rightarrow 0$  and  $\tilde{\rho} \rightarrow 0$  (i.e.  $L_2 \gg L_1$  and  $\rho_2 \gg \rho_1$ ) the reductions obtained are practically infinite. The highest possible reductions are found to be around 13 and 34 for the step and the trapezium profile, respectively, for  $\lambda, \tilde{\rho} > 0.04$ . These reductions are localized where both  $\lambda$  and  $\tilde{\rho}$  are low, demanding a sharp transition from the high to the low field region. The issue of concern for the design of a variable bend is how small can  $\tilde{\rho}$  be in order to get a realistic difference between the maximum and the minimum magnetic field along a specific dipole length that has a fixed bending angle. The magnetic design of a longitudinally variable bend will determine the final limitations of the dipole's characteristics.

### The resulted emittance reduction factor $F_{TME}$ when fixing the dipole characteristics

In order to facilitate the comparison between the step and the trapezium profile, the number of dipoles  $N_d$ , their length  $L$  and the minimum bending radius  $\rho_1$  values are kept the same. As a numerical example, the minimum  $\rho_1$  value is set to 4.1 m, i.e.  $B = 2.3$  T at an energy of 2.86 GeV for the CLIC DRs. Also, examples for dipole lengths and angles different than the ones of the CLIC DR design are presented. Using Eq. (4.15), the bending angles for the step and the trapezium profile respectively, are found to be:

$$\theta_{step} = \frac{L(\lambda + \tilde{\rho})}{\rho_1(1 + \lambda)} \quad \text{and} \quad \theta_{trapezium} = \frac{L(\lambda(-1 + \tilde{\rho}) + \tilde{\rho} \ln \tilde{\rho})}{\rho_1(-1 + \tilde{\rho})(1 + \lambda)}. \quad (4.28)$$

Solving Eq. (4.28) with respect to bending radii ratio  $\tilde{\rho}$ , for a fixed minimum bending radius value  $\rho_1$ , it is found that  $\tilde{\rho}$  depends on the bending angle, the dipole length and the lengths ratio (i.e.  $\theta, L$  and  $\lambda$ ). Thereby, the reduction factor becomes a function of  $\theta$  (or the total number of dipoles  $N_d$ ),  $L$  and  $\lambda$ . Even if by increasing length or the number of dipoles the reduction

factors achieved get higher, a compromise between how long and how many are the dipoles used is required. In addition, as will be mentioned in the next section, the fabrication of a variable bend sets a lower limit on  $\lambda$  [74] and so, an upper limit on the reduction factor values that can be achieved.

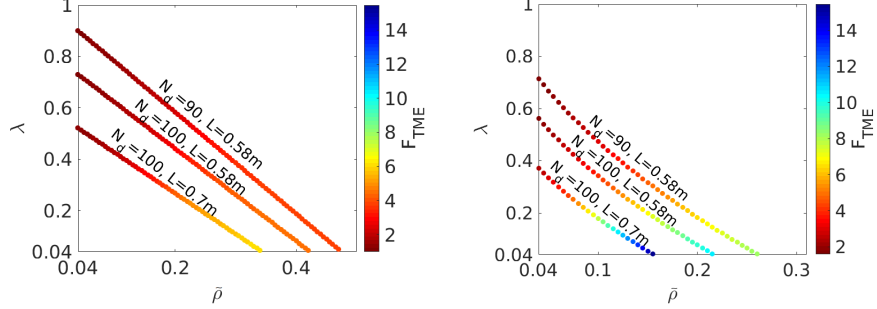


Figure 4.6: The parametrization of the  $F_{TME}$  with  $\tilde{\rho}$  and  $\lambda$ , when fixing  $N_d$  and  $L$ , for the step (left) and the trapezium (right) profile.

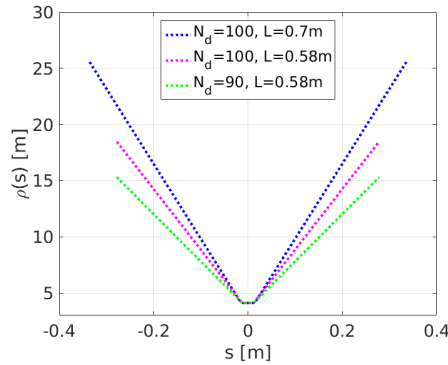


Figure 4.7: The variation of the bending radius along the dipole length for different  $(N_d, L)$  pairs, resulting in the highest emittance reduction (where  $\lambda = 0.04$ ) for each case, for the case of the trapezium profile.

After imposing the  $\theta$ ,  $L$  and  $\rho_1$  values in Eq. (4.28), a relationship between  $\tilde{\rho}$  and  $\lambda$  is obtained and can be inserted in Eq. (4.25) for obtaining the respective emittance reduction factors. In this way, the maximum emittance reductions for fixed dipole characteristics are found. Figure 4.6 shows the parameterization of the  $F_{TME}$  with  $\tilde{\rho}$  and  $\lambda$ , for both dipole profiles and again with the restriction of  $\lambda, \tilde{\rho} > 0.04$ , for three different cases of  $(N_d, L)$  pairs: (100, 0.7 m), (100, 0.58 m) and (90, 0.58 m). The case of (100, 0.58 m) corresponds to the exact bend characteristics of the CLIC DR. For the dipole constraints applied in each case, the trapezium gives always higher reductions than the step profile. Obviously, the more and the longer the dipoles are, the higher emittance reductions are achieved. The maximum reductions in all cases are localized where both  $\lambda$  and  $\tilde{\rho}$  are low. Large  $\lambda$  values are not of interest since the  $F_{TME}$  gets very small. The  $\tilde{\rho}$  values that result in the highest emittance reductions are lower for the trapezium case. The variation of the bending radius along the dipole length that results in the highest emittance reduction for each

case of  $(N_d, L)$  pair, is plotted in Fig. 4.7 for the case of the trapezium profile. As was expected from Fig. 4.6, the maximum emittance reductions (where  $\lambda = 0.04$ ) correspond to different  $\tilde{\rho}$  values for each pair of  $(N_d, L)$  and thus, for a fixed minimum bending radius ( $\rho_1=4.1$  m), their maximum bending radii differ.

# Alternative CLIC DR design using longitudinally variable bends and high field wigglers

---

In this Chapter, a numerical application of the analytical solutions shown in Chapter 4, is presented for the CLIC DR [16] TME cell. The DR lattice design is driven by the emittance requirements which for ultra-low values give rise to collective effects [16], with intra-beam scattering (IBS) being the dominant one. An alternative design is proposed, which aims to mitigate the IBS effect for a compact ring, using in the arc cells the designed variable bend presented earlier and an optimized high-field wiggler in the FODO cells. The optimization steps followed, as well as the final parameters for the improved design are discussed.

The magnet design of a variable bend according to the characteristics of a dipole with the optimal field variation, is described. The technological limitations of the magnet design are used as constraints in order to study the impact of a variable bend on the optics functions of the cell and on the properties of the ring. Extending the analytical approach for the TME cells with uniform dipoles [33], the parametrization of the quadrupole strengths and optics functions with respect to the drift lengths and the emittance is derived for a non-uniform dipole.

Based on the analytical thin-lens solutions and the numerical simulations performed with MAD-X [20], appropriate initial conditions are chosen for matching the CLIC DRs lattice through numerical optics codes. The optimization strategy followed to reduce the circumference of the DRs design, when using longitudinally variable bends at the arcs and high field wigglers at the long straight sections of their layout, is explained. Finally, the parameters of the new alternative design are compared with respect to the ones of the previous design.

## 5.1 Longitudinally variable field dipole design for the CLIC Damping Rings

The analytical results showed that the trapezium dipole profile can reach very low emittances, compared to a uniform dipole of the same bending angle. Therefore, the fabrication of a variable dipole having a bending radius that forms a trapezium shape is of interest. According to the optimal characteristics of a trapezium bending profile to be used for the CLIC Damping Rings, the magnetic design of a longitudinally variable dipole based on permanent magnets was studied and the prototype will be fabricated by CIEMAT [73, 74]. The main challenges of this design are the bending radius variation which should change linearly along the magnet and the high field region length that is very short. The longitudinal gradient with a trapezoid decay is solved by

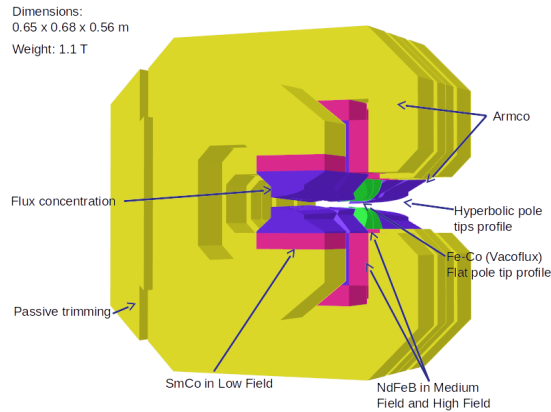


Figure 5.1: Magnet design based on the characteristics of the variable bends for the CLIC DRs [73, 74].

splitting the magnet in three differentiated field regions combined with an innovative variable gap solution, as presented in Fig. 5.1. The low field block is made of SmCo materials. The medium

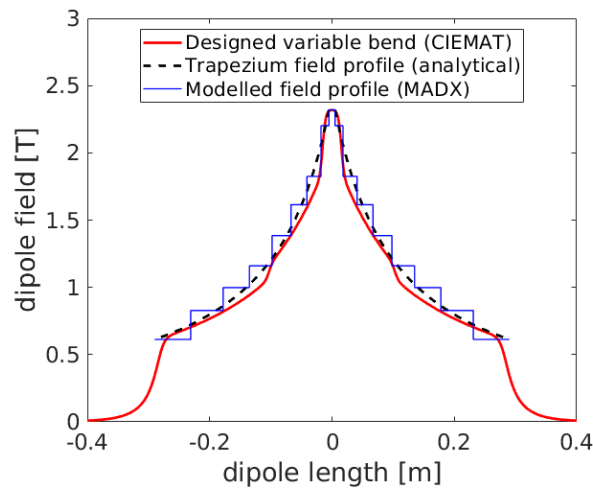


Figure 5.2: The field variation along a dipole having a peak field of 2.3 T; the designed trapezium profile (red colored), the resulted from analytical calculations profile (black colored) and the field profile that is simulated in MAD-X (blue colored).

field has the same configuration as the high field section, using NdFeB blocks. The requested peak field was limited to 1.77 T as a reasonable value for a non-superconducting magnet, requiring to deal with iron saturation that is partially overcome using a Fe-Co material and suppressing the hyperbolic profile in the high field region pole tip which is the most saturated section.

The higher is the magnetic field at the center of a variable bend, the higher emittance reduction factors can be reached. The use of permanent magnets could allow having a higher field than in the case of a normal conducting magnet which can reach around 1.8 T. The 3D simulations performed showed that the peak field could be increased above 2 T, resulting in higher

emittance reduction factors compared to the case of 1.77 T. In Fig. 5.2, a 2.3 T designed trapezium profile is shown in red. The field decay successfully matches the desired from the analytical results hyperbolic field profile (black colored). For the designed trapezium profile, the  $\lambda$  and  $\tilde{\rho}$  values achieved are respectively 0.036 and 0.295, corresponding to an emittance reduction factor  $F_{TME} = 7.1$ <sup>1</sup>. For the beam optics simulations performed with the MAD-X code, the field of the designed trapezium profile is being approximated by a sequence of dipoles with step-like field (blue colored). Furthermore, since a transverse gradient of -11 T/m was requested<sup>2</sup>, the designed magnet provides at the same time dipolar and quadrupolar fields, having pole tips with a hyperbolic profile to produce the gradient.

## 5.2 Numerical application for a variable bend TME cell

According to the design of a variable bend, the maximum dipole field is set to be 2.3 T (minimum bending radius  $\rho_1 = 4.1$  m), for dipoles having a length of  $L = 0.58$  m. The maximum pole tip field of the quadrupoles and the sextupoles is  $B_q^{\max} = 1.1$  T and  $B_s^{\max} = 0.8$  T respectively. By fixing those parameters the free parameters left are the drift space lengths  $s_1$ ,  $s_2$ ,  $s_3$  and the emittance. The stability criterion and the feasibility constraints that are applied to chose appropriately the cell characteristics, are given in this section. Most of the times it is preferable to detune the cell from the TME to larger emittances, so that to get more relaxed solutions for the cell's characteristics. A careful detuning of the TME cell that obeys the restriction given by Eq. (4.27), is necessary.

### Stability and feasibility constraints

The criterion, for both horizontal and vertical planes, that ensures the optics stability and that is used for restricting the cell characteristics is given by:

$$|\cos\varphi_{x,y}| < 1 . \quad (5.1)$$

The pole tip field value of both quadrupoles and sextupoles has a limit and the radius of the magnet aperture has a minimum value. The feasibility of the quadrupoles is ensured if the quadrupole strength  $k$  is kept below a maximum value given by:

$$k = \frac{1}{fl_q} \leq \frac{1}{(B\rho)} \frac{B_q^{\max}}{R_{\min}} , \quad (5.2)$$

where  $B\rho$  is the magnetic rigidity and  $B_q^{\max}$  is the quadrupole pole tip field. The quantity  $R_{\min} = \sqrt{\beta\varepsilon_{\max} + ((\frac{\delta p}{p_0})_{\max}D)^2}$  is the minimum required aperture radius for a Gaussian beam distribution, where  $\varepsilon_{\max}$  is the emittance and  $(\frac{\delta p}{p_0})_{\max}$  the momentum deviation that corresponds to the point where the particles displacement is maximum. As the sextupoles are set to cancel the chromaticity induced by the quadrupoles, their strength can be calculated by the

<sup>1</sup>The technological restrictions do not allow  $\tilde{\rho}$  to go down to 0.263 that is the optimal value for a  $\lambda = 0.036$ , giving a  $F_{TME} = 8.3$ .

<sup>2</sup>For a combined function dipole that has a small defocussing gradient, the IBS effect is reduced through the increase of the vertical beam size at the center of the bend [75].

condition:  $\xi_{x,y} = -\frac{1}{4\pi} \oint \beta_{x,y} [K_{x,y}(s) - S(s)D(s)] ds = 0$ , where  $K_{x,y}$  correspond to the focusing and defocusing quadrupole strengths. For  $B_s^{\max}$  being the pole tip field of the sextupoles, their feasibility is ensured if the strength  $S$  is lower than a maximum value that is:

$$S \leq \frac{2B_s^{\max}}{R_{\min}^2} \frac{1}{(B\rho)} . \quad (5.3)$$

### Parameterization with the drift lengths

Aiming to solutions with low chromaticities and small quadrupole strengths, while keeping the cell compact, a scanning of drift space lengths combinations was performed. The dependence of different cell characteristics on the drift space lengths require their parametrization with  $s_1$ ,  $s_2$ ,  $s_3$ . Since low chromaticity solutions are of interest, the parametrization of the horizontal  $\xi_x$  and vertical  $\xi_y$  chromaticities with the drift lengths is studied and is presented in Fig. 5.3.

The chromaticities were calculated for all combinations of drift lengths when  $s_1[m] \in (0.2, 2)$ ,

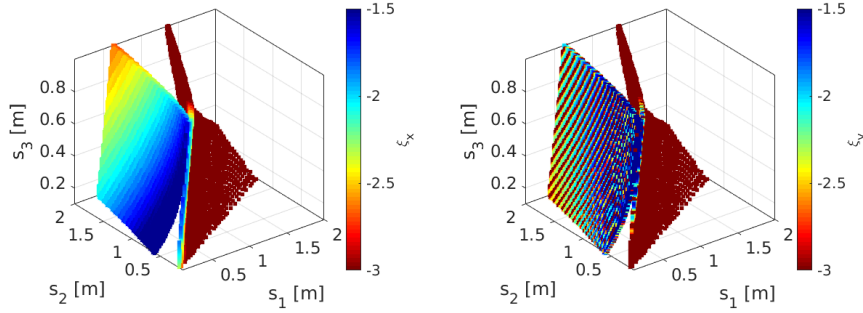


Figure 5.3: The horizontal (left) and vertical (right) chromaticities are parametrized with  $s_1, s_2, s_3$  for the TME, for the trapezium dipole profile.

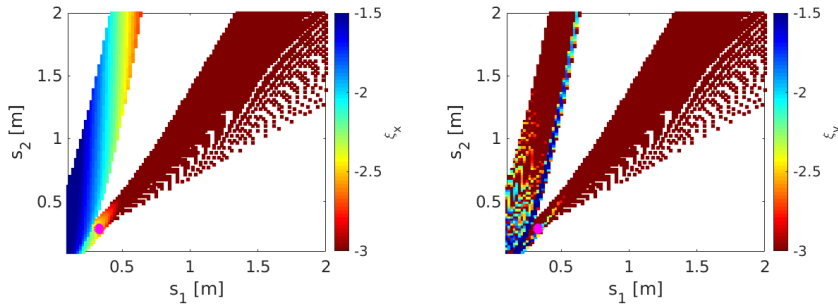


Figure 5.4: Parameterization of the horizontal (left) and vertical (right) chromaticities with  $s_1, s_2$  for the TME, for the trapezium dipole profile.

$s_2[m] \in (0.2, 2)$  and  $s_3[m] \in (0.2, 1)$ . Two regions can be distinguished; one for  $s_1 < 0.5$  m and another for  $s_1 > 0.5$  m, having respectively low and high negative chromaticities. The horizontal chromaticity depends strongly on  $s_2$ . The chosen drift lengths should comply with the fact that for the TME, the lowest negative chromaticities in both planes are found where  $s_1 < 0.5$  m and  $s_2 > 0.5$  m. The absolute minimum emittances exist only for chromaticities that are  $\xi_x < -2$

and  $\xi_y < -1$ . Detuning factors that give emittances larger than the TME can provide solutions with lower negative chromaticities. Although a careful choice of  $s_1$  and  $s_2$  is essential, the system is less dependent to  $s_3$ . It should be also stressed that only a small fraction of the  $(s_1, s_2)$  combinations satisfy the feasibility requirements. The parametrization of the chromaticities with the drift space lengths, taking into account the feasibility constraints, assists in choosing the optimal values that are found to be:  $s_1 = 0.28$  m,  $s_2 = 0.18$  m and  $s_3 = 0.18$  m.

### Parameterization with the emittance

After having fixed the drift lengths, the parametrization with the emittance detuning factor provides important information about some cell properties. The emittance value that was so far determined by the reduction factor  $F_{TME}$ , is increased with this detuning. The actual emittance reduction that depends on the relation between the detuning and the reduction factor can be found using Eq. (4.26). The plots in Fig. 5.5 give parameterizations with respect to the detuning factor, considering always the stability criterion.

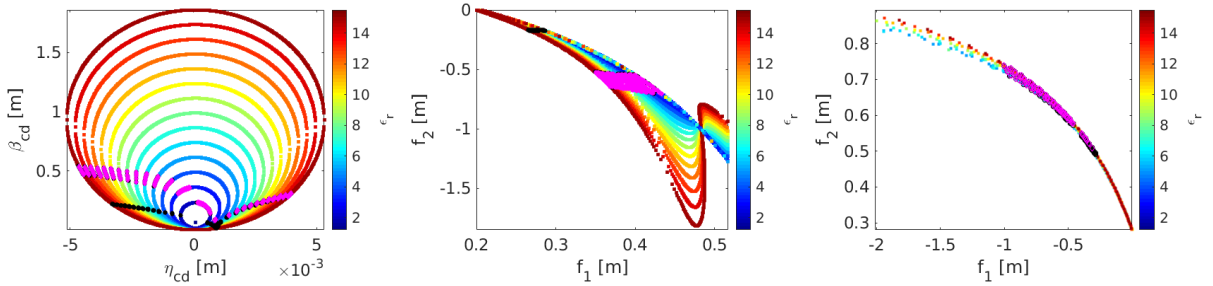


Figure 5.5: Parameterization of the beta and dispersion functions at the dipole center  $\beta_{cd}$ ,  $\eta_{cd}$  (left) and of the focal lengths, for  $f_1 > 0$ ,  $f_2 < 0$  (center) and for  $f_1 < 0$ ,  $f_2 > 0$  (right), with the detuning factor. The black squares indicate stability and the magenta ones feasibility-low chromaticities solutions.

The elliptical curves in Fig. 5.5 (left) represent the pairs of the beta and dispersion functions at the dipole center that result in the same emittance. Similarly, the parametrization of the focal lengths with the emittance detuning factor is given in Fig. 5.5 (center) for  $f_1 > 0$  and  $f_2 < 0$ , where the pairs of  $(f_1, f_2)$  lie again on constant emittance curves. Solutions with  $f_1 < 0$  and  $f_2 > 0$  which correspond to the modified TME cell [76], also exist and they are presented in Fig. 5.5 (right), with a focus on the stability and feasibility solutions. The TME ( $\varepsilon_r = 1$ ) is achieved for a unique pair of beta and dispersion functions that is  $(\eta_{cd}, \beta_{cd}) = (1.093 \times 10^{-4}$  m, 0.065 m) and only for one pair of focal lengths which is  $(f_1, f_2) = (0.261$  m,  $-0.139$  m). The small focal length values indicate that in order to tune the cell to the TME strong quadrupole strengths are needed. For the chosen drift lengths, there are no solutions that assure stability and low chromaticities for the absolute TME ( $\varepsilon_r = 1$ ). Solutions that assure lattice stability (black points) and for chromaticities  $\xi_x, \xi_y > -2.5$  (magenta points) arise when moving away from the TME to larger detuning factors, i.e.  $\varepsilon_r > 1$ . Solutions with both focal lengths positive are unstable as they always provide defocussing in the vertical plane. Even if the chosen cell characteristics result in a confined  $\varepsilon_r$  region, the low emittances reached for a very compact cell counteract the fact that it is numerically challenging to tune the cell.

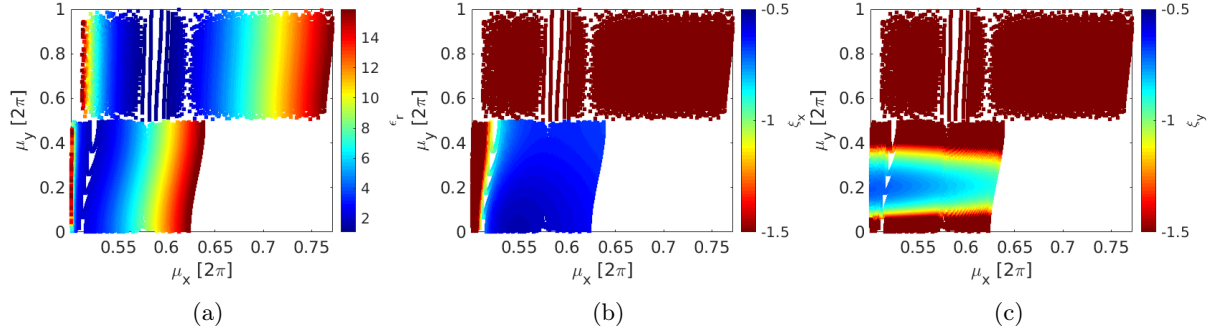


Figure 5.6: Parameterization of the detuning factor (a) and the chromaticities  $\xi_x$  (b) and  $\xi_y$  (c) with the horizontal  $\mu_x$  and vertical  $\mu_y$  phase advances, for  $f_1 > 0$ ,  $f_2 < 0$ , for the trapezium dipole profile.

Figure 5.6 shows the parametrization of the detuning factor  $\varepsilon_r$  (a) and of the horizontal  $\xi_x$  (b) and vertical  $\xi_y$  (c) chromaticity with the horizontal  $\mu_x$  and vertical  $\mu_y$  phase advances, for the case of  $f_1 > 0$ ,  $f_2 < 0$  solutions which appear only when  $\mu_x > 0.5 \cdot 2\pi$ . Towards high vertical phase advances, the chromaticities for both planes have high negative values ( $\xi_x, \xi_y < -3$ ). Large horizontal phase advances correspond to minimum dispersion and beta functions at the center of the dipole that require strong focusing and to that end, result in high chromaticities. It can be noticed that for  $\mu_y < 0.5 \cdot 2\pi$ , there are low negative chromaticities even for small detuning factors corresponding to emittances close to the minimum one. There is only one phase advance pair that gives the theoretical minimum emittance for the chosen dipole characteristics and that is  $\mu_{x_{TME}} \simeq 0.62 \cdot 2\pi$ .

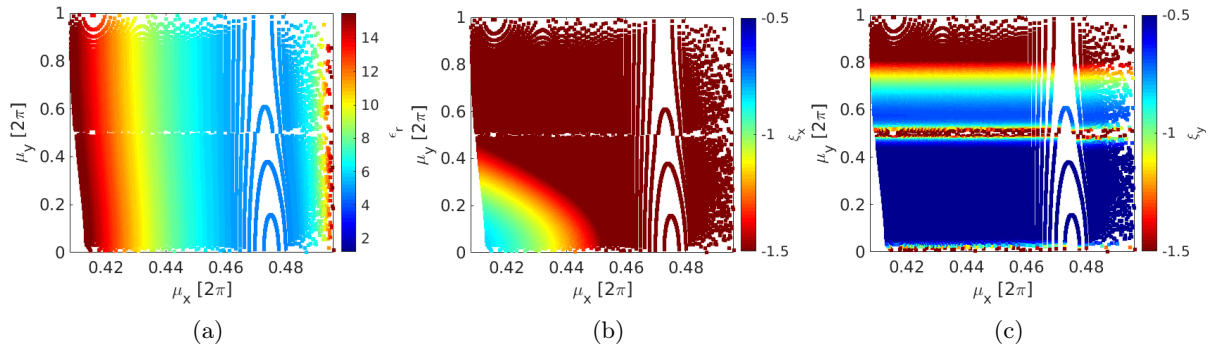


Figure 5.7: Parameterization of the detuning factor (a) and the chromaticities  $\xi_x$  (b) and  $\xi_y$  (c) with the horizontal  $\mu_x$  and vertical  $\mu_y$  phase advances, for modified TME cell where  $f_1 < 0$ ,  $f_2 > 0$ , for the trapezium dipole profile.

Solutions for  $f_1 < 0$ ,  $f_2 > 0$ , corresponding to the modified TME cell [76], also satisfy the stability criteria for the chosen cell characteristics and are presented in Fig. 5.7. These solutions appear always for  $\mu_x < 0.5 \cdot 2\pi$ . The quadrupole strengths for the modified TME cell are lower compared to the normal TME cell, as presented in Fig. 5.5 (right). Knowing the  $F_{TME}$  for the designed variable bend, the restriction described in Eq. (4.27) sets an upper limit to the

detuning of the cell. Since the modified TME cell requires a large detuning in order to get low horizontal chromaticities, the final emittance reductions reached are not sufficient. In this respect, the normal TME cell (having  $f_1 > 0$ ,  $f_2 < 0$  solutions) will be further used for the following numerical application to the CLIC DR optics design.

### 5.3 Alternative CLIC DR design

The DR lattice [16] has a racetrack shape with arc sections composed by the most compact low emittance cells, the TME cells. The two long straight sections (LSS) are composed by RF cavities, injection and extraction equipment and FODO cells filled with damping wigglers that are necessary for reaching low emittances within a fast damping time. The super-conducting magnet wigglers used in the current design have a  $B_w = 2.5$  T peak field and  $\lambda_w = 5$  cm period.

The DR lattice design is driven by the emittance requirements which for ultra-low values give rise to collective effects [16], with intrabeam scattering (IBS) being the dominant one. An alternative design which aims to mitigate the IBS effect for a compact ring, using in the arc cells the designed variable bend presented earlier and an optimized high-field wiggler in the FODO cells, is proposed. The optimization steps followed, as well as the final parameters for the improved designs are discussed in this section.

#### Optimization of the arc TME cell

For the beam optics simulations performed with the MAD-X code [20], the field variation of the designed trapezium profile is being approximated by a sequence of dipoles with varying field, as illustrated in Fig. 5.2. The dipole length is  $L = 0.58$  m and the maximum dipole field is 2.3 T. For a combined function dipole, i.e. having a small defocussing gradient (see section 5.1), the IBS effect is reduced through the increase of the vertical beam size at the center of the bend. Basically, instead of having a low  $\beta$  at the center of the dipole in both planes, the optics matching imposes  $\beta_y$  to be maximum there. Therefore, there is a reduction of IBS growth rates. After fixing the characteristics of the dipole, the drift space lengths are chosen in accordance with the results presented in Section 5.2.

Keeping in mind that a TME cell with a combined function dipole reduces the IBS effect [75], assists in choosing the proper phase advances, that guarantee low chromaticities and small quadrupole strengths. The parametrization with the emittance has shown that the quadrupole strengths for which  $f_1 > 0$  and  $f_2 < 0$  (Fig. 5.6), can only be found for  $\mu_x > 0.5 \cdot 2\pi$ . A good compromise for the horizontal phase advance is to be around  $0.51 \cdot 2\pi$  and for the vertical phase advances to be always below  $0.5 \cdot 2\pi$ . After a detailed scanning of the cell characteristics, the horizontal and vertical phases advances of the TME cell are respectively chosen to be around  $0.51 \cdot 2\pi$  and  $0.11 \cdot 2\pi$ .

When the uniform dipoles of the current design are replaced by variable bends, the resulted emittance is lower than the required one. In this case, the subtraction of some TME cells from the existing arc is possible. Actually, the number of dipoles (i.e. total number of TME cells) can be reduced to such an extent that the required emittance is still achieved, thereby resulting in a shorter ring. In this respect, it was possible to reduce the number of dipoles down to  $N_d = 90$  for the case of the designed trapezium profile with a 2.3 T maximum field.

### Optimization of the FODO cell

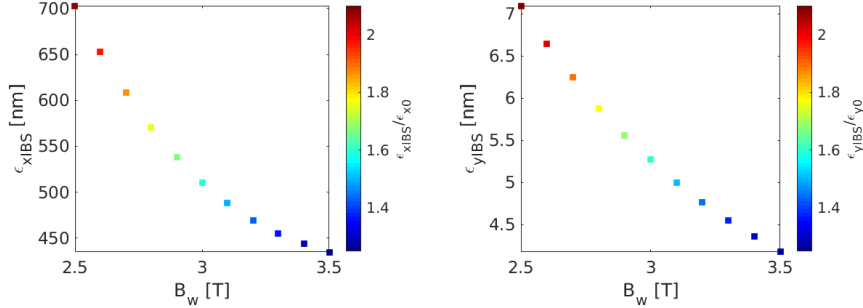


Figure 5.8: The dependence of the steady state emittances ( $\epsilon_{xIBS}$  and  $\epsilon_{yIBS}$ ) and their ratio with the corresponding equilibrium emittances ( $\epsilon_{x0}$  and  $\epsilon_{y0}$ ) on the wiggler peak field  $B_w$ , for the trapezium dipole profile.

The damping wigglers are necessary for achieving low emittances within a fast damping time. Each FODO structure of the LSS accommodates two wigglers. The use of super-conducting technology is mandatory in order to have a high wiggler field and a relatively short period for obtaining low emittances and fast damping time. It was shown that by targeting higher wiggler fields not only the emittance but also the IBS effect can be reduced [57, 77]. Taking into account the optimization of the arc cells and the fact that the emittance with IBS is significantly lowered after increasing the wiggler's peak field, the FODO cells per LSS can be reduced from 13 down to 10. The plots in Fig. 5.8 show the MAD-X results of the parametrization of the steady state transverse emittances including the IBS effect with the wiggler peak field  $B_w$ , starting from the 2.5 T that is the field of the previous wiggler design, for the 10 FODO cells. Clearly, the wiggler field increase corresponds to a significant reduction of the IBS effect. Regarding the fact that the required output emittance is 500 nm-rad, a new working point for the damping wigglers that complies with the technological restrictions is proposed to be at 3.5 T and with a 49 mm period length. This design necessitates a different wire technology, using  $Nb_3Sn$  material [78].

### Layout and optical functions

The layout of the ring is shown in Fig. 5.9. The final lattice, with a smaller number of dipoles and wigglers than the ones of the existing design, is produced. In Fig. 5.10 (left), the matched optics, i.e. horizontal dispersion, horizontal and vertical beta functions, are plotted for one arc TME cell. On the top part of the figure, a schematic layout of the cell is presented, showing the two doublets of quadrupoles and the sextupoles that are placed between the two mirror symmetric defocusing quadrupoles and between the dipole and the focusing quadrupoles. In Fig. 5.10 (right), the matched optics of the dispersion suppressor-beta matching section followed by the wiggler FODO cell, are presented.

### Dynamic aperture

The on- and off-momentum dynamic aperture (DA) of the ring was estimated for particles tracked with the PTC module of MAD-X [20]. Fig. 5.11 shows the maximum initial positions of particles

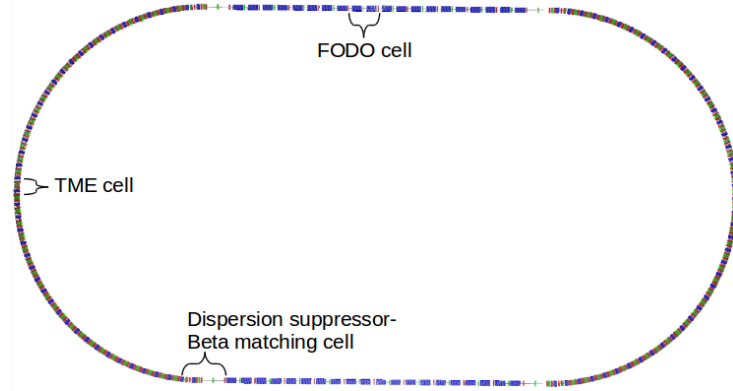


Figure 5.9: Schematic layout of the CLIC DR.

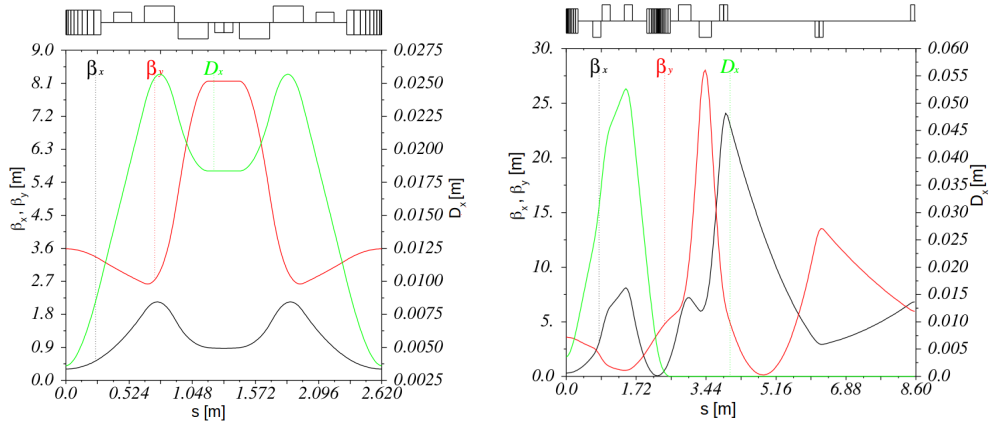


Figure 5.10: Optical functions of the TME cell (left) and of the dispersion suppressor-beta matching section followed by the FODO cell (right), when using in the arcs the trapezium dipole profiles.

that survived over 1000 turns, normalized to the horizontal and vertical beam sizes, at the point of calculation ( $\sigma_x = 273.0 \mu m$  and  $\sigma_y = 40.2 \mu m$ ). This simulation includes the effect of chromaticity sextupoles and magnets fringe fields but no other additional imperfection such as misalignments or magnet errors. The results for  $\delta p = 0$  are shown in blue, for  $\delta p = 0.5\%$  in red and for  $\delta p = -0.5\%$  in yellow. The dynamic aperture achieved is remarkable (almost 14 mm in the horizontal plane and 5 mm in the vertical plane), allowing very comfortable on-axis injection. A working point optimization, with simulations including misalignments, coupling and their correction, the non-linear effect of wigglers and space charge tune-shift, was further studied to fully quantify the non-linear performance of the new design [79], which was found robust and adequate.

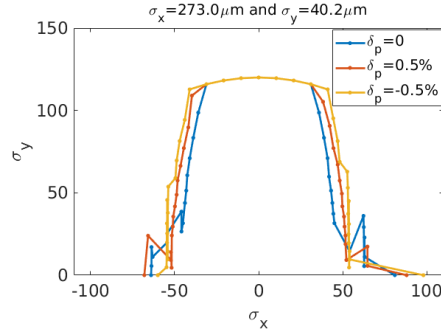


Figure 5.11: The on-momentum ( $\delta p = 0$ ) dynamic aperture of the DR for the trapezium dipole profile.

## 5.4 CLIC DR design parameters for the original and the improved design

The parameters of the original design and the alternative one are displayed in Table 5.1. It can be noticed that both lattices reach the target emittances including IBS, as calculated by the Bjorken-Mtingwa formalism through MAD-X [20]. The case of the low energy CLIC for  $N_b = 5.7 \times 10^9$  and  $V_{RF} = 6.5\text{MV}$  [80] (see Appendix D) was also studied for the new design and as was expected due to the larger bunch population that renders IBS stronger, the final emittances are increased up to 472 nm and 4.6 nm in the horizontal and the vertical plane, respectively. One of the main advantages of the alternative design is that the damping ring becomes around 13 % shorter. Also, the fact that the damping times are significantly reduced is beneficial for all collective effects, including IBS.

Table 5.1: Parameters for the original and the improved CLIC DRs design, for the case of  $N_b = 4.1 \times 10^9$ 

Parameters, Symbol [Unit]	Original design	Alternative design	
	uniform	uniform	trapezium
Energy, $E$ [GeV]	2.86	2.86	
Bunch population, $N_b$ [ $10^9$ ]	4.07	4.07	
Circumference, $C$ [m]	427.5	373.7	
Basic cell type in the arc/LSS	TME/FODO	TME/FODO	
Number of arc cells/wigglers, $N_a/N_w$	100/52	90/40	
RF Voltage, $V_{RF}$ [MV]	4.50	6.50	
Harmonic number, $h$	2850	2493	
RF Stationary phase [ $^\circ$ ]	62.3	58.9	63.0
Momentum compaction, $\alpha_c$ [ $10^{-4}$ ]	1.3	1.3	0.88
Damping times, $(\tau_x, \tau_y, \tau_l)$ [ms]	(1.98, 2.05, 1.04)	(1.24, 1.28, 0.33)	(1.19, 1.23, 0.31)
Energy loss/turn, $U$ [MeV]	4.0	5.6	5.8
Quadrupole gradient strengths, $(k_1, k_2)$ [T/m]	(26, -53)	(66, -98)	(67, -98)
Phase advances per arc cell, $(\mu_x, \mu_y)$ [ $360^\circ$ ]	0.408/0.050	0.510/0.110	
Horizontal and vertical tune, $(Q_x, Q_y)$	(48.35, 10.40)	(51.16, 14.56)	(51.18, 14.55)
Horizontal and vertical chromaticity, $(\xi_x, \xi_y)$	(-113, -82)	(-57, -70)	(-67, -75)
TME cell length, $L_{cell}$ [m]	2.44	2.62	
Dipole field, $(B_{min}, B_{max})$ [T]	(0.97, 0.97)	(0.97, 0.97)	(0.62, 2.32)
Lengths and bending radii ratio, $(\lambda, \tilde{\rho})$	(1, 1)	(1, 1)	(0.04, 0.26)
Normalized gradient in dipole [ $m^{-2}$ or T/m]	-1.1 or -10.5	-1.1 or -10.5	
Wiggler peak field, $B_w$ [T]	2.5	3.5	
Wiggler length, $L_w$ [m]	2	2	
Wiggler period, $\lambda_w$ [cm]	5.0	4.9	
without IBS			
Normalized horiz. emittance, $\gamma\varepsilon_x$ [nm-rad]	312.2	574.1	350.3
Normalized vert. emittance, $\gamma\varepsilon_y$ [nm-rad]	3.3	3.3	
Energy spread (rms), $\sigma_\delta$ [%]	0.11	0.15	
Bunch length (rms), $\sigma_s$ [mm]	1.4	1.6	
Longitudinal emittance, $\varepsilon_l$ [keVm]	4.4	5.8	
with IBS			
Normalized horiz. emittance, $\gamma\varepsilon_x$ [nm-rad]	478.9	648.7	434.7
Normalized vert. emittance, $\gamma\varepsilon_y$ [nm-rad]	5.0	4.5	4.2
Energy spread (rms), $\sigma_\delta$ [%]	0.11	0.15	
Bunch length (rms), $\sigma_s$ [mm]	1.5	1.6	
Longitudinal emittance, $\varepsilon_l$ [keVm]	4.7	5.8	
IBS factors hor./ver./long.	1.53/1.52/1.08	1.13/1.35/1.01	1.24/1.26/1.02

# IBS Simulations for the CLIC DRs

Lepton machines, such as future linear collider damping rings and new generation light sources, operate in regimes where the IBS effect can be predominant. Therefore, it is important to understand the parameters the IBS effect depends on. In this chapter, the IBS results from MAD-X (B-M analytical formalism) and SIRE are presented for the alternative CLIC DR design which was discussed in Chapter 5. A benchmarking of the IBS theoretical models with Monte-Carlo codes was presented in [57] for lepton rings. Also, a validation of the SIRE IBS routine has been performed on the CLIC DR lattice design [47].

## 6.1 The IBS growth rates along the CLIC DR

As was explained in Chapter 3, the IBS growth rates for all theories and approximations have a complicated dependence on the beam properties, the beam optics and the equilibrium rms transverse emittances and energy spread. The basic performance parameters of the alternative CLIC DR design are summarized in Table 5.1. The variation of the beta and the dispersion functions that determine the IBS growth rates are plotted in Fig. 6.1 for the CLIC DR, for the horizontal (black) and vertical (red) plane.

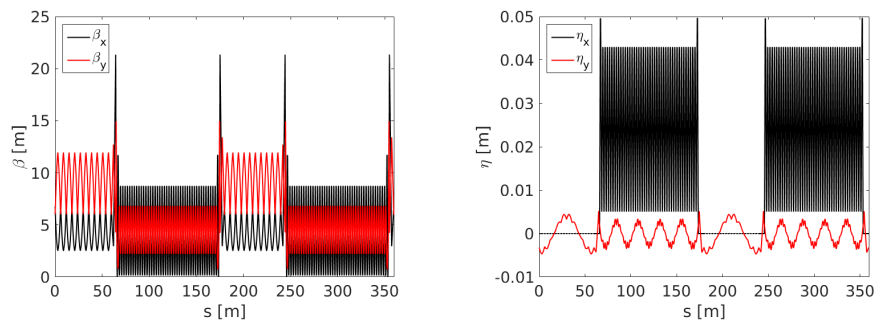


Figure 6.1: The beta (left) and dispersion (right) functions, in the horizontal (black) and vertical (red) plane, along the CLIC DR.

The IBS growth rates were calculated for the full optics of the CLIC DR, using the IBS module of the Methodical Accelerator Design code (MAD-X) [45] which is based on the Bjorken-Mtingwa formalism (see 3.3). For the IBS growth rate calculations, it is important that the IBS kicks are distributed over an adequate amount of points across the ring, such that the variation of the optics is taken into account. The starting emittance values are the zero current equilibrium ones. The steady state emittances, at least for the cases under study, do not depend on the starting point. Figure 6.2 shows the IBS growth rates in the longitudinal (green), the horizontal

(blue) and the vertical (magenta) plane. The left axis corresponds to the vertical ( $T_y$ ) and the right axis to the longitudinal ( $T_l$ ) and horizontal ( $T_x$ ) IBS growth rates. In the long straight sections which are dispersion free regions, the  $T_x$  is very small, meaning that the IBS effect in the horizontal plane is minor. On the other hand, in the arcs which are dispersive regions, due to the fact that the dispersion couples the horizontal and longitudinal planes, part of the IBS growth is transferred from the longitudinal to the horizontal plane and so,  $T_x$  is larger.

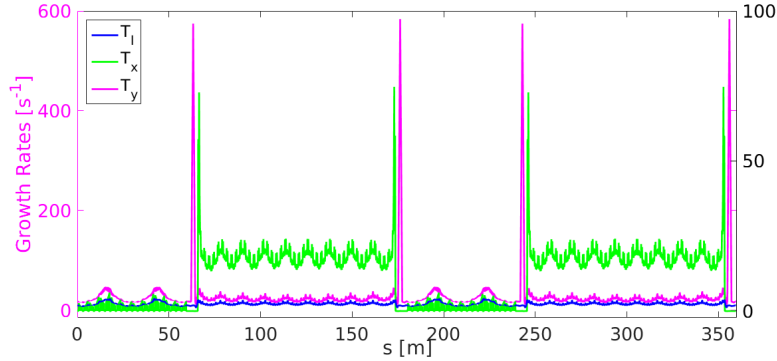


Figure 6.2: The IBS growth rates in all three planes, along the CLIC DR.

## 6.2 Benchmarking of the B-M IBS theoretical model with SIRE

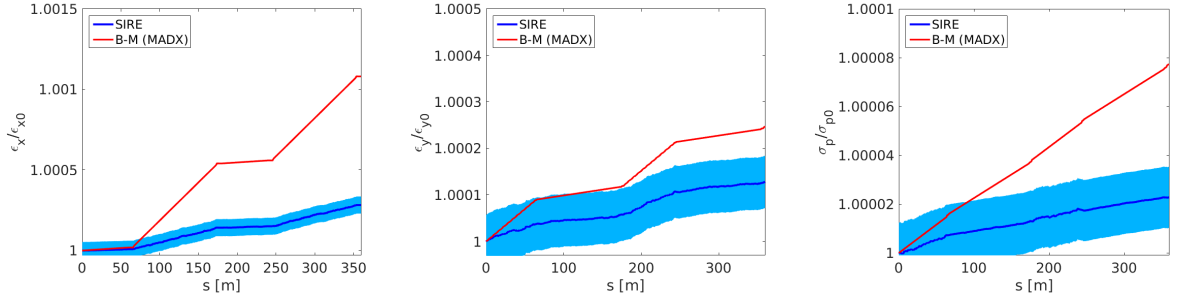


Figure 6.3: One turn comparison between the tracking code SIRE and the B-M theoretical model for the CLIC DR, showing the growth of the horizontal (left), vertical (center) emittance and energy spread (right).

It is important to benchmark the existing IBS theoretical models, in the presence of synchrotron radiation and quantum excitation, with the tracking codes and identify their limitations. In this section, the theoretical model of Bjorken-Mtingwa (B-M) is compared to the simulations performed with SIRE for the CLIC DR. Figure 6.3 shows the growth of the horizontal (left) and vertical (center) emittances and energy spread (right) in one turn, as calculated by B-M (red) and SIRE (blue). Due to the fact that in SIRE the generation of the distribution is based on a random number generator, the tracking simulations were performed several times, resulting in the two standard deviation error-bars that are plotted in light blue.

Taking into account the results presented in Fig. 6.2, the fact that the dispersion plays a very important role in the redistribution of the phase space due to the IBS effect is nicely demonstrated in Figure 6.3. In agreement with what was discussed earlier, the one turn growth shows that the IBS effect in the horizontal plane is minor at the dispersion free regions (long straight sections) and becomes significant at the dispersive regions (arcs). Since the vertical dispersion is very small (Fig 6.1 (right)) and the betatron coupling is considered to be zero, the vertical plane is uncoupled from the other two. It can be noticed that the trend of the emittance evolution is the same for the B-M theoretical model and for SIRE. The SIRE simulation algorithm uses the Rutherford cross-section to calculate the scattering probability in a solid angle, while the B-M analytical formalism, which always overestimates (compared to other theories) the IBS effect, uses a different approach.

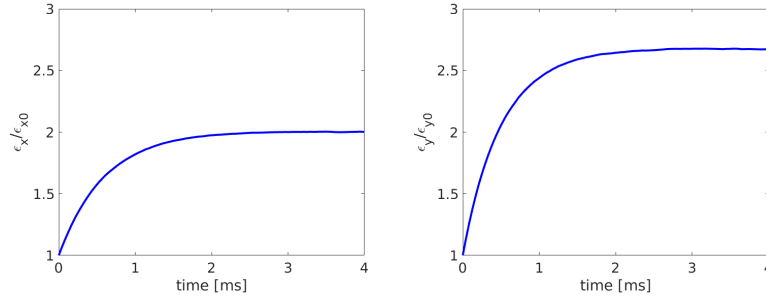


Figure 6.4: The emittance growth in the horizontal (left) and vertical (right) plane until convergence (steady states), as calculated by SIRE, for the CLIC DR.

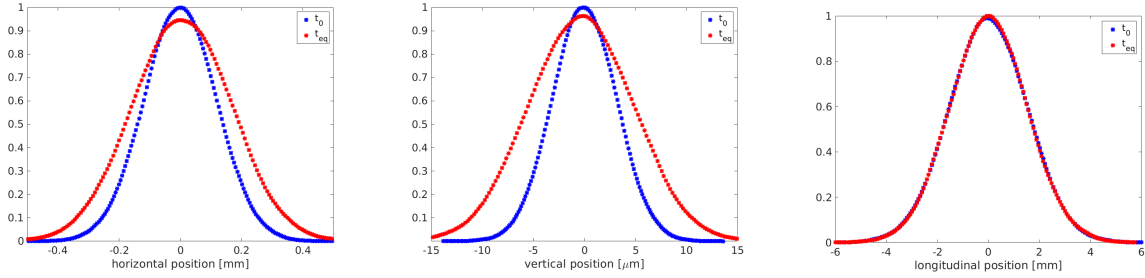


Figure 6.5: The variation of the distributions in the horizontal (left), vertical (center) and longitudinal (right) plane till the equilibrium emittance is reached, as calculated using SIRE.

Table 6.1: Initial and final (at equilibrium) fit results for the horizontal, vertical and longitudinal bunch profiles shown in Fig. 6.5, for the CLIC DRs.

Fit Parameters	Horizontal distribution		Vertical distribution		Longitudinal distribution	
	<i>Initial</i>	<i>Final</i>	<i>Initial</i>	<i>Final</i>	<i>Initial</i>	<i>Final</i>
$\sigma_{rms}$ [ $\mu m$ ]	$119.0 \pm 3$	$164.0 \pm 3$	$3.2 \pm 10^{-3}$	$5.1 \pm 10^{-3}$	$1515.0 \pm 18$	$1513.0 \pm 21$
$RMSE$ [ $10^{-3}$ ]	3	6	3	4	3	3

The growth of the emittances until convergence (steady states), using the SIRE code for the

calculations, is presented in Figure 6.4, for the horizontal (left) and vertical (right) plane. The growth in the longitudinal plane is less than 1% and thus, it is not shown here. Figure 6.5 shows the variation of the horizontal (left), vertical (center) and longitudinal (right) distributions till the equilibrium emittance is reached. The input distributions tracked using SIRE were Gaussian and they remain Gaussian till convergence. The initial and the final (steady states) distributions are color-coded with blue and red, respectively. In Table 6.1 the variation of the rms beam sizes is given for the transverse and longitudinal distributions. The beam sizes are increased by almost 40% and 60% in the horizontal and vertical plane, respectively. In the longitudinal beam size remains practically the same.

# Bunch profile measurements at the LHC

## 7.1 Transverse bunch profile instruments

The beam parameters at the high energy of the LHC require special measurement techniques in order to get the beam size and so the transverse emittance. The transverse diagnostic instruments used are the betatron matching monitor [81], the beam gas ionization monitor [82], the beam wire scanners (WS) [83] and the Beam Synchrotron Radiation Telescope (BSRT) [84]. Compatibly with high intensity and high energy operation, the BSRT is the only instrument offering non-invasive, continuous and single bunch measurements of the LHC beams.

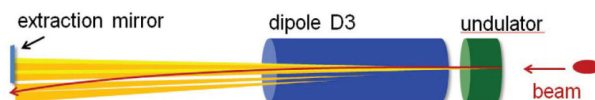


Figure 7.1: Sketch of the BSRT Synchrotron light sources [85].

The LHC is equipped with two SR monitors (one per beam) used to characterize the transverse and longitudinal beam distributions. The light emitted by a superconducting undulator and/or by a dipole magnet (depending on the beam energy) is sent to the BSRT, as sketched in Fig. 7.1. It is worth noting that the undulator and the dipole are installed in a dispersion free region. The visible synchrotron light emitted by the protons in IR4 is imaged on a fast gated CCD (Charge-Coupled Device) camera, providing a beam 2D image from which the beam size in the transverse plane can be extracted. Although the BSRT measurements are very precise when averaging over several acquisitions, their quality is mainly limited by the accuracy of the calibration.

The BSRT is calibrated with respect to the WS during dedicated low beam intensity runs <sup>1</sup>, by assuming Gaussian beam sizes and a Gaussian instrument resolution  $\sigma_{LSF}$  for the BSRT [85]. In this respect, the beam size measured by the BSRT is expressed as:

$$\sigma_{BSRT_{meas}}^2 = \sigma_{BSRT}^2 + \sigma_{LSF}^2, \quad (7.1)$$

Given the optical functions at the location of the SR source, the beam emittance can be calculated by:

$$\varepsilon_{BSRT} = \sigma_{BSRT}^2 \gamma / \beta, \quad (7.2)$$

<sup>1</sup>The WS can measure the emittance throughout the full LHC machine cycle including the energy ramp, provided that the total intensity in the machine is limited to  $\sim 240$  nominal bunches at 450 GeV and  $\sim 12$  nominal bunches at 6.5 TeV.

The  $\sigma_{LSF}$  factor, the  $\gamma$  Lorentz factor and the  $\beta$  optical function vary according to the energy (FB or FT) and to the plane (horizontal or vertical) the bunch profile measurement is taken.

### Examples of transverse bunch profiles in the LHC (BSRT)

An example of the BSRT profiles observed in the LHC is shown in Fig. 7.2 (left) for a single bunch at a specific time. The frequency each bunch is seen by the BSRT depends on the total number of bunches in the machine and on the settings the BSRT experts apply. It can be that at a specific time slot, that is every almost 1 sec, there are more than one measurements for each bunch, as the ones shown in Fig. 7.2 (blue, green and red). In this case, during each time slot there is a specific number of bunches observed, having for each one of them a few measurements (usually 3 to 5) that can be averaged to obtain a single distribution for the beam size estimation. Sometimes, for optimizing in case the machine is full or when having bunches of different intensities, only one measurement of a single bunch per time step is acquired.

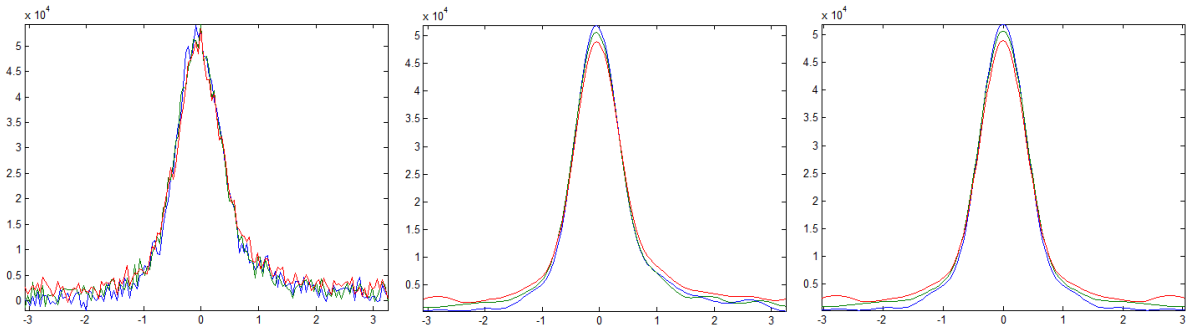


Figure 7.2: The BSRT profile measurements (blue, green and red lines) for a single bunch at a specific time, before applying any noise filter (left), after performing an FFT noise cleaning (center) and when symmetrically duplicating the left side (right).

In order to eliminate the noise of the BSRT profiles, a Fast Fourier Transform (FFT) is used. The Fourier Transform of a function of time can be considered as a relative measure of how much the function oscillates with a specific frequency. Since the frequencies of the original signal appear as spikes in the Fourier Transform graph, the dominant frequencies within a noisy signal can be identified. Once these spikes are found, the inverse Fourier Transform for these frequencies can be performed so that to obtain the original signal without the accumulated noise. By keeping the dominant frequencies found from the FFT graph, the reconstructed bunch profiles obtained after performing an inverse FFT, are presented in Fig. 7.2 (center).

Sometimes only the left part of the BSRT profiles should be considered. In such cases, the left side of the profiles is duplicated and then it is flipped horizontally, such that to be finally merged with the original left side of the distributions. Figure 7.2 (right) shows the symmetrically duplicated bunch profiles to be considered for calculating the beam size.

## 7.2 Longitudinal bunch profile instruments

Due to the fact that there is no direct method to measure the longitudinal emittance in circular accelerators, a parameter that is generally used in measurements is the bunch length (Eq. (2.70)). If all accelerator parameters are known, including the potential-well distortion effect <sup>2</sup>, the bunch length can be used to infer the emittance. The projection of the distribution function on the phase axis which is known as the bunch profile or line density, gives the bunch length.

The bunch length is operationally measured by the LHC Beam Quality Monitor (BQM) [86] which uses a wall current monitor pick-up (WCM) [87] to acquire the longitudinal profiles. Additionally, the longitudinal synchrotron radiation monitor (BSRL) [88] continuously measures the longitudinal distribution of charges in the beams. It uses the same synchrotron light source as the BSRT, but it measures the temporal distribution of the incoming light. The transfer functions of the pickups and cables were measured and are used for deconvolution [89]. The scopes connected to the WCM pick-ups can acquire longitudinal bunch profiles of both beams during a full LHC cycle.

### Examples of longitudinal bunch profiles in the LHC

During the energy ramp, the bunches in the LHC are blown up longitudinally in order to avoid instabilities due to the loss of Landau damping [90], and this results in non-Gaussian longitudinal distributions at the start of collisions [91]. An example showing the evolution of a longitudinal particle distribution during 11.5 h at collisions (6.5 TeV) in the LHC is presented in Fig. 7.3. The blue colored profile that corresponds to the start of collisions demonstrates that the bunch arrives at FT energy with a clearly non-Gaussian shape. Later in time, the interplay between SR and IBS results in a profile formation that is more Gaussian.

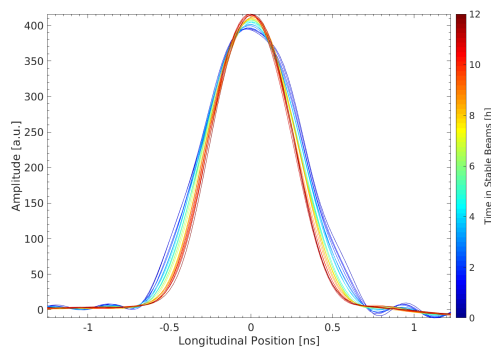


Figure 7.3: The evolution of a longitudinal bunch profile during 11.5 h at collisions (6.5 TeV).

In the case of the LHC, the full width at half maximum (FWHM) of the line density is used to calculate the longitudinal beam size. While this measurement is precise, the measured bunch length only accurately represents the r.m.s. width provided that the longitudinal distribution is

<sup>2</sup>For a stable bunch in the stationary case, the induced voltage distorts the rf potential well with respect to the ideal case, causing a shift of the stable fixed point and modifying the effective voltage seen by the particles. The latter leads to a shift in the synchrotron frequency and a change of the bunch length.

Gaussian. In order to have a complete understanding of the longitudinal emittance, specially for bunches with non-Gaussian tails, it is more accurate to determine the bunch length using the standard deviation rather than just the FWHM of the distribution.

### 7.3 Probability distribution functions for the LHC bunch profiles

In the LHC, the interplay between IBS and a series of other effects, including longitudinal beam manipulations, non-linearities of the machine or noise, can enhance the tails of the beam distributions which may become non-Gaussian. It is therefore important, in the case of non-Gaussian profiles, to make use of alternative (not Gaussian) functions to fit appropriately the measured distribution. As was mentioned earlier in this chapter, both the WS and the BSRT measurements use the Gaussian function to fit the transverse bunch profiles observed in the LHC. The distribution function used to describe the non-Gaussian longitudinal bunch profiles in the LHC [89] is the binomial discrete probability distribution. For  $k$  successes out of  $n$  trials, the binomial distribution approximates the Gaussian distribution only when  $n$  is very large. One of the alternatives used for fitting beam distributions with non-Gaussian tails is the double Gaussian, that is basically the sum of two normal distributions having different standard deviation values. Statistically the double Gaussian is a probabilistic model for representing the presence of sub-populations within an overall population, without requiring that an observed data set should identify the sub-population to which an individual observation belongs. Practically, a double Gaussian function can describe non-Gaussian tailed distributions better than a single Gaussian.

Among all the functions mentioned for fitting the particle distributions observed in the LHC (Gaussian, binomial and double Gaussian), only the q-Gaussian [92] which is described in detail below, provides the flexibility to accurately describe the core and the tails at the same time. Fitting a “heavy” or “light” tailed distribution with the q-Gaussian function reveals its preponderance among the other functions. Therefore, for the bunch profiles studied and presented in this thesis, the q-Gaussian function is used.

#### The q-Gaussian function

In order to describe more accurately bunch profiles with tails that differ from the ones of a normal distribution, a generalisation of the Gaussian distribution function, the q-Gaussian [92], can be employed. This distribution has a probability density function given by:

$$f(x) = \frac{\sqrt{\beta^{qG}}}{C_q} e_q(-\beta^{qG} x^2). \quad (7.3)$$

If the distribution needs to be centered on zero, the location parameter  $\mu$  should be included in the density function as:

$$f(x) = \frac{\sqrt{\beta^{qG}}}{C_q} e_q(-\beta^{qG} (x - \mu)^2). \quad (7.4)$$

The  $q$ -exponential function is given by: The  $q$ -exponential function is given by:

$$e_q(x) = \begin{cases} \exp(x) & , \text{ if } q = 1 \\ (1 + (1 - q)x)^{\frac{1}{1-q}} & , \text{ if } q \neq 1 \text{ and } (1 + (1 - q)x) > 0 \\ 0 & , \text{ if } q \neq 1 \text{ and } (1 + (1 - q)x) \leq 0 \end{cases} . \quad (7.5)$$

The parameter  $q$  describes the weight of the tails, in the sense that the larger it is, the heavier the tails become, as presented in Fig. 7.4. In the limit of  $q \rightarrow 1$ , the distribution becomes a normal distribution. The distribution is characterized as “light” tailed when  $q < 1$  and as “heavy”

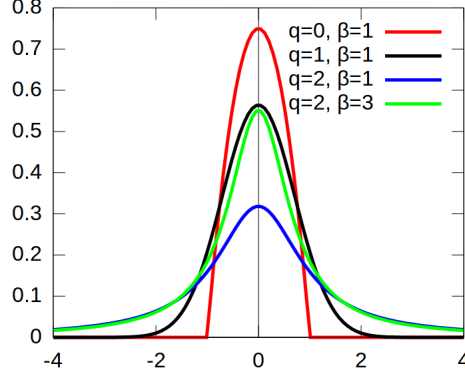


Figure 7.4: The  $q$ -Gaussian distribution function for different  $q$  and  $\beta^{qG}$  values.

tailed when  $q > 1$ . The normalization factor  $C_q$  differs for specific ranges of the  $q$  parameter, it is written as:

$$C_q = \begin{cases} \frac{2\sqrt{\pi}}{(3-q)\sqrt{1-q}} \frac{\Gamma\left(\frac{1}{1-q}\right)}{\Gamma\left(\frac{3-q}{2(1-q)}\right)} & \text{for } -\infty < q < 1 \\ \sqrt{\pi} & \text{for } q = 1 \\ \frac{\sqrt{\pi}}{\sqrt{q-1}} \frac{\Gamma\left(\frac{3-q}{2(q-1)}\right)}{\Gamma\left(\frac{1}{q-1}\right)} & \text{for } 1 < q < 3 \end{cases} \quad (7.6)$$

The parameter  $\beta^{qG}$  is a real positive number. As the normal distribution, the  $q$ -Gaussian is an even function taking its maximum at  $x = 0$ , where

$$f(0) = \frac{\sqrt{\beta^{qG}}}{C_q}. \quad (7.7)$$

For a certain  $q$  value, the higher is the value of  $\beta^{qG}$ , the larger is the maximum of the probability density function, as can be observed in Fig. 7.4. The standard deviation also differs for specific ranges of the  $q$  parameter, it is:

$$\sigma = \begin{cases} \sqrt{\frac{1}{\beta^{qG}(5-3q)}} & \text{for } q < 5/3 \\ \infty & \text{for } 5/3 \leq q < 2 \\ \text{undefined} & \text{for } 2 \leq q < 3 \end{cases} \quad (7.8)$$

The Box-Muller transform has been generalized to allow random sampling from  $q$ -Gaussians [93].

Based on Eq. (7.9), the distribution is equivalent to the Student’s  $t$ -distribution with a direct mapping between  $q$  and the degrees of freedom  $\nu$ , in the heavy tail regime only (since  $\nu+3 > \nu+1$  and so,  $q > 1$ ). Statistically the  $q$ -Gaussian is a scaled reparametrization of the Student’s  $t$ -distribution [94] for which the parameter  $\nu$  is constrained to be a positive integer related to the sample size. The advantage of the  $q$ -Gaussian function is that, by introducing the parameters  $q$

and  $\beta^{qG}$ , a generalization of the Student's t-distribution to negative and or non-integer degrees of freedom is possible.

$$q = \frac{\nu + 3}{\nu + 1} \quad \text{with} \quad \beta^{qG} = \frac{1}{3 - q} \quad (7.9)$$

## 7.4 Example of transverse bunch profiles at the LHC FT energy

In a circular collider, a certain crossing angle is required for colliding bunch trains so that to separate the two beams after collision. The magnitude of this crossing angle is a complicated function of the bunch charge, the number of long-range beam-beam (LRBB) interactions [95–97], of the  $\beta^*$  and of the optics. The LRBB interactions can be a source of emittance growth that may lead to beam losses in the LHC during physics [98]. For the case of the High Luminosity LHC upgrade (HL-LHC) with the small  $\beta^*$  and the high bunch intensities, such effects are enhanced.

During the LHC operation period, apart from the physics fills, there are specific days dedicated to machine development (MD) studies, which are carefully planned in the LHC operation schedule to optimize and further study the performance of the machine. One of the 2017 MD studies was the beam-beam long-range (BBLR) MD [99]. This MD had a primary goal to verify and establish the minimal crossing angle between beam 1 (B1) and beam 2 (B2) that is important for the luminosity leveling by crossing angle [100], by collecting observations to optimize the operational configuration, confirming the asymmetric behavior of B1 and B2 and understanding the critical BBLR regime.

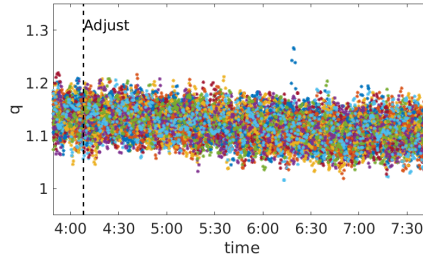


Figure 7.5: The evolution of the  $q$  parameter for a train of BCMS bunches at FT energy (6.5 TeV) versus time (left).

During the BBLR MD the transverse bunch profiles were acquired for both beams, using the BSRT [84, 85]. After having put the beam in collision at top energy, the half crossing angle of IP1 and IP5 was reduced in steps from 150 until 90  $\mu\text{rad}$  within 3 h. The evolution of the  $q$  parameter in time (after adjust) for the acquired profiles is shown for the horizontal plane of B1 in Fig. 7.5. Starting from values of the order of 1.15 the  $q$  parameter decreases gradually in time, i.e. the profiles become more Gaussian. Due to the fact that the number of BBLR experienced by each bunch is related to the position of each bunch in a train, specific patterns are expected to be observed along a train of bunches, specially when the crossing angle is significantly reduced. So, it is important to plot the quantities that are of interest versus the bunch slot number. In this respect, in Fig. 7.6 the  $q$  (left) and  $\beta^{qG}$  (right) parameters of the q-Gaussian fit are plotted over the bunch slot number and are color-coded with time. In general, all bunches become more Gaussian, since  $q$  decreases as time evolves. The bunches at the center of the train, which have

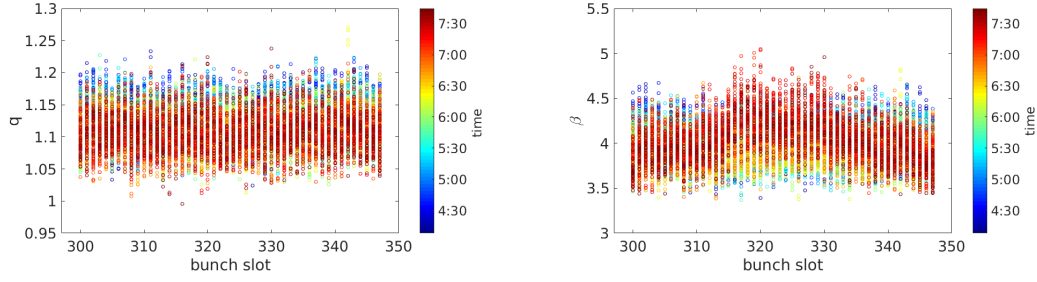


Figure 7.6: The evolution of the  $q$  (left) and of the  $\beta^{qG}$  (right) parameters for a train of BCMS bunches at FT energy (6.5 TeV) versus the bunch slot number.

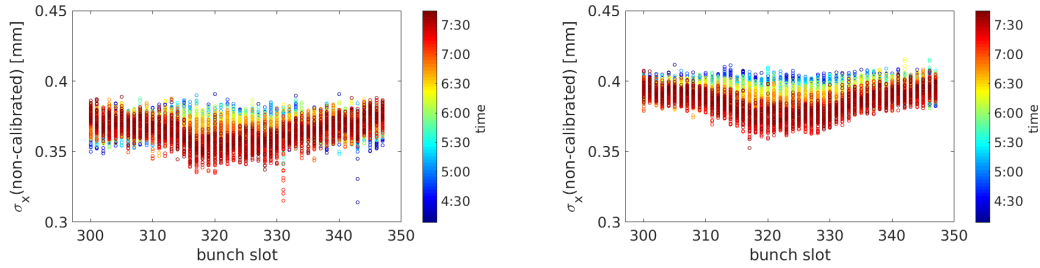


Figure 7.7: The evolution of the horizontal rms beam size (non-calibrated), as calculated by the Gaussian (left) and the q-Gaussian (right) fits, for a train of BCMS bunches during 3.5 h at FT energy (6.5 TeV), versus the bunch slot number.

more BBLR encounters than the ones at the edges of the train, correspond to larger  $\beta^{qG}$  values. Similar plots are shown for the Gaussian and the q-Gaussian rms beam sizes in Fig. 7.7. The beam size values presented in these plots are the non-calibrated ones<sup>3</sup> because the existing calibration factors to correct the rms values can be applied only for Gaussian distributions [85], and thus, their magnitude should not be taken into account. The comparison of the Gaussian and the q-Gaussian non-calibrated beam sizes shows that the Gaussian fit- which cannot describe well the observed overpopulated tails, underestimates the real beam size. For both the Gaussian and the q-Gaussian case there is a clear correlation between the beam size and the BBLRs encountered by the bunches along the train.

<sup>3</sup>The BSRT is calibrated with respect to the wire scanners (WS) [83] during dedicated low beam intensity runs.

# Luminosity observations and estimations

---

Operating at  $6.5\text{ TeV}$ , the LHC surpassed the expectations and delivered an average of  $66\text{ fb}^{-1}$  integrated luminosity to the two high luminosity experiments ATLAS and CMS by the end of 2018 (see Fig. 1.3). Aiming to gain some of the luminosity lost during collisions, the crossing angle is gradually reduced (anti-leveling process) [101, 102]. In view of increasing the integrated luminosity, the beams are initially squeezed to a  $\beta^*$  of  $30\text{ cm}$  that is further reduced to  $25\text{ cm}$  after some hours in collisions according to the ATS (Achromatic Telescopic Squeeze) [103] optics scheme. In order to provide a continuous feedback to the machine coordination for further optimizing the performance, an automated tool for monitoring the main beam parameters and machine configurations, has been devised and extensively used. Estimates, based both on simulations and on observed beam parameters, were reported fill-by-fill as well as in overall trends during the Run 2.

## 8.1 Emittance observations in the LHC

In Fig. 8.1 the BSRT convoluted (average of two beams) emittances at the start of collisions are compared to the ones of the emittance scans [104] and to the ones extracted by the luminosity of the LHC experiments (ATLAS and CMS), for the 2018 BCMS Fills. The pink solid lines correspond to BSRT calibration Fills and the dashed ones to Technical Stops (TS). Except for the periods before Fill 6700 and for Fills 7100-7220 having BSRT hardware issues (gray colored areas), for most of the year the BSRT emittances are underestimated. The agreement of the emittance scans [105] with the emittances inferred from luminosity is  $5-20\%$  and, the emittances from Wire Scanners (WS) [106] are up to  $10-15\%$  lower than the ones extracted from luminosity, based on the results presented in [107] for a BSRT calibration Fill. Since the BSRT is calibrated with respect to the WS, the discrepancy between the BSRT and the emittances estimated from luminosity is something to be expected. In 2017, the emittance estimations coming from the different methods agree well, within the uncertainties of each measurement, except for specific periods where the BSRT measurements are diverging [101].

Understanding the discrepancy between different emittance measurements is important since they play a key role for the luminosity estimations as well as, for the validation of the data quality. One of the studies to explain these differences, focuses on fitting accurately the beam distributions. The importance of that was discussed in [108] for the longitudinal distributions, in order to get a better bunch length estimation. Moreover, the bunch by bunch analysis for various Fills during Run 2, underlines the seriousness of fitting accurately the transverse bunch profiles that determine the transverse emittances.

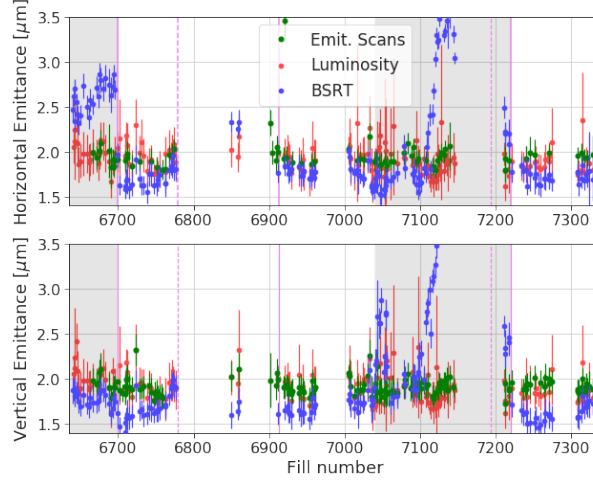


Figure 8.1: Convoluted (average of the two beams) emittances for the 2018 Fills in the horizontal (top) and vertical (bottom) plane, from Emittance scans (green), Luminosity (red) and BSRT (blue).

## Emittance calibration in the LHC

The divergence from the expected emittance values coming from luminosities was guiding the BSRT calibration along the LHC Run 2. As was discussed in Chapter 7, the BSRT is calibrated with respect to the WS during dedicated low beam intensity Fills. Certainly, such a calibration determines the values of the measured emittances. A BSRT calibration Fill from the LHC Run 2

Table 8.1: Injected emittances of bunch slots during a BSRT calibration Fill, based on Gaussian fitting.

Bunch slots	Emittance [ $\mu m$ ]
3 and 450	5
891 and 1200	3
1500 and 1785	1.8
2100 and 2450	1.2

is taken as a case study example (Fill 6293 in 2017) in order to understand the impact of fitting accurately the observed beam profiles on the estimation of the transverse beam size and therefore, on the emittance. The accuracy of the calibration technique can be improved by using a wide range of emittances. During the calibration Fill used as example here, 8 bunches per beam of various emittances were injected (at 450 GeV), they are listed in Table 8.1. The BSRT profiles of these bunches were fitted using both the Gaussian and the q-Gaussian distribution function. Figure 8.2 presents the resulted q parameter, that describes the weight of the distribution tails, of the q-Gaussian fits for the first minutes after these bunches were injected in the LHC. First of all, the bunches injected with large emittances (i.e. bunch slots 3 and 450) are more Gaussian ( $q \approx 1$ ) compared to the other bunches. This is related to the way these bunches are blown up in the injectors, so that to have various emittances when injected in the LHC. There are also some differences between the horizontal (top) and vertical (bottom) plane, with the horizontal bunch profiles having slightly lighter tails compared to the vertical ones. While the reduction of the

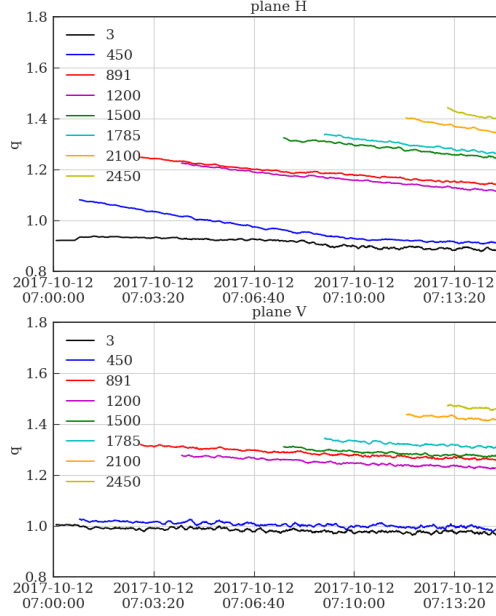


Figure 8.2: Evolution of the weight of the distribution tails, given by the  $q$  parameter, for bunches which are injected in the LHC having different emittances (see Table 8.1), in the horizontal (top) and in the vertical (bottom) plane.

$q$  parameter in time is obvious in the horizontal plane, in the vertical plane it remains almost constant. This means that for the specific calibration Fill at injection energy, as time evolves, the tails of the horizontal profiles become lighter and the vertical ones do not change.

In Figure 8.3, the rms beam sizes of the 8 bunches are plotted for the cases of fitting the profiles with the Gaussian (left) and the  $q$ -Gaussian (right) function. The rms beam sizes in the vertical plane are larger compared to the ones in the horizontal plane. The  $q$ -Gaussian rms differs significantly from the Gaussian one for bunches with small beam sizes that are heavy tailed (see Fig. 8.2). For the bunches having small emittances (i.e. bunches 1500, 1785, 2100 and 2450) the rms beam size can be underestimated by more than 20% if the Gaussian fitting function is used. So, the emittance values presented in Table 8.1, which are given for Gaussian profiles, will differ significantly for the heavy tailed bunches. Since the calibration is based on some emittance estimations that are inaccurate, this will eventually lead to forthcoming emittance measurements that are incorrect. Therefore, it is crucial to develop calibration techniques that take into account the actual shapes of the bunch profiles.

## 8.2 Observations and modeling of the LHC Luminosity

In the luminosity model [21], that is a numerical model used since 2016 to calculate the machine luminosity, for the evolution of the emittance, apart from the effects of IBS, SR and elastic scattering, the effects of betatron coupling, noise and burn-off have been also included in 2018 [109]. The comparison of the measurements to the results coming from the luminosity model assists in understanding the impact of mechanisms which are beyond the existing model, on the emit-

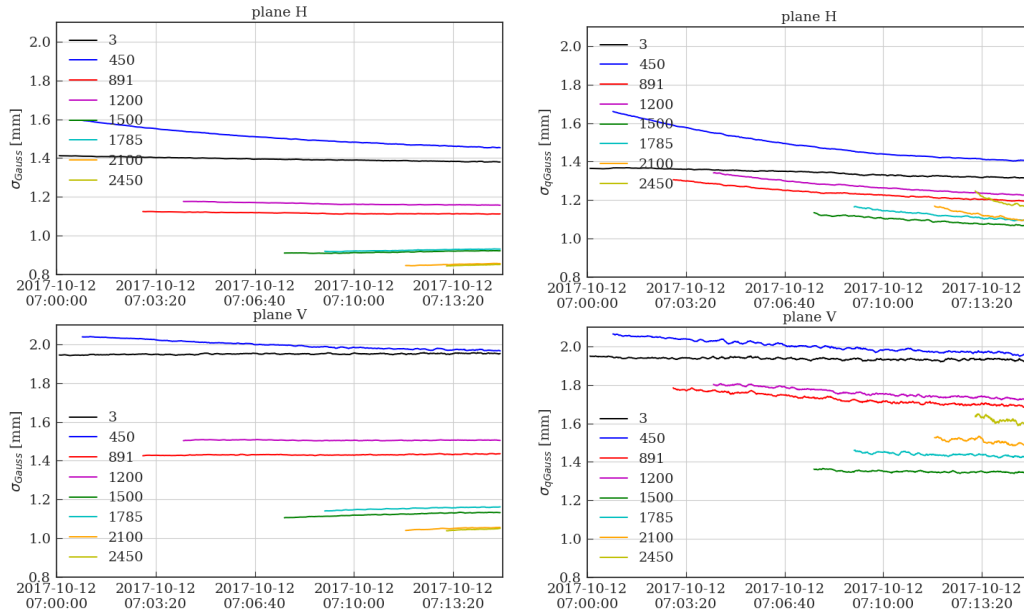


Figure 8.3: Evolution of rms beam sizes of bunches which are injected in the LHC with different emittances (see Table 8.1), for the case of fitting the profiles with the Gaussian (left) and the q-Gaussian (right) function, in the horizontal (top) and in the vertical (bottom) plane.

tance growth and therefore, on the luminosity degradation. In Figure 8.4, the bunch luminosity (averaged over all the colliding bunches) evolution is plotted for an example Fill of 2018. The luminosity degradation because of mechanisms that are beyond the model and result in an emittance blow-up, are plotted in light-blue and blue for the old and the updated model, respectively. The black curve corresponds to the average measured luminosity by the experiments. Although the updated model gives better emittance and luminosity predictions with respect to the measured luminosities by the experiments (i.e. ATLAS [1] and CMS [2]), there is still some room for improvement.

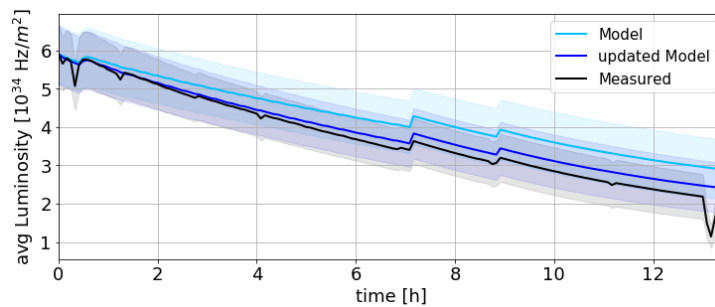


Figure 8.4: Luminosity evolution for an example 2018 Fill that stayed at collisions for 13 h, estimated using the old (in light-blue) and the updated model (in blue). The average measured luminosity by the experiments of ATLAS and CMS is plotted in black. The shadowed areas correspond to the one standard deviation error-bars.

The luminosity model was constructed based on the IBS module of MAD-X [45] which assumes Gaussian beam distributions. In order to understand the beam size evolution but also, the remaining discrepancy between the luminosity coming from the model and the measurements, the actual distribution shapes should be known. In view of quantifying the impact of non-Gaussian distribution tails on the calculated luminosity, the luminosity formula for q-Gaussian distribution functions is derived in Section 8.3.

### 8.3 Luminosity estimations

The performance of a collider is determined by the luminosity which, for two beams colliding head-on, is given by [8]:

$$\mathcal{L} = 2N_1N_2N_b f_{rev} \int \int \int \int_{-\infty}^{\infty} \rho_{1x}(x)\rho_{1y}(y)\rho_{1s}(s-s_0)\rho_{2x}(x)\rho_{2y}(y)\rho_{2s}(s+s_0) dx dy ds ds_0, \quad (8.1)$$

with  $N_{1,2}$  representing the number of particles per bunch for each beam,  $N_b$  the total number of colliding bunches,  $f_{rev}$  the revolution frequency and  $\rho$  the beam density distribution functions for each plane and beam.

Based on Eq. (8.1), assuming Gaussian beams that collide head-on, the luminosity is expressed as [8]:

$$\mathcal{L}^G = \frac{N_1N_2N_b f_{rev}}{4\pi\sigma_x^G\sigma_y^G}. \quad (8.2)$$

In order to achieve high luminosity, high intensity bunches and small beam sizes are required. The transverse beam sizes of two colliding Gaussian bunches are given by:

$$\sigma_x^G = \sqrt{\sigma_{1x}^2 + \sigma_{2x}^2} \quad \text{and} \quad \sigma_y^G = \sqrt{\sigma_{1y}^2 + \sigma_{2y}^2}. \quad (8.3)$$

Based on the transverse and longitudinal bunch profile measurements, it has been observed that the particle distributions in the LHC, both at collision and injection energies, appear to have shapes that differ from the ones of a normal distribution [59, 91, 110]. At the LHC injection energy, the emittance evolution is dominated by the IBS effect, both in the horizontal and in the longitudinal plane, while no effect is expected in the vertical plane [111], as was also shown in the previous section. From Run 2 data, it is observed that in many cases the transverse bunch profiles appear to be non-Gaussian during the whole injection plateau [110]. At the LHC collision energy, the IBS effect is weaker, while synchrotron radiation damping becomes more pronounced. The bunch profiles at collisions appear to have non-Gaussian tails, as well. In fact, during the energy ramp, the bunches that are blown up longitudinally in order to avoid instabilities due to the loss of Landau damping [90], arrive at the start of collisions with a clearly non-Gaussian shape [91].

By assuming that a particle distribution is Gaussian when this is not the case, not only the rms beam size may be underestimated or overestimated, but also its impact on performance parameters, such as the luminosity. Therefore, it is important to use appropriate fitting functions (or some type of interpolation algorithm) on the beam profile in order to properly address this discrepancy. A generalized Gaussian function, called the  $q$ -Gaussian [92], can be employed for

fitting more accurately bunch profiles with shapes that differ from the ones of a normal distribution (see Section 7.3 for the properties of this distribution function). The parameter  $q$  describes the weight of the tails as compared to the core, ranging from light tailed ones for  $q < 1$  (including the square distribution for  $q \rightarrow -\infty$ ) and extending to a heavy tailed ones for  $q < 1$ , passing through the Gaussian distributions in the limit of  $q \rightarrow 1$ . This distribution is actually a stationary solution of a generalised Fokker-Plank equation which can cover a full spectrum of statistical behaviour of dynamical systems, from sub to super-diffusion Levy-type processes [112].

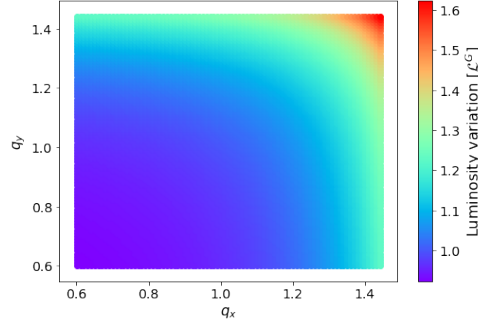


Figure 8.5: Parameterization of the luminosity variation, normalised to the corresponding Gaussian luminosity value  $\mathcal{L}^G$ , with the weight of the transverse distribution tails, given by the parameters  $q_{x,y}$ .

In view of quantifying the impact of non-Gaussian distributions, the luminosity is estimated through Eq. (8.1) by using the specified probability density functions. Assuming that the two beams are identical and that they collide head-on, the luminosity for  $q$ -Gaussian distribution functions in the transverse plane is given by:

$$\mathcal{L}^{qG} = \frac{N_1 N_2 N_b f_{rev}}{4\pi \sigma_x^{qG} \sigma_y^{qG}} \mathcal{I}_x^{qG} \mathcal{I}_y^{qG}, \quad (8.4)$$

for  $\sigma_{x,y}^{qG}$  being the beam sizes (see Section 7.3) in the transverse plane, for both beams. The factors  $\mathcal{I}_{x,y}^{qG}$  which depend on the parameter  $q$  in the respective planes and the details of the calculation are presented in Appendix E, together with the validation of the luminosity estimation for  $q$ -Gaussian distributions (shown in Fig. E.1). By comparing this equation to the standard luminosity formula for Gaussian beams with identical rms sizes, the significance of the tail population contribution on luminosity can be established and parameterised through  $q$ .

This is illustrated in Figure 8.5 where the luminosity variation normalised to the corresponding one for Gaussian beams  $\mathcal{L}^G$ , assuming the same beam parameters, is parameterized with the parameter  $q$  of the  $q$ -Gaussian fitting function, characterising the weight of the tails in the transverse plane assuming head on collisions (i.e. no dependence of the luminosity on the longitudinal beam size, see Appendix E). As  $q$  (and  $\beta^{qG}$ ) vary, when keeping the beam sizes in all planes fixed, the luminosity varies as well with respect to the one estimated for purely Gaussian beams. Practically, if the tails of a distribution differ by 10% compared to the ones of a Gaussian distribution, the luminosity value can be overestimated or underestimated by 5%. It is then clear that, for two beams colliding head-on, the shape of the transverse distributions has a significant impact to the estimated luminosity, in particular for the LHC experiments which target a  $\sim 2\%$  accuracy in their estimates [113]. The impact of non-Gaussian distributions on the luminosity

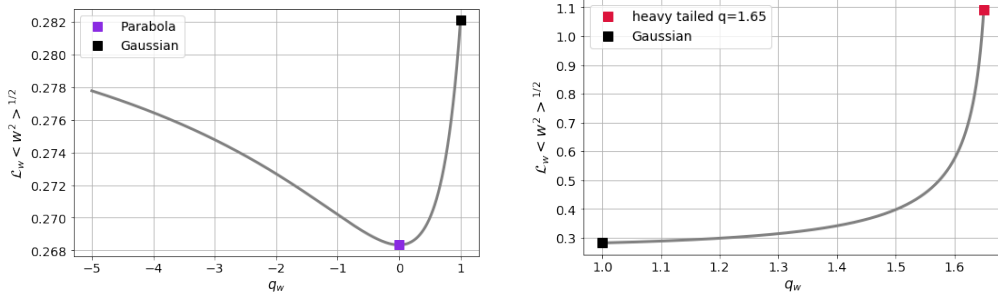


Figure 8.6: In order to estimate the divergence of the luminosity for non-Gaussian distributions from the one for Gaussian densities, the  $\mathcal{L}_w < w^2 >^{1/2}$  (see Eq. 8.5) is plotted versus the weight of the tails  $q$ , for light tailed (left) and the heavy tailed (right) distributions, i.e.  $q < 1$  and  $q > 1$ , respectively. The points corresponding to a parabola and a Gaussian distribution, firstly presented in [114, 115], are plotted.

was firstly discussed by Hereward [114]. In particular, the luminosity integrals were calculated for several distributions as the rectangular and the parabolic which correspond to a  $q$ -Gaussian with  $q \rightarrow -\infty$  and  $q = 0$ , respectively. Assuming that the two beams are identical and that they collide head-on, these distributions were used as examples to estimate the divergence from the luminosity for Gaussian densities. This divergence is calculated in one plane only as:

$$\mathcal{L}_w < w^2 >^{1/2} = \sigma_w \int_{-\infty}^{\infty} \rho(w)^2 dw \quad (8.5)$$

and it was found that [114, 115]:

$$\mathcal{L}_w < w^2 >^{1/2} = \begin{cases} 0.2887, & \text{for a rectangular distribution} \\ 0.2683, & \text{for a parabolic distribution} \\ \frac{1}{2\sqrt{\pi}} = 0.2821, & \text{for a Gaussian distribution} \end{cases} \quad (8.6)$$

with  $w = x, y$  and for  $\sigma_w$  being the transverse rms beam size, since these solutions correspond to the transverse plane. In fact, this approach already identified the existence of a minimum for a light tailed parabolic distribution, which becomes obvious by employing the  $q$ -Gaussian, as observed in Fig. 8.6, where  $\mathcal{L}_w < w^2 >^{1/2}$  is plotted versus  $q$  for  $q < 1$ , i.e. light tails (left), and  $q > 1$ , i.e. heavy tails (right). The results for  $q$ -Gaussian distributions (grey curves) are in perfect agreement with the case studies discussed in [114]. This is also true for a rectangular distribution which corresponds to a  $q$ -Gaussian with  $q \rightarrow -\infty$  and is beyond the range of the left plot of Fig. 8.6. For heavy tailed distributions, there is no upper limit for the constant of Eq. (8.6), as already inferred by Hereward [114]. In Fig. 8.6 (right) the case of a heavy tailed distribution with  $q = 1.65$  is denoted by a red square. The extreme case of  $q \rightarrow 5/3$  corresponds to a  $q$ -Gaussian whose rms size goes to infinity (i.e. Levy distributions, see Section 7.3).

By keeping the  $q$  parameter constant, here  $q = 1$ , and varying the beam size, the  $\beta$  parameter also varies. Figure 8.7 shows the luminosity variation that is parameterized with the variation of the parameter  $\beta$  (left) and, with the beam size variation (right), in the transverse plane. The variation of the  $\beta$  parameter together with the beam size variation result always in a Gaussian

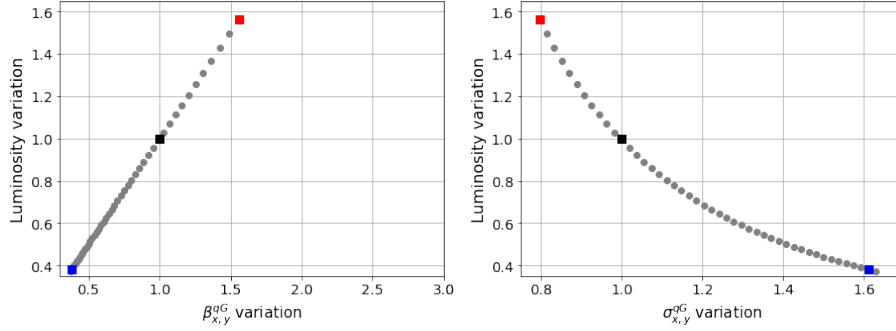


Figure 8.7: Luminosity variation with respect to an initial luminosity value for the specified same beam parameters, versus the variation of the  $\beta$  parameter (left) and the beam size (right) of the transverse distributions, keeping the  $q$  parameter constant. The variation of the  $\beta$  parameter together with the beam size variation result always in a Gaussian distribution, i.e.  $q = 1$ .

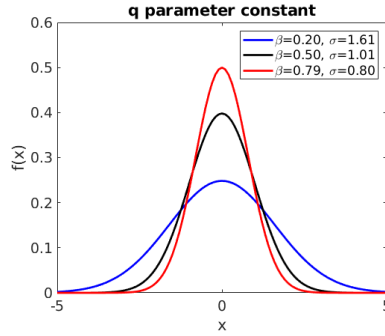


Figure 8.8: The  $q$ -Gaussian density distribution function for Gaussian bunch profiles ( $q = 1$ ), having different  $\beta$  parameters and beam sizes.

( $q = 1$ ) distribution. The blue, black and red points correspond to the bunch profile shapes that are plotted in Fig. 8.8, which are all Gaussian.

Figure 8.9 shows the luminosity variation with respect to the corresponding Gaussian luminosity value (denoted as  $\mathcal{L}^G$ ) for the same beam parameters. The luminosity variation is parameterized with the parameter  $q$  (left) of the  $q$ -Gaussian fitting function which characterizes the weight of a distribution's tails and with the  $\beta$  parameter (right), in the transverse plane (since there is no dependence on the longitudinal plane, see 8.4). Basically, this plot is similar to the one presented in Fig. 8.5 but, for the horizontal and vertical distributions being the same. The blue, black and red points correspond to a light tailed ( $q = 0.6$ ), a Gaussian ( $q = 1$ ) and a heavy tailed ( $q = 1.4$ ) distribution, respectively. The bunch profile shapes for these distributions are plotted in Fig. 8.10, having identical beam sizes (based on Eq. 7.8). Since the beam size is being kept constant and the  $q$  parameter varies, the  $\beta$  parameter of the  $q$ -Gaussian (see 7.3) also varies. As  $q$  (and  $\beta$ ) increases, for fixed beam sizes in all planes, the luminosity gets higher with respect to the one for the Gaussian case. Practically, if the tails of a distribution differ by 10% compared to the ones of a Gaussian distribution, the luminosity value can be overestimated or

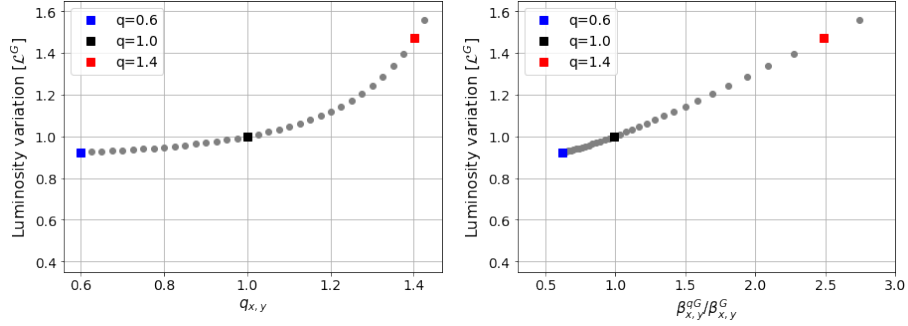


Figure 8.9: Luminosity variation, with respect to the corresponding Gaussian luminosity value ( $\mathcal{L}^G$ ) for the same beam parameters, with the weight of the tails (left) and the  $\beta$  parameter ratio (right) of the transverse distributions, keeping the beam size constant. The blue, black and red points represent the result for a light tailed ( $q < 1$ ), a Gaussian ( $q = 1$ ) and a heavy tailed ( $q > 1$ ) distribution, respectively.

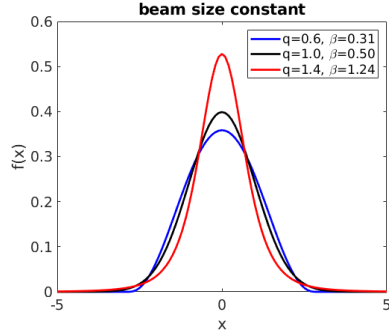


Figure 8.10: The  $q$ -Gaussian density distribution function for a light tailed ( $q < 1$ ), a Gaussian ( $q = 1$ ) and a heavy tailed ( $q > 1$ ) bunch profile, having identical beam sizes.

underestimated by around 5% if instead of a proper fitting function, the Gaussian one is used. It is then clear that, for two beams colliding head-on, the shape of the transverse distributions determines the estimated luminosity.

Keeping now the  $\beta$  parameter constant, in Figure 8.11 the luminosity variation is parameterized with the parameter  $q$  (left) and with the beam size variation- with respect to the Gaussian value (right), in the transverse plane. The blue, black and red points correspond to a light tailed, a Gaussian and a heavy tailed distribution, respectively. The bunch profile shapes for these distributions are plotted in Fig. 8.12, having the same  $\beta$  parameter. As  $q$  increases, the luminosity gets lower with respect to the one for the Gaussian case ( $\mathcal{L}^G$ ). If both the tails and the transverse beam size of a distribution differ by 10% compared to the ones of a Gaussian distribution, the luminosity value can be overestimated or underestimated by around 10% if the Gaussian fitting function is used.

The sensitivity of the luminosity on the distribution as generalised by employing the  $q$ -Gaussian function justifies the need of carefully studying the evolution of distributions in hadron colliders. The extension of this to non-Gaussian distributions as observed in the LHC may shed

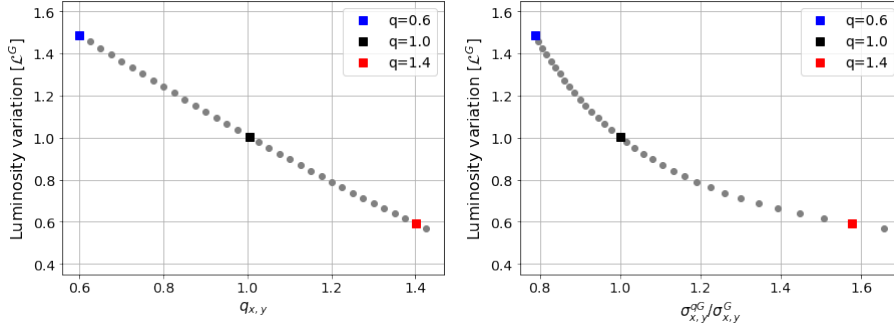


Figure 8.11: Luminosity variation, with respect to the corresponding Gaussian luminosity value ( $\mathcal{L}^G$ ) for the same beam parameters, with the weight of the tails (left) and the beam size ratio (right) of the transverse distributions, keeping the  $\beta$  parameter constant. The blue, black and red points represent the result for a light tailed ( $q < 1$ ), a Gaussian ( $q = 1$ ) and a heavy tailed ( $q > 1$ ) distribution, respectively.

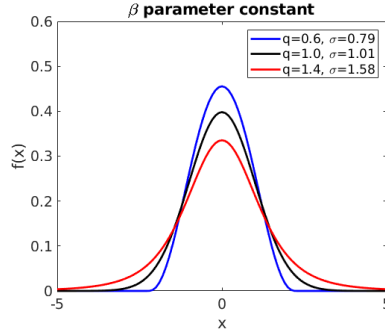


Figure 8.12: The  $q$ -Gaussian density distribution function for a light tailed ( $q < 1$ ), a Gaussian ( $q = 1$ ) and a heavy tailed ( $q > 1$ ) bunch profile, all having the same  $\beta$  parameter.

light to the provenance of the remaining discrepancy between the luminosity model (which is based on IBS calculations assuming Gaussian beam distributions, see Section 8.2) and the measurements.

# IBS Simulations for the LHC

---

For the LHC luminosity studies, a model including the effects of intrabeam scattering (IBS), synchrotron radiation (SR), elastic scattering and luminosity burn-off is used [21]. The model was constructed based on analytical approaches which assume Gaussian beam distributions. A comparison of the bunch characteristics evolution as predicted by this model with the measured ones revealed an extra (on top of the model) transverse emittance blow up in the measured data. One of the attempts to explain this blow up concerns the bunch profiles that appear to have non-Gaussian shapes both at injection and collision energies, i.e. 450 GeV and 6.5 TeV respectively. The aim of this study is to quantify the impact of the distribution's shape on the emittance and luminosity evolution, extending the usual approach of employing the analytical formulas for modeling IBS, which are based on 3D Gaussian beam assumptions [38]. For this, the Monte Carlo multiparticle simulation code for IBS and Radiation Effects (SIRE) [47, 60] is being used. The comparison of the code results with analytical formulas has been studied for the nominal collision energy (7 TeV) for various initial parameters cases [58]. Also, a comparison of LHC data from Run 2 with simulations performed with SIRE is discussed in [59]. In this chapter, a benchmarking of the Bjorken-Mtingwa (B-M) IBS theoretical model with the SIRE code for both injection and collision energies is presented for the nominal Batch Compression Merging and Splitting (BCMS) [10, 11] and the high luminosity (HL-LHC) [3] parameters. For the case of collision energy, an example showing the comparison between experimental data coming from Run 2, the SIRE and the B-M analytical formalism [38], is given.

Apart from the IBS and Synchrotron Radiation (SR) which are the dominant effects for the emittance evolution in the LHC, a combination of other diffusion mechanisms, like the beam-beam effect, electron-cloud, noise (due to the power converters, the transverse damper, the crab cavities, etc.), non-linearities, etc., cause emittance growth and/or particle losses [12]. Despite the fact that these mechanisms are not included in SIRE, it is possible to add empirically (i.e. based on observations) their contribution. Practically, there is the option of adding or complementing the variation of the bunch parameters in time. The simulation studies presented here for the LHC are focused on the  $3\sigma$  range of the particle distributions and therefore, mechanisms like the long-range beam-beam effect and electron-cloud which concern the far tail regime are not taken into account.

## Generation of q-Gaussian random deviates

The input distribution to be tracked in SIRE should be given in action angle variables (see Section 3.4). In order to obtain these variables by generating random deviates for a q-Gaussian distribution which successfully describes the bunch profiles in the LHC, the inverse Abel transform [116] is used. Basically, the inverse Abel transform is a process of calculating a set of radial points from a corresponding set of lateral points. For generating the non-Gaussian distributions

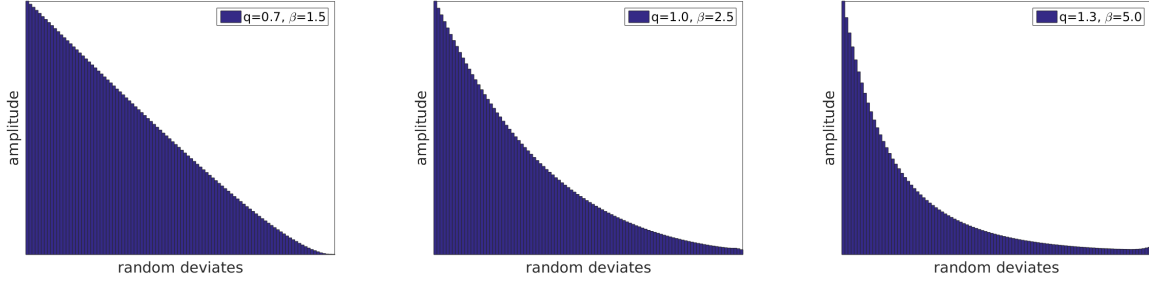


Figure 9.1: Generated  $q$ -Gaussian random deviates to be used as action angle variables, using the Nestor and Olsen method [117] for the inverse Abel transform, for the cases of  $q=0.7$  (left),  $q=1.0$  (center) and  $q=1.3$  (right).

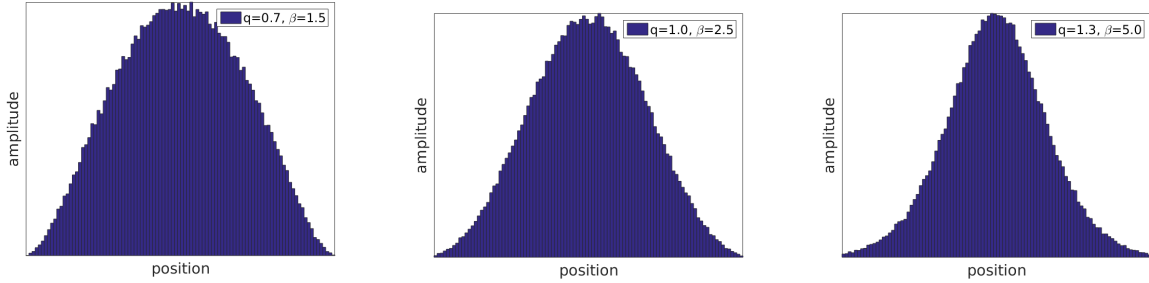


Figure 9.2: Generated  $q$ -Gaussian distributions corresponding to the cases of  $q=0.7$  (left),  $q=1.0$  (center) and  $q=1.3$  (right).

to be tracked in SIRE, the Nestor and Olsen method [117] is used for the inverse Abel transform, because of its simple computational implementation. After defining the required beam parameters and the number of macro-particles, the inverse Abel transform gives the action angle variables for the requested distribution. Some examples of the generated  $q$ -Gaussian random deviates to be used as action angle variables are shown in Fig. 9.1 as histograms, for the cases of having  $q=0.7$ ,  $q=1.0$  and  $q=1.3$ . The corresponding distributions (i.e. in terms of beams sizes) are formed as shown in Fig. 9.2, for the cases of having underpopulated ( $q=0.7$ ), Gaussian ( $q=1.0$ ) and overpopulated ( $q=1.3$ ) tails.

## Reduced lattice

As mentioned earlier, one of the inputs required by SIRE are the optical functions along the ring. As the LHC is a very long accelerator of about 27 km, with a very large number of elements in the sequence (more than 11000), SIRE requires an extremely long computational time to track the distribution for all the elements along the ring. Aiming to reduce the computational time, a study was first performed in order to identify the optimal minimum number of critical IBS kicks around the lattice, without affecting the overall effect. The IBS growth rates were firstly calculated for the full optics of the LHC, using the IBS module of the Methodical Accelerator Design code (MAD-X) [45] which is based on the Bjorken-Mtingwa formalism. Figure 9.3 shows the IBS growth rates in the longitudinal (green), the horizontal (blue) and the vertical (magenta)

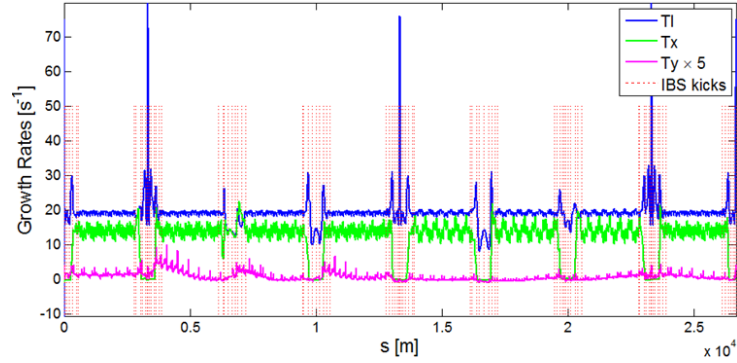


Figure 9.3: The IBS growth rates along the LHC in all three planes: longitudinal (green), the horizontal (blue) and the vertical (magenta). The IBS kicks that are noted with red dashed lines, represent the positions of the 92 elements that compose the reduced lattice.

plane. Taking into account the strong IBS kicks along the ring, various lattices with a reduced number of elements, including the case of the smooth lattice approximation, were tested. Then, using the IBS module of MAD-X, the emittance evolution was calculated for several sets of beam parameters to assure that the choice of the elements is valid both for regimes that the effect is weak and strong. Finally, the optimal lattice chosen consists of only 92 elements whose positions are denoted by red dashed lines in Fig. 9.3.

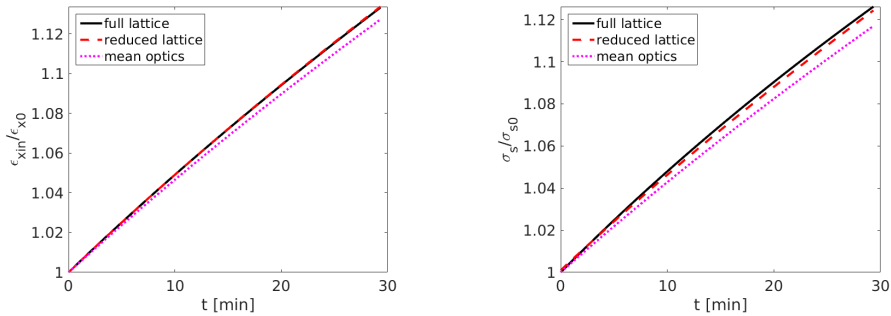


Figure 9.4: The growth of the horizontal emittance (left) and bunch length (right) due to IBS, as computed by MAD-X (Bjorken-Mtingwa analytical formalism), in a time period of 30 min at injection, when considering the full lattice (black solid line), the reduced lattice (red dashed line) and the smooth lattice approximation- mean optics (magenta dotted line).

Figure 9.4 shows the emittance (left) and the bunch length (right) growth during 30 min at injection energy, for the nominal BCMS beams, with initial parameters an emittance and a  $4\sigma$  bunch length that are respectively  $\varepsilon_{x0} = 1.5 [\mu m.rad]$  and  $\sigma_{s0} = 1 [ns]$ , having a bunch population that is  $1.2 \times 10^{11}$ . The black solid line refers to the case of the full lattice, while the red dashed one to the reduced lattice with the 92 elements. The magenta dotted line corresponds to the case of the smooth lattice approximation for which a lattice with a unique element, having the optics that represent in the best possible way the mean optics of the full lattice, is considered. The agreement of the full and the reduced lattice is very good in all planes. On the other hand, by using the smooth lattice approximation the IBS effect is slightly underestimated, in particular,

in the longitudinal plane. In the next, the reduced lattice is used as an input for the SIRE code. After choosing the optimal number of cells and macro-particles, the computational time in the case of the reduced lattice is almost 20 times shorter than the one of the full LHC lattice.

## 9.1 Benchmarking of the B-M IBS theoretical model with SIRE

SIRE has the advantage to accept any type of distribution as an input. If requested, it also gives as output the distribution at any stage of the tracking. In order to benchmark the code with the analytical formulation of B-M for the LHC, a Gaussian distribution was tracked for two sets of bunch parameters which are summarized in Table 9.1 for the injection energy (450 GeV) and in Table 9.2 for the collision energy (6.5 TeV). The first case corresponds to the nominal BCMS [10, 11] LHC beams, having a significantly lower transverse beam size with respect to the nominal production scheme. The second case corresponds to the HL-LHC [3, 118] parameters, for which the bunch population is very high. The input Twiss functions used for the tracking, are the ones that correspond to the optics of the aforementioned reduced lattice.

Table 9.1: Nominal (BCMS) and HL-LHC parameters, at injection energy (450 GeV).

Parameters	Nominal (BCMS)	HL-LHC
$\varepsilon_{x,y}$ [ $\mu\text{m}\cdot\text{rad}$ ]	1.5	2.0
$4\sigma$ bunch length [ns]	1.0	1.2
Bunch population [ $10^{11}$ ]	1.2	2.3

Table 9.2: Nominal (BCMS) and HL-LHC parameters, at collision energy (6.5 TeV).

Parameters	Nominal (BCMS)	HL-LHC
$\varepsilon_{x,y}$ [ $\mu\text{m}\cdot\text{rad}$ ]	2.5	2.5
$4\sigma$ bunch length [ns]	1.0	1.2
Bunch population [ $10^{11}$ ]	1.1	2.2

### LHC at injection (450 GeV)

Table 9.3: IBS growths of the transverse emittances and energy spread during 1 h at injection energy (450 GeV).

IBS growths	Nominal (BCMS)		HL-LHC	
	MADX	SIRE	MADX	SIRE
$d\varepsilon_x/\varepsilon_{x0}$ [%]	24.6	24.1	20.1	19.6
$d\varepsilon_y/\varepsilon_{y0}$ [%]	0.2	0.4	0.2	0.3
$d\sigma_l/\sigma_{l0}$ [%]	21.4	20.8	16.8	16.2

The horizontal emittance (left), the vertical emittance (center) and energy spread (right) evolution after 1 h at the injection energy (450 GeV), where the IBS effect is dominant, are presented in Fig. 9.5 for the nominal BCMS case and in Fig. 9.6 for the HL-LHC parameters. The red and the blue lines correspond to the analytical calculations of the MAD-X [20] IBS

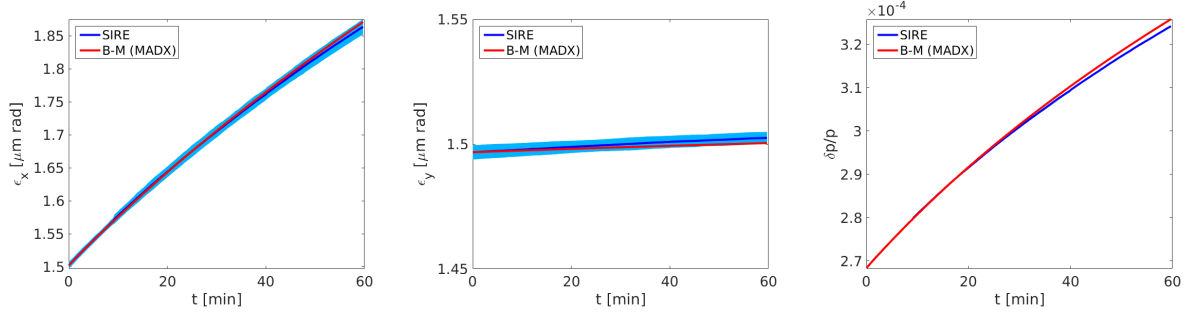


Figure 9.5: The growth of the horizontal (left) and vertical (center) emittance and energy spread (right) due to IBS, in a time period of 1 h at the injection energy of the LHC (450 GeV) for the nominal parameters, as computed by the SIRE code (blue line) and the Bjorken-Mtingwa analytical formalism in MAD-X (red line).

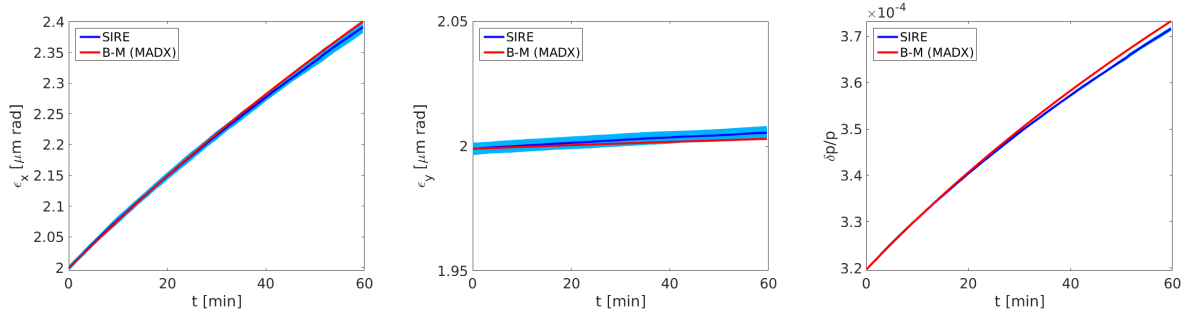


Figure 9.6: The growth of the horizontal (left) and vertical (center) emittance and energy spread (right) due to IBS, in a time period of 1 h at the injection energy of the LHC (450 GeV) for the HL-LHC parameters, as computed by the SIRE (blue line) and the Bjorken-Mtingwa analytical formalism in MAD-X (red line).

routine (based on the B-M formalism) and to the SIRE results, respectively. Due to the fact that in SIRE the generation of the distribution is based on a random number generator, the tracking simulations were performed several times, resulting in the two standard deviation spread that is plotted in light blue. Table 9.3 summarizes the IBS growth of the transverse emittances and energy spread, for the nominal BCMS and HL-LHC parameters, as computed by the SIRE code and the B-M analytical formalism in MAD-X.

In the horizontal and longitudinal plane the IBS effect is dominant, while in the vertical plane, it is minor. Even though the SIRE simulation algorithm and the B-M analytical formalism make use of different approaches to calculate the IBS effect (SIRE uses the classical Rutherford cross section which is closer to the Piwinski formalism), they seem to agree very well during the 1 h time at injection energy. In the longitudinal plane, there is a small difference observed for longer time-spans. Such differences can be explained by the fact that SIRE reshapes the beam distributions after each collisional process, while the B-M IBS formalism assumes Gaussian beam distributions throughout the calculation.

The variation of the initially Gaussian particle distributions within 1 h at injection energy is shown in logarithmic scale in Fig. 9.7 and Fig. 9.8 for the nominal BCMS and the HL-LHC

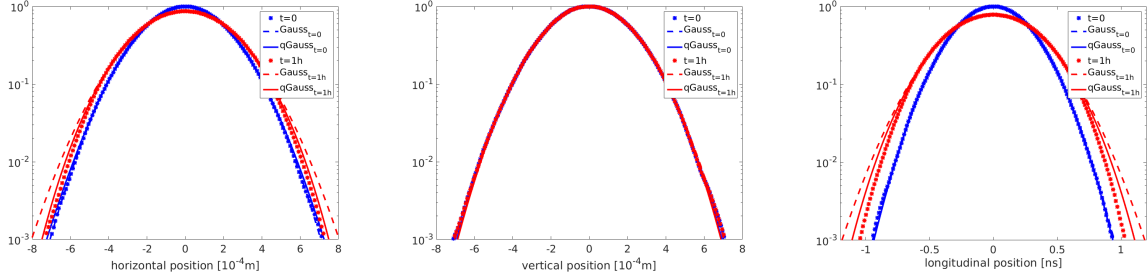


Figure 9.7: The initial and final (after 1 h) distributions in the horizontal (left), vertical (center) and longitudinal (right) plane, for the nominal BCMS bunch parameters at injection energy (450 GeV), are denoted by blue and red stars, respectively. They are fitted with the Gaussian (dashed line) and the q-Gaussian (solid line) functions.

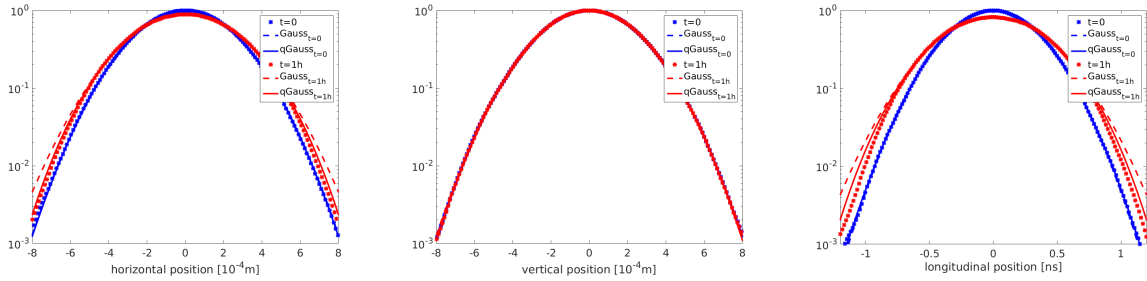


Figure 9.8: The initial and final (after 1 h) distributions in the horizontal (left), vertical (center) and longitudinal (right) plane, for the HL-LHC bunch parameters at injection energy (450 GeV), are denoted by blue and red stars, respectively. They are fitted with the Gaussian (dashed line) and the q-Gaussian (solid line) functions.

case, respectively. The initial and final (after 1 h) distributions in the horizontal (left), vertical (center) and longitudinal (right) plane, are denoted by blue and red stars, respectively. They are fitted with the Gaussian (dashed line) and the q-Gaussian (solid line) functions. The fitting results of the initial and final distributions are presented in Table 9.4 for the nominal BCMS case and in Table 9.5 for the HL-LHC case.

As was expected from the results shown in Fig. 9.5-9.6 concerning the IBS growth, the horizontal and longitudinal rms beam sizes get larger as time evolves, while the vertical one does not change. The vertical distributions remain Gaussian since  $q \approx 1$ . For both the nominal and the HL-LHC case, the  $q$  parameter of the horizontal and longitudinal distributions is decreased. This can be explained by the fact that, due to IBS, the core of the distributions is blown up in such a way that it covers up the initially Gaussian tails of the input distributions. In the longitudinal plane the decrease in  $q$  is more significant for the HL-LHC case. This indicates that the stronger IBS is, the more the core is blown up. Since for a light tailed distribution ( $q < 1$ ) the Gaussian fit overestimates the rms value, the resulted beam sizes are slightly larger than in the case of the q-Gaussian fit. Comparing the root mean square error (RMSE) values of the two fitting functions for the final non-Gaussian bunch profiles shows that the q-Gaussian fit is better.

Table 9.4: Initial and final (after 1 h) fit results for the horizontal, vertical and longitudinal bunch profiles shown in Fig. 9.7, for the nominal BCMS parameters case at injection energy (450 GeV).

Fit Parameters	Horizontal distribution		Vertical distribution		Longitudinal distribution	
	<i>Initial</i>	<i>Final</i>	<i>Initial</i>	<i>Final</i>	<i>Initial</i>	<i>Final</i>
<b>Gaussian</b>						
$\sigma_{rms} \pm 10^{-3}$	0.19 [mm]	0.22 [mm]	0.19 [mm]	0.19 [mm]	0.25 [ns]	0.33 [ns]
$RMSE [10^{-3}]$	1	14	1	1	1	10
<b>q-Gaussian</b>						
$\sigma_{rms} \pm 10^{-3}$	0.19 [mm]	0.21 [mm]	0.19 [mm]	0.19 [mm]	0.25 [ns]	0.32 [ns]
$q \pm dq$	$1.024 \pm 0.003$	$0.893 \pm 0.002$	$0.970 \pm 0.007$	$0.967 \pm 0.006$	$0.992 \pm 0.002$	$0.941 \pm 0.001$
$RMSE [10^{-3}]$	1	1	1	1	1	6

Table 9.5: Initial and final (after 1 h) fitting results for the horizontal, vertical and longitudinal bunch profiles shown in Fig. 9.8, for the HL-LHC parameters case at injection energy (450 GeV).

Fit Parameters	Horizontal distribution		Vertical distribution		Longitudinal distribution	
	<i>Initial</i>	<i>Final</i>	<i>Initial</i>	<i>Final</i>	<i>Initial</i>	<i>Final</i>
<b>Gaussian</b>						
$\sigma_{rms} \pm 10^{-3}$	0.22 [mm]	0.25 [mm]	0.22 [mm]	0.22 [mm]	0.30 [ns]	0.37 [ns]
$RMSE [10^{-3}]$	1	14	1	1	3	13
<b>q-Gaussian</b>						
$\sigma_{rms} \pm 10^{-3}$	0.22 [mm]	0.24 [mm]	0.22 [mm]	0.22 [mm]	0.30 [ns]	0.36 [ns]
$q \pm dq$	$0.992 \pm 0.003$	$0.891 \pm 0.004$	$0.995 \pm 0.003$	$0.987 \pm 0.003$	$1.019 \pm 0.005$	$0.885 \pm 0.001$
$RMSE [10^{-3}]$	1	1	1	1	3	4

## LHC at collision (6.5 TeV)

Since at collision energy IBS becomes weaker and SR starts playing an important role, it is the interplay between these effects that determines the evolution of the bunch characteristics. In this respect, for the benchmarking of the B-M IBS theoretical model with SIRE at collision energy, apart from the IBS, the radiation effects (SR and QE) are also taken into account. It should be mentioned that for the results presented in the following plots the intensity is assumed to be constant.

Figure 9.9 shows the horizontal emittance (left), the vertical emittance (center) and energy spread (right) evolution after 10 h at collision energy for the nominal BCMS case, while Fig. 9.10 shows the evolutions for the HL-LHC parameters. The red and the blue lines correspond to the analytical calculations of the MAD-X [20] IBS routine (based on the B-M formalism) and to the SIRE results, respectively. The two standard deviation spread for the simulation results are plotted in light blue. Table 9.6 summarizes the variation of the transverse emittances and energy spread during 10 h at the collision energy of the LHC, for the nominal BCMS and HL-LHC parameters, as computed by the SIRE code and the B-M analytical formalism in MAD-X.

Table 9.6: Variation of the transverse emittances and energy spread during 10 h at collision energy.

IBS growths	Nominal (BCMS)		HL-LHC	
	<i>MADX</i>	<i>SIRE</i>	<i>MADX</i>	<i>SIRE</i>
$d\varepsilon_x/\varepsilon_{x0}$ [%]	-0.1	-1.4	7.4	5.0
$d\varepsilon_y/\varepsilon_{y0}$ [%]	-26.2	-26.1	-31.4	-31.2
$d\sigma_l/\sigma_{l0}$ [%]	-0.1	-2.6	-12.6	-14.7

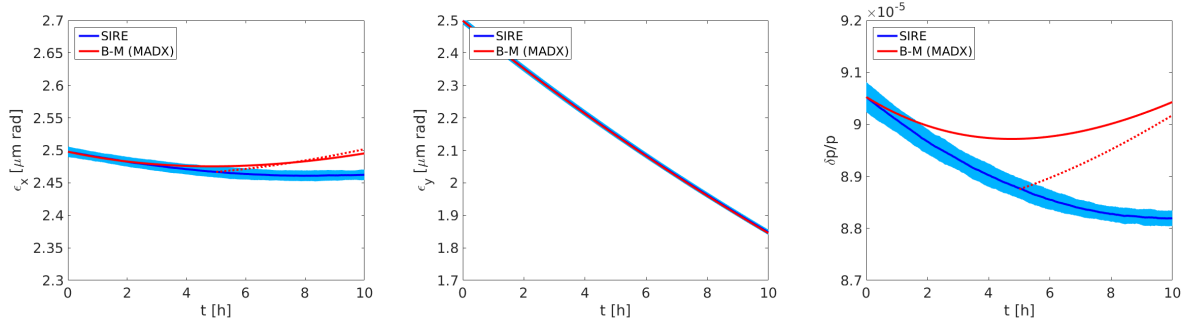


Figure 9.9: The evolution of the horizontal (left) and vertical (center) emittance and energy spread (right) due to IBS and radiation effects (SR and QE), in a time period of 10 h at the collision energy of the LHC (6.5 TeV) for the nominal BCMS parameters, as computed by the SIRE code (blue line) and the Bjorken-Mtingwa analytical formalism in MAD-X (red line).

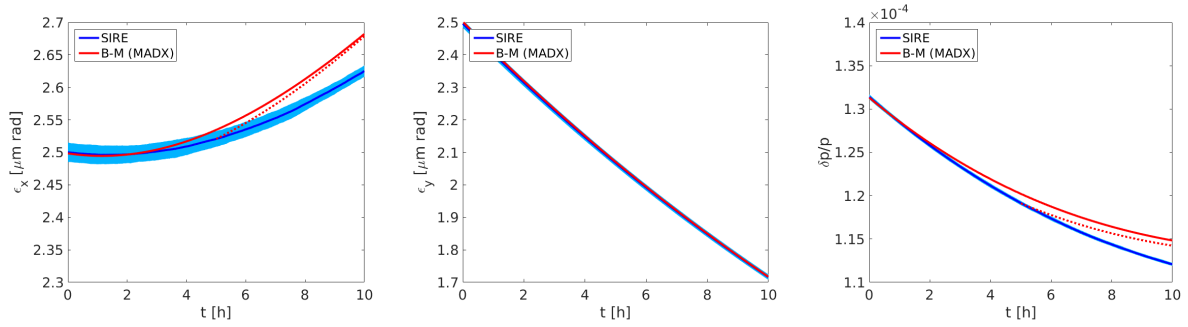


Figure 9.10: The evolution of the horizontal (left) and vertical (center) emittance and energy spread (right) due to IBS and radiation effects (SR and QE), in a time period of 10 h at the collision energy of the LHC (7 TeV) for the HL-LHC parameters, as computed by the SIRE (blue line) and the Bjorken-Mtingwa analytical formalism in MAD-X (red line).

After a few hours at collisions, the B-M analytical formalism and the simulations start differentiating. In order to understand whether these differences are explained by the fact that SIRE reshapes the beam distributions after each collisional process and the B-M IBS formalism assumes always Gaussian beam distributions, the bunch parameters given by SIRE at 5 h are used as input for the IBS and SR calculations in MAD-X (Gaussian bunches). The red dotted lines in Fig. 9.9 and Fig. 9.10 represent the results of these tests. Even if giving as input to MAD-X exactly the same bunch parameters as in SIRE, there is clear divergence of the MAD-X results (red dotted lines) with SIRE right after the 5 h at collisions. This divergence is much larger than the one observed during the first hours at collisions. After 5 h collisions the beam in SIRE has been reshaped enough so that IBS and radiation processes act differently as compared to Gaussian MAD-X distributions. Consequently, the differences observed between the B-M analytical formalism and the simulations are expected because MAD-X assumes always Gaussian distribution, in contrast to SIRE that takes into account the variation of the bunch shape throughout the calculation.

Due to the fact that the IBS effect is minor in the vertical plane, the strong SR damping mechanism leads to a clear reduction of the vertical emittance. However, the variation of the

horizontal emittance and energy spread is determined by the interplay of IBS growth with SR damping. For the nominal BCMS parameters, these variations are very small after 10 h at collision energy (Table 9.6). For the HL-LHC case, having the same initial horizontal emittance but double bunch population compared to the nominal BCMS parameters (Table 9.2), the IBS effect prevails over SR in the horizontal plane after almost 3 h (Fig. 9.10 (left)). As can be seen in Fig. 9.10 (right) this is not the case for the longitudinal plane, for which the initial bunch length of 1.2 ns compared to the 1 ns in the nominal case, renders IBS weaker than SR and, results in the decrease of the energy spread.

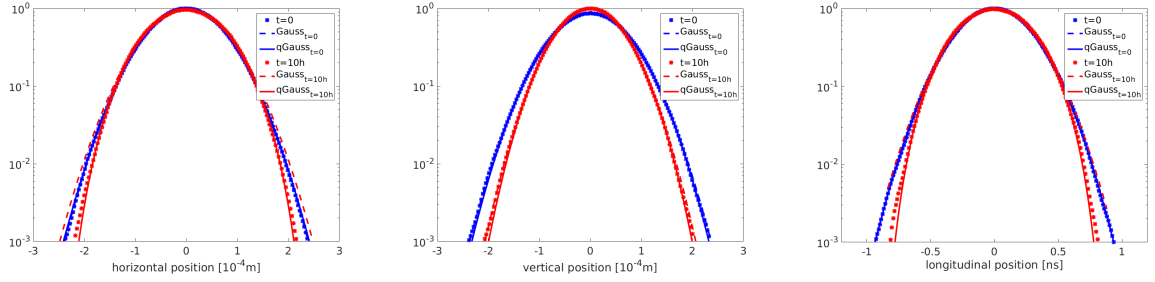


Figure 9.11: The initial and final (after 10 h) distributions in the horizontal (left), vertical (center) and longitudinal (right) plane, for the nominal BCMS bunch parameters at collision energy (6.5 TeV), are denoted by blue and red stars, respectively. They are fitted with the Gaussian (dashed line) and the q-Gaussian (solid line) functions.

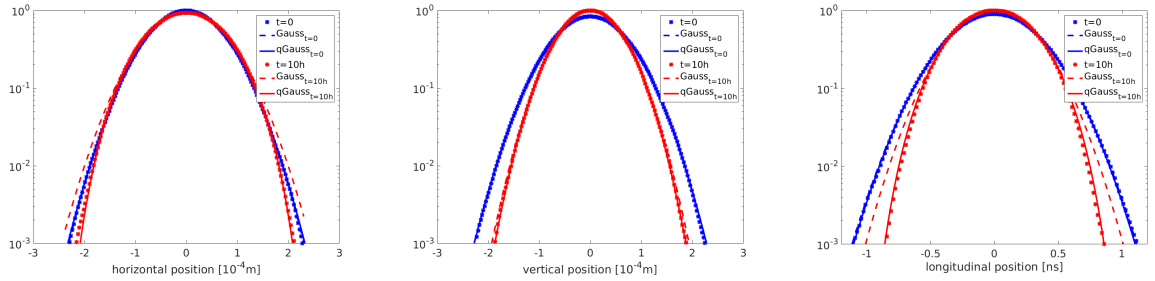


Figure 9.12: The initial and final (after 10 h) distributions in the horizontal (left), vertical (center) and longitudinal (right) plane, for the HL-LHC bunch parameters at collision energy (7 TeV), are denoted by blue and red stars, respectively. They are fitted with the Gaussian (dashed line) and the q-Gaussian (solid line) functions.

The evolution of the initially Gaussian (in all planes) particle distributions within 10 h at collision energy is shown in logarithmic scale in Fig. 9.11 and Fig. 9.12 for the nominal BCMS and the HL-LHC case, respectively. The initial and final (after 10 h) distributions in the horizontal (left), vertical (center) and longitudinal (right) plane, are denoted by blue and red stars, respectively. They are fitted with the Gaussian (dashed line) and the q-Gaussian (solid line) functions. The fitting results of the initial and final distributions are presented in Table 9.7 for the nominal BCMS case and in Table 9.8 for the HL-LHC case. The RMSE values of the two fitting functions show that when the final bunch profiles are strongly non-Gaussian, the q-Gaussian fitting results should be considered. In this respect, the evolution of the particle distributions in all planes for

Table 9.7: Initial and final (after 10 h) fit results for the horizontal, vertical and longitudinal bunch profiles shown in Fig. 9.11, for the nominal BCMS parameters case at collision energy (6.5 TeV).

Fit Parameters	Horizontal distribution		Vertical distribution		Longitudinal distribution	
	Initial	Final	Initial	Final	Initial	Final
<b>Gaussian</b>						
$\sigma_{rms} \pm 10^{-3}$	0.064 [mm]	0.067 [mm]	0.064 [mm]	0.056 [mm]	0.25 [ns]	0.26 [ns]
RMSE [ $10^{-3}$ ]	1	25	1	1	1	30
<b>q-Gaussian</b>						
$\sigma_{rms} \pm 10^{-3}$	0.064 [mm]	0.064 [mm]	0.064 [mm]	0.055 [mm]	0.25 [ns]	0.24 [ns]
$q \pm dq$	$1.004 \pm 0.003$	$0.856 \pm 0.005$	$0.982 \pm 0.004$	$0.971 \pm 0.004$	$1.007 \pm 0.004$	$0.830 \pm 0.006$
RMSE [ $10^{-3}$ ]	1	1	1	1	1	1

Table 9.8: Initial and final (after 10 h) fitting results for the horizontal, vertical and longitudinal bunch profiles shown in Fig. 9.12, for the HL-LHC parameters case at collision energy (7 TeV).

Fit Parameters	Horizontal distribution		Vertical distribution		Longitudinal distribution	
	Initial	Final	Initial	Final	Initial	Final
<b>Gaussian</b>						
$\sigma_{rms} \pm 10^{-3}$	0.062 [mm]	0.067 [mm]	0.062 [mm]	0.052 [mm]	0.30 [ns]	0.28 [ns]
RMSE [ $10^{-3}$ ]	1	27	2	2	2	17
<b>q-Gaussian</b>						
$\sigma_{rms} \pm 10^{-3}$	0.062 [mm]	0.063 [mm]	0.062 [mm]	0.052 [mm]	0.30 [ns]	0.27 [ns]
$q \pm dq$	$1.005 \pm 0.004$	$0.852 \pm 0.004$	$0.991 \pm 0.005$	$0.977 \pm 0.005$	$0.990 \pm 0.003$	$0.825 \pm 0.001$
RMSE [ $10^{-3}$ ]	1	1	1	1	1	1

the nominal BCMS and HL-LHC cases is discussed based on the q-Gaussian results.

The horizontal beam sizes do not change after 10 h at collision energy because the blow up caused by IBS is balanced out by the SR damping. However, there is a transformation of the horizontal distributions' shape for which the tails become less populated ( $q < 1$ ). In the longitudinal plane both the beam size and the q parameter are reduced, meaning that SR prevails over IBS and the core is blown up due to IBS- giving underpopulated tails. In the vertical plane, the dominant SR damping results in a smaller beam size without changing much the formation of the tails, so the distribution remains Gaussian.

## 9.2 Comparison with experimental data from Run 2

The longitudinal bunch manipulations performed during the Ramp to avoid instabilities due to the loss of Landau damping [90], produce bunches that arrive at collision energy with a clearly non-Gaussian longitudinal shape. By assuming that these profiles are Gaussian may lead in underestimating or overestimating the actual bunch length. In this respect, these profiles are fitted using the q-Gaussian function. An example showing the evolution of the  $q$  parameter for a train of longitudinal bunches during 11.5 h at stable beams (6.5 TeV) in the LHC is presented in Fig. 9.13. It is clear that with such q parameter values, corresponding to non-Gaussian tails, the rms beam size cannot be accurately estimated by using the Gaussian function. The increase of the  $q$  parameter means that the longitudinal distributions with the underpopulated tails ( $q < 1$ ) at the start of stable beams, become more Gaussian ( $q \rightarrow 1$ ) as time evolves. This is a general statement that can be made for the longitudinal distribution observed at the collision energy of the LHC. The evolution of the longitudinal particle distribution of a single bunch that is picked

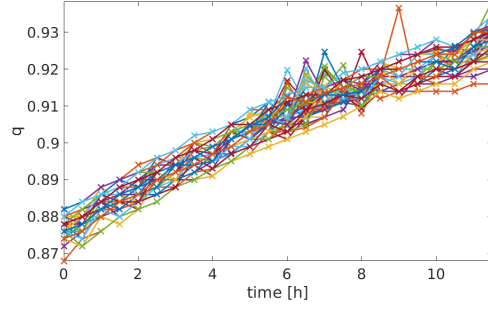


Figure 9.13: The evolution of the  $q$  parameter during 11.5 h at stable beams (6.5 TeV), for a train of bunches in the longitudinal plane.

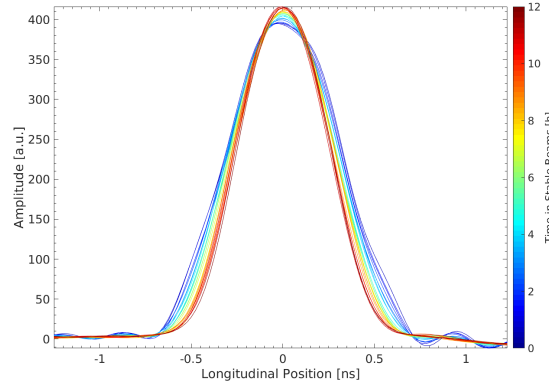


Figure 9.14: The evolution of a longitudinal bunch profile during 11.5 h at stable beams (6.5 TeV).

out of the train of bunches is shown in Fig. 9.14 for the time period of 11.5 h. The initial bunch profile (plotted in blue) is fitted with the Gaussian and the  $q$ -Gaussian functions that give different rms beam sizes because of the dependence of the standard deviation on the  $q$  parameter (Eq. (7.8)). The fitting results are used to generate a Gaussian and a  $q$ -Gaussian distribution to be tracked in SIRE in order to compare the experimental observations with the results of the code.

Table 9.9: Fitting results for the initial (at the start of collisions) and the final (after 11.5 h) longitudinal bunch distribution shown in Fig. 9.15, as was observed in the LHC and as was calculated by the SIRE code.

Fit Parameters		Initial (t=0)		Final (t=11.5 h)	
		DATA	SIRE	DATA	SIRE
Gaussian	$\sigma_{rms} \pm d\sigma_{rms}$ [ns]	$0.299 \pm 0.003$	$0.297 \pm 0.002$	$0.233 \pm 0.002$	$0.237 \pm 0.002$
	RMSE [ $10^{-3}$ ]	22	19	18	20
q-Gaussian	$\sigma_{rms} \pm d\sigma_{rms}$ [ns]	$0.286 \pm 0.004$	$0.290 \pm 0.001$	$0.227 \pm 0.002$	$0.235 \pm 0.001$
	$q \pm dq$	$0.88 \pm 0.03$	$0.85 \pm 0.01$	$0.93 \pm 0.03$	$0.86 \pm 0.01$
	RMSE [ $10^{-3}$ ]	10	3	10	4

In Fig. 9.15, the initial (at the start of collisions) and the final (after 11.5 h) longitudinal bunch profiles, as observed in the LHC (left) and as calculated by the SIRE (right) for an initially

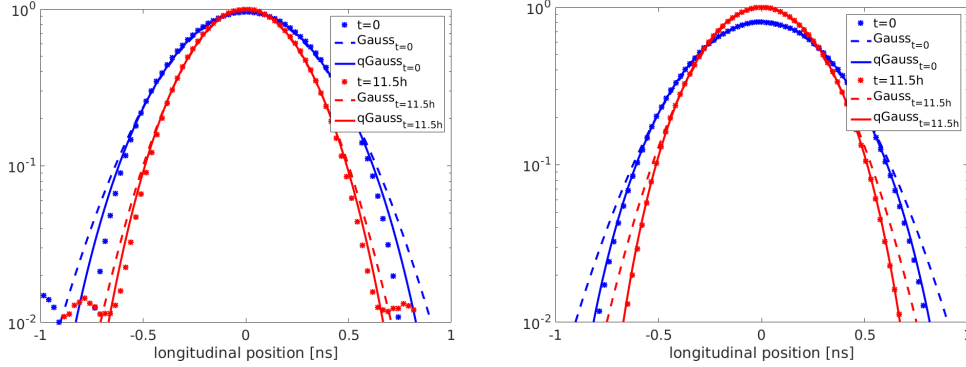


Figure 9.15: The initial (at the start of collisions) and the final (after 11.5 h) longitudinal bunch profiles as observed in the LHC (left) and as calculated by the SIRE (right), in logarithmic scale, are denoted by blue and red stars, respectively. They are fitted with the Gaussian (dashed line) and the q-Gaussian (solid line) functions.

q-Gaussian simulated profile, are denoted by blue and red stars, respectively. They are plotted in logarithmic scale and they are fitted with the Gaussian (dashed line) and the q-Gaussian (solid line) functions. The reduction of the bunch population with time and the extra (on top of IBS) transverse emittance blow up observed in the machine, are taken into account for the simulation. The transverse distributions are assumed to be Gaussian, since at collisions the shape of their tails is not clear due to diffraction. The fitting results are presented in Table 9.9. Even if there seems to be no change at the tails of the simulated distribution, in reality the profiles become more Gaussian. Within 11.5 h at stable beams, the rms beam size of the measured bunch profile and of the corresponding tracked distribution is reduced by 21% and by 19%, respectively. This shows a very good agreement between the experimental data and the simulations performed with SIRE.

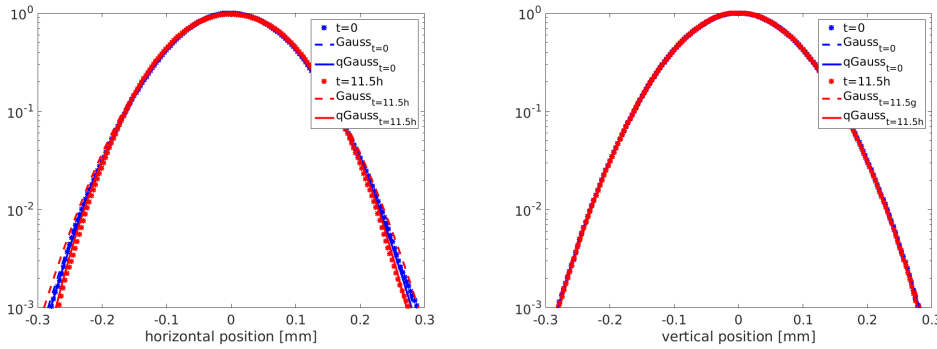


Figure 9.16: The initial (at the start of collisions) and the final (after 11.5 h) horizontal (left) and vertical (right) bunch profiles as calculated by the SIRE, in logarithmic scale, are denoted by blue and red stars, respectively. They are fitted with the Gaussian (dashed line) and the q-Gaussian (solid line) functions.

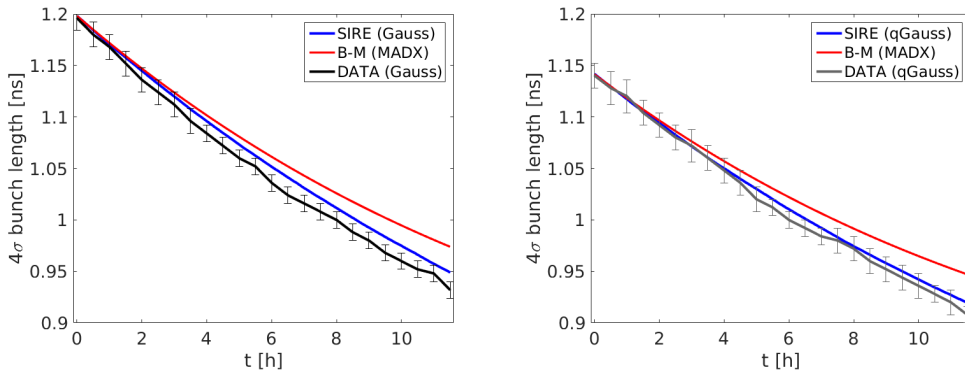
Figure 9.16 shows in logarithmic scale the initial (blue stars) and the final (red stars) horizontal (left) and vertical (right) bunch profiles as calculated by SIRE, fitted with the Gaussian

Table 9.10: Fitting results for the initial (at the start of collisions) and the final (after 11.5 h) transverse bunch distributions shown in Fig. 9.16, as was calculated using the SIRE code.

Fit Parameters		Horizontal distribution		Vertical distribution	
		Initial	Final	Initial	Final
q-Gaussian	$\sigma_{rms} \pm 10^{-4}$ [mm]	0.076	0.076	0.076	0.076
	$q \pm dq$	$0.990 \pm 0.004$	$0.893 \pm 0.005$	$0.992 \pm 0.003$	$0.983 \pm 0.003$
	RMSE [ $10^{-3}$ ]	3	3	3	3

(dashed line) and the q-Gaussian (solid line) functions. As can be seen in Table 9.10, the simulations showed no change in the transverse beam sizes and that is because the extra (on top of IBS) transverse emittance blow up is included. The effect of IBS together with the extra blow up assumed, widens the core of the horizontal bunch in such a way that the  $q$  parameter is decreased by around 10% within these 11.5 h. Since IBS is negligible in the vertical plane, the fact that the vertical bunch profile remains Gaussian indicates that the interplay between the SR damping and the extra blow up do not change the tails of the distribution.

The  $4\sigma$ -bunch length evolution when assuming Gaussian (left) and q-Gaussian (right) initial distributions is shown in Figure 9.17. The blue line corresponds to the SIRE calculations and the red line to the results given by the IBS module of MAD-X [45] which is based on the analytical formulation of B-M and always assumes Gaussian distributions. The bunch length evolution, together with the two standard deviation error-bars, when fitting the data with the Gaussian and the q-Gaussian functions is represented by a black and a grey line, respectively. The bunch length values differ for the two distribution functions used due to the fact that, for a light tailed distribution the rms value is overestimated by fitting a Gaussian. When assuming a Gaussian distribution, the bunch length evolution calculated by the code is close to the measured data. For the q-Gaussian case the agreement between data and simulations is excellent. In agreement with the results presented in the previous section, the divergence between the SIRE and the MAD-X for longer time-spans is something to be expected since the distribution shape in SIRE is updated, while in MAD-X it is not.


 Figure 9.17: The bunch length ( $4\sigma$ ) evolution during several hours in stable beams, as computed by the SIRE code (blue), the B-M analytical formalism (red) and as measured by the longitudinal profile monitors when assuming a Gaussian (left) and a q-Gaussian (right) distribution.

At collisions, the divergence between the luminosity model and the measured luminosity by

the experiments becomes more pronounced as time evolves [109] (see Chapter 8). Actually, the predicted luminosity by the model is always larger compared to the measured one by the end of collisions. As calculated by SIRE, the weight of the horizontal bunch profile tails is decreased in time (see Table 9.10) and as explained in Chapter 8, for lighter tails and a constant beam size, the luminosity is expected to become lower. It is then clear that by taking into account the luminosity change due to the variation of the transverse distribution tails, the model predictions can be significantly improved.

# Conclusions

---

This thesis elaborated the impact of the Intra Beam Scattering (IBS) effect on the bunch characteristics, for the case of lepton and hadron machines. The first part of this thesis was dedicated to a  $e^+/e^-$  linear collider that is under study at CERN, the Compact Linear Collider (CLIC), focusing on the optimization of its Damping Rings (DRs). In the second part, observations of the Large Hadron Collider (LHC) beam distributions, along with their impact on the evolution of bunch characteristics and luminosity, are presented. Based on simulations, the evolution of bunch parameters for the nominal LHC and the High Luminosity LHC (HL-LHC) were studied. For both the CLIC DRs and the LHC, the important role of the IBS effect that limits the performance of a collider, is discussed. The interplay between IBS and radiation effects is studied, using the existing IBE theoretical models and a Monte-Carlo multi-particle tracking code, called SIRE (Software for IBS and Radiation Effects).

The CLIC project aims to explore the Tera scale particle physics regime, for an optimized 3 TeV center of mass energy. Targeting a luminosity of  $10^{34} \text{ cm}^{-2}\text{s}^{-1}$ , which needs to be produced already at the extraction of the DRs, high intensity bunches with ultra low emittances are required. The DRs have to produce the beams with these specifications. One of the main challenges for the beams with ultra-low emittances and high bunch charge is the strong IBS effect which limits the performance of the DR. This thesis elaborated the optimization of the main CLIC DRs, in the strong IBS regime.

In particular, an analytical parametrization of the TME cell has been derived for the case of using dipoles with longitudinally varying magnetic fields. The emittances reached for longitudinally variable bends are lower compared to the ones in the case of using uniform dipoles. Among the non-uniform dipoles studied, it is found that the one having a hyperbolic field profile gives the largest emittance reductions. Based on these analytical calculations, the magnetic design of such a dipole was studied in CIEMAT. It reaches the 2.3 T (using permanent magnets) at the highest field region and it gives very good results in terms of emittance reduction. This innovative dipole design could be applied in any low emittance ring which targets lower emittances.

For the optimization of the DRs Theoretical Minimum Emittance (TME) cells located at the arcs, based on the analytical studies, the numerical simulation code MAD-X is used in order to define the appropriate initial conditions for matching the lattice and for finding optimal regions of operation for the best performance. By replacing the uniform dipoles of the existing DRs arcs with longitudinally variable bends, emittances much lower than the DR requirements could be achieved and this allowed to remove some TME cells, resulting in a shorter ring. Moreover, the high field wigglers used at the FODO cells of the DRs straight sections lowered the number of cells needed to achieve the required design parameters. The ultimate purpose of using damping wigglers is to further reduce damping times and thereby maintain low emittances by reducing the impact of IBS, but also of various collective effects. The use of super-conducting technology

is mandatory in order to have a high wiggler field and a relatively short period for obtaining low emittances and fast damping time. By targeting higher wiggler fields not only the emittance but also the IBS effect are reduced. Overall, the optimization of the TME cells and of the wiggler FODO cells made it possible to reduce the circumference of the DRs by around 13%. With the alternative DR design proposed, apart from achieving all target parameters, for a mitigated IBS effect, it is possible to allow significant margin for the 500 nm target, for an eventual increase of the required bunch population, as lately proposed due to the CLIC re-baselining [80]. The benchmarking of the B-M IBS theoretical model with the results obtained from a multi-particle tracking code called SIRE, was also presented.

IBS plays an important role also for high intensity hadron machines, like the LHC. On top of IBS, radiation effects and a combination of other diffusion mechanisms (such as the beam-beam effect, electron-cloud, noise, etc.), an extra transverse emittance blow up which leads to luminosity degradation, is observed in the LHC. One of the attempts to explain this blow up concerns the studies of the particle distributions, along the LHC energy cycle, which appear to have non-Gaussian shapes. Examples of measured LHC bunch profiles in both the transverse and the longitudinal plane were given. By assuming that a particle distribution is Gaussian when this is not the case, not only the rms beam size may be underestimated or overestimated, but also its impact on performance parameters, such as the luminosity. The use of appropriate fitting functions for the LHC beam profiles is underlined. The q-Gaussian distribution function is employed in order to describe the actual beam profile shapes observed, both for the light tail and the heavy tail regime. It is proven that the use of this function allows to obtain more accurate beam size estimations.

The impact of non-Gaussian distribution shapes on the estimation of the beam size and of the luminosity is discussed. The luminosity integrals are solved for q-Gaussian density distributions in the transverse plane. By comparing the resulted luminosity equation with the standard luminosity formula for Gaussian beams, the significance of the tail population contribution to luminosity is established. The sensitivity of the luminosity on the distribution as generalised by employing the q-Gaussian function justifies the need of carefully studying the evolution of distributions in hadron colliders. One of the next steps is to improve the luminosity model, that is currently based on Gaussian distributions, by taking into account the actual shape of the bunch profiles. In this way, it is possible to get more accurate luminosity predictions. Already, for the operational scenario of the High Luminosity LHC upgrade, a non-Gaussian bunch length estimation is being considered.

In order to understand the evolution of the bunch characteristics, based on the bunch profile observations, it is important to study the interplay between IBS and radiation effects during the full LHC cycle. At the LHC injection energy (450 GeV), in the horizontal and longitudinal plane the IBS effect is dominant, while in the vertical plane, it is minor. At the LHC collision energy (6.5 TeV) where IBS becomes weaker and synchrotron radiation starts playing an important role, it is the interplay between these effects that determines the evolution of the bunch characteristics. Based on the transverse and longitudinal bunch profile measurements, it has been observed that the particle distributions in the LHC, both at collision and injection energies, appear to have shapes that differ from the ones of a normal distribution. In many cases the bunch profiles appear to be non-Gaussian during the whole injection plateau. At collisions, in many cases the bunch

profiles appear to have non-Gaussian tails. The bunches that are blown up longitudinally during the energy ramp arrive at the start of collisions with a non-Gaussian shape. In general, it is observed that along the LHC energy cycle, in both the longitudinal and the transverse plane, the particle distributions become more Gaussian in time.

The way IBS and radiation effects act depends on the shape of the profiles. In order to quantify the impact of the distribution's shape on the emittance evolution, SIRE is used for simulations. The benchmarking of the B-M analytical formalism with SIRE showed a very good agreement for the first couple of hours at injection and collision energies of the LHC, even if they make use of different approaches to calculate the IBS effect. Due to the fact that in SIRE the particle distributions are updated, while MAD-X always assumes Gaussian distributions, the divergence between the two approaches becomes more pronounced as time evolves. The results obtained from the simulations encourage the idea of using the code to track distributions coming from experimental data, in order to study the impact of the distribution's shape on the evolution of the bunch characteristics. The agreement between data and simulations is excellent, specially in the case of using the q-Gaussian fitting function for the measured and simulated bunch profiles. This is a remarkable result, considering that no assumptions are being made in the simulations apart from using identical initial conditions with respect to the experimental ones. Finally, the fact that SIRE takes into account the change of the particle distribution showed that it is a very useful tool for estimating the actual bunch parameters evolution in the machine.



# Appendices

# The Bjorken-Mtingwa formalism auxiliary matrices

---

For  $i = p, x, y$  being the index that respectively corresponds to the longitudinal and transverse planes, the auxiliary matrices for the B-M growth times (see Eq. 3.9) are given by:

$$L = L^{(p)} + L^{(x)} + L^{(y)}, \quad (\text{A.1})$$

$$L^{(p)} = \frac{\gamma^2}{\sigma_p^2} \begin{pmatrix} 0 & 0 & 0 \\ 0 & 1 & 0 \\ 0 & 0 & 0 \end{pmatrix}, \quad (\text{A.2})$$

$$L^{(x)} = \frac{\beta_x}{\varepsilon_x} \begin{pmatrix} 1 & -\gamma\phi_x & 0 \\ -\gamma\phi_x & \gamma^2\mathcal{H}_x/\beta_x & 0 \\ 0 & 0 & 0 \end{pmatrix}, \quad (\text{A.3})$$

$$L^{(y)} = \frac{\beta_y}{\varepsilon_y} \begin{pmatrix} 0 & 0 & 0 \\ 0 & \gamma^2\mathcal{H}_y/\beta_y & -\gamma\phi_y \\ 1 & -\gamma\phi_y & 1 \end{pmatrix}, \quad (\text{A.4})$$

where,

$$\phi_{x,y} \equiv \eta'_{x,y} - \frac{\beta'_{x,y}\eta_{x,y}}{2\beta_{x,y}}, \quad (\text{A.5})$$

and

$$\mathcal{H}_{x,y} = \frac{1}{\beta_{x,y}} \left[ \eta_{x,y}^2 + \left( \beta_{x,y}\eta'_{x,y} - \frac{1}{2}\beta'_{x,y}\eta_{x,y} \right)^2 \right]. \quad (\text{A.6})$$

# The integrals to calculate the emittance of a variable bend

---

The integrals to calculate the emittance given in Eq. (4.17) for a variable bend described by two different bending radii functions along its length, are:

$$\begin{aligned}
 I_1 &= \int_0^{L_1} \frac{\theta_1^2}{|\rho_1(s)|^3} ds, \quad I_2 = \int_{L_1}^{L_1+L_2} \frac{(\theta_2 + \theta_{L_1})^2}{|\rho_2(s)|^3} ds, \quad I_3 = \int_0^{L_1} \frac{1}{|\rho_1(s)|^3} ds, \quad I_4 = \int_{L_1}^{L_1+L_2} \frac{1}{|\rho_2(s)|^3} ds, \\
 I_5 &= \int_0^{L_1} 2 \frac{-s\theta_1 + \tilde{\theta}_1}{|\rho_1(s)|^3} ds, \quad I_6 = \int_{L_1}^{L_1+L_2} 2 \frac{-s\theta_2 + \tilde{\theta}_2 - L_1\theta_{L_1} + \tilde{\theta}_{L_1}}{|\rho_2(s)|^3} ds, \quad I_7 = \int_0^{L_1} \frac{(-s\theta_1 + \tilde{\theta}_1)^2}{|\rho_1(s)|^3} ds \quad \text{and} \\
 I_8 &= \int_{L_1}^{L_1+L_2} \frac{(-s\theta_2 + \tilde{\theta}_2 - L_1\theta_{L_1} + \tilde{\theta}_{L_1})^2}{|\rho_2(s)|^3} ds.
 \end{aligned} \tag{B.1}$$

where  $\theta_{L_1} = \theta(s = L_1)$  and  $\tilde{\theta}_{L_1} = \tilde{\theta}(s = L_1)$ .

# The emittance reduction factor as a function of $\rho$ and $\lambda$ for the step and the trapezium profile

As discussed in section 4.2, the emittance reduction factors for the step and the trapezium variable bend profiles depend only on  $\rho$  and  $\lambda$  and their full expressions are given by:

$$F_{TME}^{step} = 2(\lambda + \tilde{\rho})^3(1 + \tilde{\rho}^2) \sqrt{\frac{1 + \tilde{\rho}^3}{\lambda_1 \tilde{\rho}^4 + \lambda_2 \tilde{\rho}^5 + \lambda_3 \tilde{\rho}^7 + \lambda_4 \tilde{\rho}^8 + \lambda_5 \tilde{\rho}^9 + \lambda_6 \tilde{\rho}^{10} + \lambda_7(1 + 9\tilde{\rho}^3 + 18\tilde{\rho}^6) + \lambda_8(\lambda_9 \tilde{\rho}^{11} + \lambda_{10} \tilde{\rho}^{12} + \tilde{\rho}^{13})}},$$

where  $\lambda_1 = 4\lambda^4(5 + 18\lambda)$ ,  $\lambda_2 = \lambda^2(9 + 45\lambda + 64\lambda^2)$ ,  $\lambda_3 = 12\lambda^4(5 + 21\lambda)$ ,  $\lambda_4 = \lambda^2(31 + 210\lambda + 399\lambda^2)$ ,  $\lambda_5 = \lambda(27 + 155\lambda + 240\lambda^2)$ ,  $\lambda_6 = 3(3 + 15\lambda + 20\lambda^2)$ ,  $\lambda_7 = 4\lambda^6$ ,  $\lambda_8 = (4 + 15\lambda + 15\lambda^2)$ ,  $\lambda_9 = 3\lambda_7/(4\lambda^4)$  and  $\lambda_{10} = \lambda_9/\lambda$ .

$$F_{TME}^{trapezium} = \frac{4\sqrt{2}r_1(r_2\lambda + \tilde{\rho}\ln\tilde{\rho})^3\sqrt{w_2/w_3}}{w_1},$$

where  $r_1 = \tilde{\rho} + 1$ ,  $r_2 = \tilde{\rho} - 1$  and:

$$w_1 = 2r_2^3(2 + 3r_1\tilde{\rho})\lambda^2 - 6r_2\tilde{\rho}^2(r_1r_2 - 2\tilde{\rho}^2\ln\tilde{\rho})\lambda + 3(r_1r_2 - 2\tilde{\rho}^2\ln\tilde{\rho})\tilde{\rho}^3 + 6\tilde{\rho}^5(\ln\tilde{\rho})^2,$$

$$w_2 = r_2^3(2 + r_1\tilde{\rho})w_1,$$

$$w_3 = w_{3a}\lambda + w_{3b}\lambda^2 + w_{3c}\lambda^3 + w_{3d}\lambda^4 + w_{3e},$$

for  $w_{3a} = 90r_2\tilde{\rho}^4(r_2^2(-8 + \tilde{\rho}(5 + (-1 + r_2)\tilde{\rho})) + 4(-1 + r_2)\tilde{\rho}\ln\tilde{\rho}(-2r_2 + \tilde{\rho}\ln\tilde{\rho}))$ ,  
 $w_{3b} = 15r_2^2\tilde{\rho}^3(r_2^2(20 + 3(2 + r_1)r_2\tilde{\rho}) + 4\tilde{\rho}^2\ln\tilde{\rho}(-2r_2 + 3(-1 + r_2)\ln\tilde{\rho}))$ ,  $w_{3c} = -120r_2^4\tilde{\rho}^2(r_1r_2 - 2\tilde{\rho}^2\ln\tilde{\rho})$ ,  
 $w_{3d} = 16r_2^6(1 + 3r_1\tilde{\rho})$  and  $w_{3e} = 45\tilde{\rho}^5(r_2^2(-44 + \tilde{\rho}(-3 + (-5 + r_2)\tilde{\rho})) + 4\ln\tilde{\rho}(4r_1r_2 + 6r_2\tilde{\rho} + (-1 + r_2)\tilde{\rho}^2\ln\tilde{\rho}))$ .

# CLIC DRs design parameters for the case of $N_b = 5.7 \times 10^9$

The design parameters for the alternative design of the CLIC DRs for the case of  $N_b = 5.7 \times 10^9$  are given in the following table.

Table D.1: Parameters for the original and the improved CLIC DRs design, for the case of  $N_b = 5.7 \times 10^9$

Parameters, Symbol [Unit]	Alternative design	
	uniform	trapezium
Energy, $E$ [GeV]	2.86	
Bunch population, $N_b$ [ $10^9$ ]	5.70	
Circumference, $C$ [m]	373.7	
RF Voltage, $V_{RF}$ [MV]	6.50	
Harmonic number, $h$	2493	
Momentum compaction, $\alpha_c$ [ $10^{-4}$ ]	1.3	0.88
Phase advances per arc cell, $(\mu_x, \mu_y)$ [ $360^\circ$ ]	0.510/0.110	
Horizontal and vertical tune, $(Q_x, Q_y)$	(51.16, 14.56)	(51.18, 14.55)
Horizontal and vertical chromaticity, $(\xi_x, \xi_y)$	(-57, -70)	(-67, -75)
	without IBS	
Normalized horiz. emittance, $\gamma\epsilon_x$ [nm-rad]	574.1	350.3
Normalized vert. emittance, $\gamma\epsilon_y$ [nm-rad]	3.3	
Energy spread (rms), $\sigma_\delta$ [%]	0.15	
Bunch length (rms), $\sigma_s$ [mm]	1.6	
Longitudinal emittance, $\epsilon_l$ [keVm]	5.8	
	with IBS	
Normalized horiz. emittance, $\gamma\epsilon_x$ [nm-rad]	682.2	472.8
Normalized vert. emittance, $\gamma\epsilon_y$ [nm-rad]	5.0	4.6
Energy spread (rms), $\sigma_\delta$ [%]	0.15	
Bunch length (rms), $\sigma_s$ [mm]	1.6	
Longitudinal emittance, $\epsilon_l$ [keVm]	5.8	
IBS factors hor./ver./long.	1.18/1.51/1.01	1.35/1.39/1.02

# Luminosity calculation for q-Gaussian density distribution functions

Using Eq. (7.3) as the probability density functions, the general luminosity formula in Eq. (8.1) is solved for q-Gaussian distributions in all planes. For the two beams being identical, integrating firstly over  $s$  and  $s_0$ :

$$I_s^{qG} = \int \int_{-\infty}^{\infty} \rho_{1s}(s - s_0) \rho_{2s}(s + s_0) ds ds_0, \quad (\text{E.1})$$

and then, integrating over  $x$  and  $y$ :

$$I_{xy}^{qG} = \int \int_{-\infty}^{\infty} \rho_{1x}(x) \rho_{1y}(y) \rho_{2x}(x) \rho_{2y}(y) dx dy = \int \int_{-\infty}^{\infty} \rho_x(x)^2 \rho_y(y)^2 dx dy, \quad (\text{E.2})$$

keeping in mind that for  $w = x, y, s$  it is:

$$w \in \left[ \pm \frac{1}{\sqrt{\beta^{qG}(1-q)}} \right], \quad \text{for } -\infty < q_w < 1 \quad (\text{E.3})$$

$$w \in (-\infty, \infty), \quad \text{for } 1 \leq q_w < 3,$$

the solutions of these integrals are found to be:

$$I_s^{qG} = 1, \quad (\text{E.4})$$

and

$$I_{x,y}^{qG} = \begin{cases} \frac{\beta_{x,y}^{qG}}{C_{q_{x,y}}^2} \frac{\sqrt{\pi} \Gamma\left(\frac{-3+q_{x,y}}{-1+q_{x,y}}\right)}{\sqrt{\beta_{x,y}^{qG}(1-q_{x,y})} \Gamma\left(\frac{3q_{x,y}-7}{2(-1+q_{x,y})}\right)}, & \text{for } -\infty < q_{x,y} < 1 \\ \frac{\beta_{x,y}^{qG}}{C_{q_{x,y}}^2} \frac{\sqrt{\pi} \Gamma\left(\frac{-q_{x,y}+5}{2(-1+q_{x,y})}\right)}{\sqrt{\beta_{x,y}^{qG}(-1+q_{x,y})} \Gamma\left(\frac{2}{-1+q_{x,y}}\right)}, & \text{for } 1 \leq q_{x,y} < 3 \end{cases}, \quad (\text{E.5})$$

for  $I_x^{qG} I_y^{qG} = I_{xy}^{qG}$  and, for  $\beta_{x,y}^{qG}$  and  $C_{q_{x,y}}$  being the beta parameters and the normalization factors in the transverse plane. After some simplifications, using also Eq. (7.6) and Eq. (7.8), it is found that the luminosity for q-Gaussian distribution functions depends on the  $\mathcal{I}_{x,y}^{qG}$  (see Eq.(8.4)) which are defined as:

$$\mathcal{I}_{x,y}^{qG} = \begin{cases} \frac{(2+1/k)^2 \Gamma(1+2k) \Gamma(1/2+k)^2}{2\sqrt{3+2k} \Gamma(3/2+2k) \Gamma(k)^2}, & \text{for } -\infty < q_{x,y} < 1 \\ \frac{2}{\sqrt{-(3+2k)}} \frac{\Gamma(-1/2-2k) \Gamma(-k)^2}{\Gamma(-2k) \Gamma(-1/2-k)^2}, & \text{for } 1 \leq q_{x,y} < \frac{5}{3} \end{cases}, \quad (\text{E.6})$$

for  $k = \frac{1}{1 - q_{x,y}}$ . As for the Gaussian case (Eq. (8.2)), the luminosity for q-Gaussian beams colliding head-on does not depend on the longitudinal beam size.

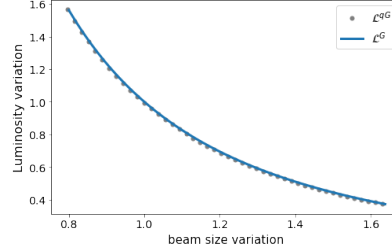


Figure E.1: Luminosity variation with respect to the transverse beam size variation, for the q-Gaussian ( $\mathcal{L}^{qG}$ ) with  $q = 1$  (i.e. normal distribution shape) and the Gaussian case ( $\mathcal{L}^G$ ), for the same beam parameters.

In Fig. E.1, the variation of the luminosity is plotted with respect to the transverse beam size for the  $q$ -Gaussian case ( $\mathcal{L}^{qG}$ ) with  $q = 1$  (i.e. normal distribution shape) and the Gaussian case ( $\mathcal{L}^G$ ). Basically, the transverse beam sizes in Eq. (8.2) and Eq. (8.4) are being varied equivalently and the resulted luminosity changes are found using these two equations. The excellent agreement demonstrates that in the limit of  $q \rightarrow 1$ , the luminosity estimation for  $q$ -Gaussian distributions (given in Eq. (8.4)) allows to obtain the exact same result as for Gaussian distributions. By keeping the  $q$  parameter constant (here  $q = 1$ ) and varying the beam size, the  $\beta^{qG}$  parameter also varies.

# Bibliography

- [1] G. Aad et al. Observation of a new particle in the search for the Standard Model Higgs boson with the ATLAS detector at the LHC. *Phys.Lett.*, B716:1–29, 2012. (Cited on pages 1, 3 and 74.)
- [2] A. M. Sirunyan A. Tumasyan W. Adam E. Aguilo T. Bergauer M. Dragicevic J. Eröo C. Fabjan et al. S. Chatrchyan, V. Khachatryan. Observation of a new boson at a mass of 125 GeV with the CMS experiment at the LHC. *Phys.Lett.*, B716:30–61, 2012. (Cited on pages 1, 3 and 74.)
- [3] G. Apollinari, O. Brüning, T. Nakamoto, and Lucio Rossi. Chapter 1: High Luminosity Large Hadron Collider HL-LHC. *CERN Yellow Report*, (arXiv:1705.08830. 5):1–19. 19 p, May 2017. 21 pages, chapter in High-Luminosity Large Hadron Collider (HL-LHC) : Preliminary Design Report. (Cited on pages 1, 81 and 84.)
- [4] H. Damerau, A. Funken, R. Garoby, S. Gilardoni, B. Goddard, K. Hanke, A. Lombardi, D. Manglunki, M. Meddahi, B. Mikulec, G. Rumolo, E. Shaposhnikova, M. Vretenar, and J. Coupard. LHC Injectors Upgrade, Technical Design Report, Vol. I: Protons. Technical Report CERN-ACC-2014-0337, Dec 2014. (Cited on page 1.)
- [5] Tadeusz Lesiak. The day after LHC: electron-positron colliders are marching on. In Dariusz Bocian and Ryszard S. Romaniuk, editors, *Superconductivity and Particle Accelerators 2018*, volume 11054, pages 17 – 23. International Society for Optics and Photonics, SPIE, 2019. (Cited on page 2.)
- [6] M. Aicheler, P. Burrows, M. Draper, T. Garvey, P. Lebrun, K. Peach, N. Phinney, H. Schmickler, D. Schulte, and N. Toge. A Multi-TeV linear collider based on CLIC technology: CLIC Conceptual Design Report. 2012. (Cited on pages 2, 7, 8 and 9.)
- [7] N. Toge & N. Walker N. Phinney. ILC Reference Design Report Vol. 3. 2007. (Cited on page 2.)
- [8] W. Herr and B. Muratori. Concept of luminosity. 2006. (Cited on pages 2 and 75.)
- [9] D. Angal-Kalinin et al. Chapter 2: Machine Layout and Performance. *CERN Yellow Report*, (arXiv:1705.09447. 5):21–60. 40 p, May 2017. 40 pages, chapter 2 in High-Luminosity Large Hadron Collider (HL-LHC) : Preliminary Design Report. (Cited on page 4.)
- [10] R. Garoby. New RF exercises envisaged in the CERN-PS for the antiprotons production beam of the ACOL machine. Technical Report CERN-PS-85-36-RF, May 1985. (Cited on pages 4, 81 and 84.)
- [11] I. Bejar Alonso and L. Rossi. HiLumi LHC Technical Design Report: Deliverable: D1.10. Technical Report CERN-ACC-2015-0140, Nov 2015. (Cited on pages 4, 81 and 84.)

- [12] M. Lamont and O. Johnson. LHC beam and luminosity lifetimes revisited. Technical Report CERN-ACC-2014-0255, CERN, Geneva, Nov 2014. (Cited on pages 5 and 81.)
- [13] A. Miyamoto, M. Stanitzki, H. Weerts, and L. Linssen. Physics and detectors at clic: Clic conceptual design report. Technical Report arXiv:1202.5940. CERN-2012-003. ANL-HEP-TR-12-01. DESY-12-008. KEK-Report-2011-7, Geneva, Feb 2012. Comments: 257 p, published as CERN Yellow Report CERN-2012-003. (Cited on page 7.)
- [14] M. J. Boland et al. Updated baseline for a staged compact linear collider. Technical Report arXiv:1608.07537., Geneva, 2016. (Cited on page 8.)
- [15] H. Braun et al. Clic 2008 parameters. Oct 2008. (Cited on page 8.)
- [16] Y. Papaphilippou, F. Antoniou, M. Barnes, S. Calatroni, P. Chiggiato, R. Corsini, A. Grudiev, E. Koukovini, T. Lefevre, M. Martini, M. Modena, N. Mounet, A. Perin, Y. Renier, S. Russenschuck, G. Rumolo, D. Schoerling, D. Schulte, H. Schmickler, M. Taborelli, G. Vandoni, F. Zimmermann, P. Zisopoulos, M. Boland, M. Palmer, A. Bragin, E. Levichev, S. Syniatkin, K. Zolotarev, P. Vobly, M. Korostelev, A. Vivoli, C. Belver-Aguilar, A. Faus-Golfe, L. Rinolfi, A. Bernhard, M. Pivi, S. Smith, R. Rassool, and K. Wootton. Conceptual design of the clic damping rings. Technical Report CERN-ATS-2012-176, CERN, Geneva, May 2012. (Cited on pages 8, 49 and 55.)
- [17] L. K. Spentzouris C. Bhat and P. L. Colestock. Measurements of Intrabeam Scattering Rates below Transition in the Fermilab Antiproton Accumulator. *Proceedings of Particle Accelerator Conference*, 1999. (Cited on pages 9, 30 and 34.)
- [18] W. Fischer et al. Measurements of Intra-Beam Scattering Growth Times with Gold Beam below Transition in RHIC. *Proceedings Particle Accelerator Conference*, 2001. (Cited on pages 9, 30 and 34.)
- [19] K. L. F. Bane. Intra-beam scattering, impedance, and instabilities in ultimate storage rings. 2012. (Cited on pages 9, 30 and 31.)
- [20] MAD-X homepage. URL <http://http://mad.web.cern.ch/mad/>. (Cited on pages 10, 33, 49, 55, 56, 58, 84 and 87.)
- [21] F. Antoniou, M. Hostettler, M. Iadarola, S. Papadopoulou, Y. Papaphilippou, D. Pellegrini, and G. Trad. Can we predict luminosity? *Proceedings of the 7th Evian Workshop 2016*, 2016. (Cited on pages 11, 73 and 81.)
- [22] Oliver Sim Brüning. Linear imperfections. 2006. (Cited on pages 12 and 15.)
- [23] S. Y. Lee. *Accelerator Physics (2nd Edition)*. World Scientific, 2004. (Cited on pages 13, 17, 18, 19, 24, 25 and 26.)
- [24] H. Wiedemann. *Particle Accelerator Physics*. SpringerLink: Springer e-Books. Springer London, Limited, 2007. (Cited on pages 13, 14, 16, 17 and 25.)

- [25] B.J. Holzer. Introduction to Transverse Beam Dynamics. (arXiv:1404.0923):27–45. 19 p, Apr 2014. Comments: contribution to the CAS - CERN Accelerator School: Course on Superconductivity for Accelerators, Erice, Italy, 24 Apr - 4 May 2013, edited by R. Bailey, CERN-2014-005. (Cited on page 17.)
- [26] CERN. , Geneva, 2006. CERN. (Cited on pages 17 and 24.)
- [27] A. Chao. *Handbook of Accelerator Physics and Engineering*. World Scientific, 1999. (Cited on pages 18, 24 and 25.)
- [28] A. Wolski. A new lattice design for the nlc positron pre-damping ring. 2002. (Cited on page 18.)
- [29] L. Rivkin. Synchrotron radiation. CERN Accelerator School: Introduction to Accelerator Physics November 5, 2012, Granada, Spain. (Cited on page 22.)
- [30] K. Wille. *The Physics of Particle Accelerators: An Introduction*. Oxford University Press, 1996. (Cited on pages 22 and 23.)
- [31] A. Streun. Lattices for light sources. Technical Report CERN-2006-002, 2006. (Cited on pages 27, 43 and 45.)
- [32] D. Einfeld, J. Schaper, and M. Plesko. A Lattice Design to Reach the Theoretical Minimum Emittance for a Storage Ring. (Cited on page 28.)
- [33] F. Antoniou and Y. Papaphilippou. Analytical considerations for linear and nonlinear optimization of the theoretical minimum emittance cells: Application to the compact linear collider predamping rings. *Phys. Rev. ST Accel. Beams*, 17:064002, Jun 2014. (Cited on pages 28, 38 and 49.)
- [34] A. Robert. High brilliance lattices and the effects of insertion devices. 1990. (Cited on page 28.)
- [35] A. Piwinski. The Touschek effect in strong focusing storage rings. Technical Report physics/9903034. DESY-98-179, DESY, Hamburg, Mar 1999. (Cited on page 30.)
- [36] A. Piwinski. Intra-beam scattering. 1987. (Cited on pages 30 and 32.)
- [37] M. Martini. Intrabeam scattering in the acol-aa machines. Technical Report CERN-PS-84-9-AA, CERN, Geneva, 1984. (Cited on pages 30 and 33.)
- [38] J. D. Bjorken and S. K. Mtingwa. Intrabeam scattering. *Part. Accel.*, 13(FERMILAB-PUB-82-47-THY):115–143. 63 p, Jul 1982. (Cited on pages 30, 33 and 81.)
- [39] K. L. F. Bane, H. Hayano, K. Kubo, T. Naito, T. Okugi, et al. Intrabeam scattering analysis of measurements at KEK’s ATF damping ring. *Phys.Rev.ST Accel.Beams*, 5:084403, 2002. (Cited on page 30.)
- [40] K. Kubo, S.K. Mtingwa, and A. Wolski. Intrabeam scattering formulas for high energy beams. *Phys.Rev.ST Accel.Beams*, 8:081001, 2005. (Cited on page 30.)

- [41] V. Lebedev. Single and multiple intrabeam scattering in hadron colliders. *AIP Conf.Proc.*, 773:440–442, 2005. (Cited on page 30.)
- [42] Tor O. Raubenheimer. The Generation and acceleration of low emittance flat beams for future linear colliders. 1991. (Cited on page 31.)
- [43] K. L. F. Bane. A simplified model of intrabeam scattering. (physics/0206002. SLAC-PUB-9226):4 p, June 2002. (Cited on page 32.)
- [44] F. Zimmermann. Intrabeam scattering with non-ultrarelativistic corrections and vertical dispersion for mad-x. Technical Report CERN-AB-2006-002, CERN, Geneva, Dec 2005. revised version submitted on 2006-03-17 17:13:34. (Cited on page 33.)
- [45] F. Antoniou and F. Zimmermann. Revision of intrabeam scattering with non-ultrarelativistic corrections and vertical dispersion for mad-x. Technical Report CERN-ATS-2012-066, CERN, Geneva, May 2012. (Cited on pages 33, 60, 75, 82 and 93.)
- [46] J. M. Jowett. Introductory statistical mechanics for electron storage rings. *AIP Conf. Proc.*, 153(SLAC-PUB-4033):864–970. 107 p, Jul 1986. (Cited on page 33.)
- [47] A. Vivoli and M. Martini. Intra-beam scattering in the clic damping rings. (CERN-ATS-2010-094. CLIC-Note-834):3 p, June 2010. (Cited on pages 33, 34, 36, 60 and 81.)
- [48] M. Biagini, M. Boscolo, T. Demma, A.W. Chao, K.L.F. Bane, et al. Multiparticle simulation of intrabeam scattering for SuperB. *Conf.Proc.*, C110904:2259–2261, 2011. (Cited on page 33.)
- [49] M. T. F. Pivi. Cmad: A self-consistent parallel code to simulate the electron cloud build-up and instabilities. Technical Report SLAC-PUB-12970, SLAC, Stanford, CA, Nov 2007. (Cited on page 33.)
- [50] K. G. Sonnad, F. Antoniou, Y. Papaphilippou, K. S. B. Li, M. Boscolo, et al. Multi-Particle Simulation Codes Implementation to Include Models of a Novel Single-bunch Feedback System and Intra-beam Scattering. *Conf.Proc.*, C1205201:3147–3149, 2012. (Cited on page 33.)
- [51] P. Zenkevich, A. Bolshakov, and O. Boine-Frankenheim. Kinetic effects in multiple intrabeam scattering. *AIP Conf.Proc.*, 773:425–429, 2005. (Cited on page 33.)
- [52] P. Zenkevich, O. Boine-Frankenheim, and A. Bolshakov. A new algorithm for the kinetic analysis of intra-beam scattering in storage rings. *Nucl.Instrum.Meth.*, A561:284–288, 2006. (Cited on page 33.)
- [53] J. Wei, A. Fedotov, W. Fischer, N. Malitsky, G. Parzen, and J. Qiang. Intra-beam scattering theory and rhic experiments. *AIP Conference Proceedings*, 773(1):389–393, 2005. (Cited on page 34.)
- [54] G. Parzen. Intrabeam scattering growth rates for a bi-gaussian beam, 2004. (Cited on page 34.)

- [55] A.V. Fedotov, A.O. Sidorin, and A.V. Smirnov. Ibs for non-gaussian distributions. In *Proceedings of HB2010, Morschach, Switzerland (MOPD09)*, pages 62–66, 01 2010. (Cited on page 34.)
- [56] A. Xiao and M. Borland. Intrabeam scattering effect calculated for a non-gaussian-distributed linac beam. In *Proceedings of PAC09, Vancouver, BC, Canada*. (Cited on page 34.)
- [57] F. Antoniou. *Optics design of Intrabeam Scattering dominated damping rings*. PhD thesis, 2012. Presented 08 Jan 2013. (Cited on pages 34, 56 and 60.)
- [58] A. Vivoli and M. Martini. Effects of Intrabeam Scattering and Synchrotron Radiation Damping when Reducing Transverse Emittances to Augment the LHC Luminosity. Technical Report sLHC-PROJECT-Report-0032. CERN-sLHC-PROJECT-Report-0032, CERN, Geneva, Feb 2010. (Cited on pages 34 and 81.)
- [59] S. Papadopoulou, F. Antoniou, T. Argyropoulos, M. Fitterer, M. Hostettler, and Y. Papaphilippou. Modelling and measurements of bunch profiles at the LHC. *Journal of Physics: Conference Series*, 874(1):012008, 2017. (Cited on pages 34, 75 and 81.)
- [60] M. Martini, F. Antoniou, and Y. Papaphilippou. Intrabeam Scattering. *ICFA Beam Dyn. Newsl.*, 69:38–59. 22 p, 2016. (Cited on pages 34 and 81.)
- [61] P. Zenkevich. Last advances in analysis of intra-beam scattering in the hadron storage rings. *Nuclear Instruments and Methods in Physics Research A*, 577:110–116, July 2007. (Cited on page 35.)
- [62] L C. Teng. Minimum emittance lattice for synchrotron radiation storage rings, 1985. (Cited on pages 38 and 39.)
- [63] D. Einfeld, J. Schaper, and M. Plesko. A lattice design to reach the theoretical minimum emittance for a storage ring, 01 1996. (Cited on pages 38 and 39.)
- [64] J. Guo and T. Raubenheimer. *Proceedings of EPAC 2002*, 01 2002. (Cited on pages 41 and 44.)
- [65] R. Nagaoka and A. F. Wrulich. Emittance minimisation with longitudinal dipole field variation. *Nuclear Instruments and Methods in Physics Research Section A: Accelerators, Spectrometers, Detectors and Associated Equipment*, 575(3):292 – 304, 2007. (Cited on pages 41 and 44.)
- [66] Y. Papaphilippou and P. Elleaume. Analytical considerations for reducing the effective emittance with variable dipole field strengths. In *Proceedings of the 2005 Particle Accelerator Conference*, pages 2086–2088, May 2005. (Cited on pages 41 and 44.)
- [67] Y. Papaphilippou, A. Ropert, P. Elleaume, and L. Farvacque. Lattice upgrade options for the esrf storage ring. In *Proceedings of the 2005 Particle Accelerator Conference*, pages 2047–2049, May 2005. (Cited on pages 41 and 44.)

- [68] C. Wang, Y. Wang, and Y. Peng. Optimal dipole-field profiles for emittance reduction in storage rings. *Phys. Rev. ST Accel. Beams*, 14:034001, Mar 2011. (Cited on pages 41 and 44.)
- [69] C. Wang. Minimum emittance in storage rings with uniform or nonuniform dipoles. *Phys. Rev. ST Accel. Beams*, 12:061001, Jun 2009. (Cited on pages 41 and 44.)
- [70] S. Papadopoulou. Analytical considerations for reducing the emittance with longitudinally variable bends. presented at the 4th Low Emittance Rings Workshop (LOWERING 2014), 17-19 September 2014, INFN-LNF, Frascati, Italy. (Cited on page 41.)
- [71] A. Streun and A. Wrulich. Compact low emittance light sources based on longitudinal gradient bending magnets. *Nuclear Instruments and Methods in Physics Research Section A: Accelerators, Spectrometers, Detectors and Associated Equipment*, 770:98 – 112, 2015. (Cited on page 41.)
- [72] S. Papadopoulou, F. Antoniou, and Y. Papaphilippou. Alternative Optics Design of the CLIC Damping Rings with Variable Dipole Bends and High-field Wigglers. In *Proceedings, 6th International Particle Accelerator Conference (IPAC 2015): Richmond, Virginia, USA, May 3-8, 2015*, page TUPTY022, 2015. (Cited on page 41.)
- [73] M. A. Domínguez Martínez and F. Toral. (private communication). (Cited on pages 45, 49 and 50.)
- [74] M. A. Domínguez Martínez, F. Toral, H. Ghasem, S. Papadopoulou, and Y. Papaphilippou. Longitudinally Variable Field Dipole Design Using Permanent Magnets for CLIC Damping Rings. *IEEE Transactions on Applied Superconductivity*, PP(99):1–1, 2018. (Cited on pages 45, 47, 49 and 50.)
- [75] H. Braun, E. Levichev, Y. Papaphilippou, S. Siniatkin, and K. Zolotarev. Alternative design of the CLIC Damping Ring Lattice. Technical Report CERN-OPEN-2011-016. CLIC-Note-849, BINP, Novosibirsk, Jun 2010. (Cited on pages 51 and 55.)
- [76] Y. Jiao, Y. Cai, and A. W. Chao. Modified theoretical minimum emittance lattice for an electron storage ring with extreme-low emittance. *Phys. Rev. ST Accel. Beams*, 14:054002, May 2011. (Cited on pages 53 and 54.)
- [77] D. Schoerling and S. Russenschuck. *Superconducting wiggler magnets for beam-emittance damping rings*. PhD thesis, T.U. Bergakademie Freiberg, Freiberg, 2012. Presented 19 Mar 2012. (Cited on page 56.)
- [78] L. García Fajardo, F. Antoniou, A. Bernhard, P. Ferracin, J. Mazet, S. Papadopoulou, Y. Papaphilippou, J. C. Pérez, and D. Schoerling. Design of Nb3Sn Wiggler Magnets for the Compact Linear Collider and Manufacturing of a Five-Coil Prototype. *IEEE Trans. Appl. Supercond.*, 26(4):4100506, 2016. (Cited on page 56.)
- [79] H. Ghasem, J. Alabau-Gonzalvo, F. Antoniou, S. Papadopoulou, and Y. Papaphilippou. Nonlinear optimization of CLIC DRs new design with variable bedns adn hgih field wigglers.

- In *Proceedings, 7th International Particle Accelerator Conference (IPAC 2016): Busan, Korea, May 8-13, 2016*, page WEPMW003, 2016. (Cited on page 57.)
- [80] M. J. Boland et al. Updated baseline for a staged Compact Linear Collider. Technical Report CERN-2016-004, Geneva, Aug 2016. (Cited on pages 58 and 96.)
- [81] S. Burger, A. Ravni, F. Roncarolo, R. Sautier, E. Bravin, A. Boccardi, and A. Goldblatt. Turn by turn profile monitors for the cern sps and lhc. *Proceedings of IBIC 2013*, 2005. (Cited on page 64.)
- [82] M. Sapinski, W. Andreatza, B. Dehning, A. Guerrero, M. Patecki, and R. Versteegen. The first experience with lhc beam gas ionization monitor. Technical Report CERN-ATS-2012-286, CERN, Geneva, Oct. 2012. (Cited on page 64.)
- [83] J. Bosser, J. Camas, L. Evans, G. Ferioli, R. Hopkins, J. Mann, and O. Olsen. Transverse emittance measurement with a rapid wire scanner at the CERN SPS. *Nuclear Instruments and Methods in Physics Research Section A: Accelerators, Spectrometers, Detectors and Associated Equipment*, 235:475–480, 1985. (Cited on pages 64 and 70.)
- [84] F. Méot, L. Ponce, J. Bosser, and R. Jung. Diagnostic with synchrotron radiation of the LHC proton beams. In *Particle accelerator. Proceedings, 8th European Conference, EPAC 2002, Paris, France, June 3-7, 2002*, pages 1945–1947, 2002. (Cited on pages 64 and 69.)
- [85] G. Trad. *Development and Optimisation of the SPS and LHC beam diagnostics based on Synchrotron Radiation monitors*. PhD thesis, LPSC, Grenoble, 2015-05-28. (Cited on pages 64, 69 and 70.)
- [86] G. Papotti, T. Bohl, F. Follin, and U. Wehrle. Longitudinal Beam measurements at the LHC: The LHC Beam Quality Monitor. (CERN-ATS-2011-220):3 p, Nov 2011. (Cited on page 66.)
- [87] T. Bohl and J. F. Malo. The APWL Wideband Wall Current Monitor. Technical Report CERN-BE-2009-006, CERN, Geneva, Feb 2009. (Cited on page 66.)
- [88] A. Jeff, M. Andersen, A. Boccardi, S. Bozyigit, E. Bravin, T. Lefevre, A. Rabiller, F. Roncarolo, C. P. Welsch, and A. S. Fisher. Longitudinal density monitor for the LHC. *Phys. Rev. ST Accel. Beams*, 15:032803, 2012. (Cited on page 66.)
- [89] J. Esteban Muller, E. Shaposhnikova, and L. Rivkin. *Longitudinal intensity effects in the CERN Large Hadron Collider*. PhD thesis, Apr 2016. Presented 28 Jun 2016. (Cited on pages 66 and 67.)
- [90] P. Baudrenghien and T. Mastoridis. Longitudinal emittance blowup in the large hadron collider. *Nuclear Instruments and Methods in Physics Research Section A: Accelerators, Spectrometers, Detectors and Associated Equipment*, 726:181 – 190, 2013. (Cited on pages 66, 75 and 90.)

- [91] H. Timko, P. Baudrenghien, J. Esteban Müller, and E. Shaposhnikova. Operational and beam dynamics aspects of the RF system in 2015. In *Proceedings, 6th Evian Workshop on LHC beam operation: Evian Les Bains, France, December 15-17, 2015*, pages 143–148, Geneva, 2016. CERN, CERN. (Cited on pages 66 and 75.)
- [92] E. M. F. Curado and C. Tsallis. Generalized statistical mechanics: connection with thermodynamics. *Journal of Physics A: Mathematical and General*, 25(4):1019, 1992. (Cited on pages 67 and 75.)
- [93] W. J. Thistleton, J. A. Marsh, K. Nelson, and C. Tsallis. Generalized Box-Müller method for generating -gaussian random deviates. *IEEE Trans. Inf. Theor.*, 53(12):4805–4810, December 2007. (Cited on page 68.)
- [94] Student. The probable error of a mean. *Biometrika*, 6(1):1–25, 1908. (Cited on page 68.)
- [95] O. Brüning, W. Herr, and R. Ostojic. A Beam Separation and Collision Scheme for IP1 and IP5 at the LHC for Optics Version 6.1. Technical Report LHC-Project-Report-315. CERN-LHC-Project-Report-315, CERN, Geneva, Nov 1999. (Cited on page 69.)
- [96] W. Herr. Features and implications of different LHC crossing schemes. Technical Report LHC-Project-Report-628. CERN-LHC-Project-Report-628, CERN, Geneva, Feb 2003. (Cited on page 69.)
- [97] W. Herr. Dynamic behaviour of nominal and PACMAN bunches for different LHC crossing schemes. Technical Report LHC-Project-Report-856. CERN-LHC-Project-Report-856, CERN, Geneva, Jun 2005. (Cited on page 69.)
- [98] M. B. Salvachua Ferrando. Luminosity leveling and beam-beam effects in the lhc. presented at the Beam-Beam effects in Circular Collider workshop, 5-7 February 2018, LBNL, USA. (Cited on page 69.)
- [99] G. Sterbini. MD2201 preprint. Technical report, CERN, Geneva, 2018. (Cited on page 69.)
- [100] N. Karastathis, K. Fuchsberger, M. Hostettler, Y. Papaphilippou, and D. Pellegrini. Crossing Angle Anti-Levelling at the LHC in 2017. In *Proceedings of the 9th International Particle Accelerator Conference: Vancouver, Canada, 2018*. (Cited on page 69.)
- [101] N. Karastathis, K. Fuchsberger, M. Hostettler, Y. Papaphilippou, and D. Pellegrini. Crossing Angle Anti-Levelling at the LHC in 2017. In *Proceedings of the 9th International Particle Accelerator Conference: Vancouver, Canada, 2018*. (Cited on page 71.)
- [102] D. Pellegrini. Incoherent beam-beam effects and lifetime optimisation. In *Proceedings, 8th Evian Workshop on LHC beam operation: Evian Les Bains, France, 2017*, Geneva, 2017. CERN, CERN. (Cited on page 71.)
- [103] S. Fartoukh. Achromatic telescopic squeezing scheme and application to the LHC and its luminosity upgrade. *Phys. Rev. Spec. Top. Accel. Beams*, 16(CERN-ACC-2013-0289):111002. 33 p, Dec 2013. (Cited on page 71.)

- [104] M Hostettler and G Papotti. Luminosity, emittance evolution and OP scans. pages 71–76. 6 p, 2016. (Cited on page 71.)
- [105] O. Karacheban. Understanding of the beam emittance evolution during SB. presented at the LHC Lumi Days 2019, 4-5 June 2019, CERN, Switzerland. (Cited on page 71.)
- [106] J. Bossler, J. Camas, L. R. Evans, G. Ferioli, R. Hopkins, J. Mann, and Ø. Olsen. Transverse emittance measurement with a rapid wire scanner at the CERN SPS. *Nucl. Instrum. Methods Phys. Res., A*, 235(CERN-SPS-84-11-DI-MST):475–480. 14 p, Sep 1984. (Cited on page 71.)
- [107] G. Trad. BSRT calibration. presented at the LHC Machine Committee (LMC), 7 November 2018, CERN, Switzerland. (Cited on page 71.)
- [108] M. Hostettler, K. Fuchsberger, G. Papotti, Y. Papaphilippou, and T. Pieloni. Luminosity scans for beam diagnostics. *Phys. Rev. Accel. Beams*, 21:102801, Oct 2018. (Cited on page 71.)
- [109] S. Papadopoulou. Update on luminosity model including coupling, noise and burn-off for the emittance growth prediction. presented at the 158th HiLumi WP2 Meeting, September 2019, CERN, Geneva, Switzerland. (Cited on pages 73 and 94.)
- [110] M. Fitterer, G. Stancari, A. Valishev, R. Bruce, S. Papadopoulou, G. Papotti, D. Pellegrini, S. Redaelli, G. Trad, D. Valuch, G. Valentino, J. Wagner, and C. Xu. Effect of a resonant excitation on the evolution of the beam emittance and halo population. Technical Report CERN-ACC-NOTE-2017-0037, May 2017. (Cited on page 75.)
- [111] M. Kuhn. Emittance Preservation at the LHC. Master’s thesis, Hamburg U., 2013-03-12. (Cited on page 75.)
- [112] C. Tsallis, F. Baldovin, R. Cerbino, and P. Pierobon. Introduction to nonextensive statistical mechanics and thermodynamics, 2003. (Cited on page 76.)
- [113] I. Eftymiopoulos. LHC lumi days 2019. presented at the LHC Lumi Days 2019 Workshop, June 2019, CERN, Geneva, Switzerland. (Cited on page 76.)
- [114] H. G. Hereward. How good is the R.M.S. as a measure of beam size ? Technical Report CERN-MPS-DL-69-15, CERN, Geneva, 1969. (Cited on page 77.)
- [115] K. Potter. Luminosity Measurements and Calculations. In *Proc. of the CERN Accelerator School, CAS 1992, CERN yellow report*, page 117, 1992. (Cited on page 77.)
- [116] A. L. Crelle, C. W. Borchardt, L. Kronecker, L. Fuchs, K. Hensel, H. Hasse, and F. H. Schottky. *Journal für die reine und angewandte Mathematik*. Number v. 50. W. de Gruyter, 1855. (Cited on page 81.)
- [117] O. H. Nestor and H. N. Olsen. Numerical methods for reducing line and surface probe data. *SIAM Review*, 2(3):200–207, 1960. (Cited on page 82.)

- [118] E. Metral et al. Update of the HL-LHC operational scenarios for proton operation. Technical report, Jan 2018. (Cited on page 84.)



